WELDING SEQUENCE OPTIMIZATION USING LOCAL/GLOBAL FEM ANALYSIS

Eduardo Vitor Meirelles Azevedo Gomes

Dissertação de Mestrado apresentada ao Programa de Pós-Graduação em Engenharia Oceânica, COPPE, da Universidade Federal do Rio de Janeiro, como parte dos requisitos necessários à obtenção do título de Mestre em Engenharia Oceânica.

Orientadores: Jean-David Job Emmanuel Marie Caprace

Marcelo Igor Lourenço de Souza

Rio de Janeiro

Março de 2019

WELDING SEQUENCE OPTIMIZATION USING LOCAL/GLOBAL FEM ANALYSIS

Eduardo Vitor Meirelles Azevedo Gomes

DISSERTAÇÃO SUBMETIDA AO CORPO DOCENTE DO INSTITUTO ALBERTO LUIZ COIMBRA DE PÓS-GRADUAÇÃO E PESQUISA DE ENGENHARIA (COPPE) DA UNIVERSIDADE FEDERAL DO RIO DE JANEIRO COMO PARTE DOS REQUISITOS NECESSÁRIOS PARA A OBTENÇÃO DO GRAU DE MESTRE EM CIÊNCIAS EM ENGENHARIA OCEÂNICA.

Examinada por:

Prof. Jean-David Job Emmaniel Marie Caprace, Ph.D.

Prof. Marcelo Igor Lourenço de Souza, D.Sc.

Profa. Tetyana Gurova, D.Sc.

Dra. Annelise Zeemann do Pinho, D.Sc.

Dr. Lincoln Silva Gomes, D.Sc.

RIO DE JANEIRO, RJ – BRASIL
MARÇO DE 2019

Gomes, Eduardo Vitor Meirelles Azevedo

Welding Sequence Optimization Using Local/Global FEM Analysis/Eduardo Vitor Meirelles Azevedo Gomes. – Rio de Janeiro: UFRJ/ COPPE, 2019.

XIV, 109 p.: il.; 29,7 cm.

Orientadores: Jean-David Job Emmanuel Marie Caprace

Marcelo Igor Lourenço de Souza.

Dissertação (mestrado) – UFRJ/ COPPE/ Programa de Engenharia Oceânica, 2019.

Referências Bibliográficas: p. 90-96.

1. Welding Sequence. 2. Optimization. 3. Welding Simulation. I. Caprace, Jean-David Job Emmanuel Marie *et al*. II. Universidade Federal do Rio de Janeiro, COPPE, Programa de Engenharia Oceânica. III. Título.

Dedico não somente este trabalho, mas todo e qualquer sucesso obtido até o momento, aos meu pais. Os mecenas que incondicionalmente me desejaram, apoiaram e patrocinaram o caminho dos saberes. Devo a eles o intelecto que hoje habita o meu corpo, as experiências vividas e as que ainda viverei. Logo depois do carinho, não acredito que haja bem maior a ser deixado nessa vida do que as oportunidades que me propiciaram. Agradeço ao amor e ao mundo que vocês me deram, serei eternamente grato.

AGRADECIMENTOS

Agradeço a todos que fizeram parte deste ciclo, seja de forma discreta ou contínua. Agradeço às pessoas e instituições que me trouxeram até aqui. Pretendo continuar dando sequência ao que foi construído e deixar ao mundo o meu grão de areia de contribuição.

Não entrarão nomes nestes agradecimentos, pois não seria justo por conta da minha falha memória deixar de fora alguém importante. Todos que me ajudaram sabem que o fizeram. Sabem como o fizeram. E eu também sei. Essa reciprocidade é o que vale para mim.

Serei eternamente grato, muito obrigado a todos.

Resumo da Dissertação apresentada à COPPE/UFRJ como parte dos requisitos necessários para a obtenção do grau de Mestre em Ciências (M.Sc.)

OTIMIZAÇÃO DA SEQUÊNCIA DE SOLDAGEM UTILIZANDO ANÁLISE LOCAL/GLOBAL EM EF

Eduardo Vitor Meirelles Azevedo Gomes

Março/2019

Orientadores: Jean-David Job Emmanuel Marie Caprace

Marcelo Igor Lourenço de Souza

Programa: Engenharia Oceânica

Os processos de solda por fusão são amplamente utilizados na indústria naval, devido principalmente à sua velocidade de produção e à estanqueidade obtida. Contudo, alguns problemas podem ser gerados por conta do alto gradiente de calor imposto pelo processo de soldagem, como distorções e tensões residuais. As distorções podem chegar a proporções que dificultam a futura união de peças, painéis ou blocos. O que torna a produção mais lenta e consequentemente mais custosa. O objetivo deste projeto é a dimunuição das distorções em painéis reforçados por meio otimização da sequência de soldagem. Utilizando um algoritmo genético para otimização e análises de elementos finitos para a avaliação das distorções geradas, mostrou-se que sequências de soldagem específicas podem gerar distorções consideravelmente menores. Além de serem otimizações viáveis em escala industrial quando se considera o tempo gasto na otimização de um painel.

Abstract of Dissertation presented to COPPE/UFRJ as a partial fulfillment of the requirements for the degree of Master of Science (M.Sc.)

WELDING SEQUENCE OPTIMIZATION USING LOCAL/GLOBAL FEM ANALYSIS

Eduardo Vitor Meirelles Azevedo Gomes

March/2019

Advisors: Jean-David Job Emmanuel Marie Caprace

Marcelo Igor Lourenço de Souza

Department: Ocean Engineering

The fusion welding processes are largely employed in the naval industry, mainly due to its productivity and obtained water tightness. However, some problems may be generated due to the high-temperature gradient that is imposed by the welding process, as distortions and residual stresses. Distortions may reach elevated values, making difficult the future assembly of pieces, panels or blocks. Therefore, production becomes slower and consequently elevating costs. The objective of this project is the reduction of distortions on stiffened plates by optimization of the welding sequence. Using a genetic algorithm for the optimization and finite element analysis for the prediction of induced distortions was shown that specific welding sequences might considerably reduce distortions. Additionally, optimizations may be feasible in the industry when considered the time spent on the optimization of a single panel.

CONTENTS

LIST OF FIGURES

LIST OF TABLES

1. INTRODUCTION

Welding is the principal assembly method used in marine structures and fusion processes form the greater part of the welding methods. Ships and offshore platforms may have thousands of meters of welding, thus its effects become an important aim to the naval industry. On a structural view, one of the main issues of welding is residual stresses and distortion, which may drastically influence the structural response of marine structures. Considering that ships and platforms have a lifespan of 20 years or more, these effects may become relevant.

Residual stresses and distortion are consequences of the great temperature gradient observed during a welding process. Therefore, becomes an important subject for the industry as the ultimate strength may be influenced. Chen [1] analyzed the reduction in longitudinal ultimate strength due to residual stresses for steel stiffened plates. Using a model with a simple beam and a plate, Chen found a decrease of 5-7% for different plate thicknesses. Varying the slenderness of an aluminum stiffened plate, composed by a tee-bar, a plate and transversal plates at ends, Farajkhah [2] evaluated the buckling strength reduction. The author found a maximum decrease of 16.5% for these models. Distortions have a more complex role in structural behavior. Depending on the main direction of distortion, the strength may be reduced or increased [3]. Although for the collapse of cracked stiffened plates, the presence of distortions reduces its ultimate strength [4].

Welding sequence has great importance in the final distribution of residual stress and distortion. Some works showed these relations in simple structures [5–7] using Finite Elements Analysis (FEA), presenting a welding sequence that generates lower residual stresses or distortion. Similar studies were carried for more complex structures, as a stiffened grid [8] and a stiffened plate [9] reaching the same consideration. Although some simplifications were made in these models to reduce the computational effort. A small part of authors also uses experiments to study welding sequence [10], as the costs are much higher than simulations. However, the assessment of welding sequence in complete complex structures, as stiffened plates, continues a great boundary of current studies due to computational capacity in FEA.

In order to overcome the computational capacity problem, some methods were developed as the Local/Global approach. This method is based on the FEA solution for small

portions (Local Models) of a complex structure (Global Model), which are joined together to achieve the solution of the Global Model. The main advantage is the time used to run the simulations, which are much lower than a direct simulation of the Global Model. Local/Global approach was introduced by Michaleris [11] for the prediction of welding distortion for a stiffened plate. The local simulation used a two-dimensional cross-section transverse to the welding direction that gives the residual stress distribution. These results were utilized to determine the elastic buckling and large deformations in the three-dimensional global model.

Souloumiac [12] also used the Local/Global approach; however, considered a three-dimensional local model. It was assumed that the plastic strains are located close to the welding bead and only dependent on thermal and mechanical conditions. This enabled the computation of the residual plastic strains in the Local Model and extrapolation to the Global Model. In this work, the Local/Global method was used to optimize the welding sequence, in order to reduce distortions.

The purpose of the present work is to create a model capable to determine the optimal welding sequence of a complex stiffened plate. Considering the objective function as the minimization of average distortion on the base plate. The simulation model is be based on the Local/Global method and a genetic algorithm to run the optimization.

2. STATE OF THE ART

2.1. WELDING SIMULATION

Welding simulations have been used to study different problems, as residual stresses and distortions [13–15], cracks [16,17], keyholes [18–20] and molten pool related problems [21,22]. Although these works may have different approaches, they tend to have a common framework. The most important part of a simulation is the theory behind it. Previously the codes were firstly based on analytical formulations and later on Finite Differences. However, the most popular codes are currently based on Finite Elements. Next will be presented the basic and most important components of a welding simulation.

Models

Simulations start with a model, which will bring the real structure to the numerical language. Therefore, it is essential to build a highly accurate model. The first main component of the model is the form. For a simple structure, some numerical entries may be enough to represent the form, like a bar or even a truss. Although, for more complex structures, it is necessary to use a CAD software.

The second component is the material properties. These are crucial parameters for simulation, because they carry the responses for thermal and mechanical processes. However, it is difficult to obtain all parameters for a specific material, the experimental measurement of these properties become laborious due to the great variation of temperature. The most common solution is to use the properties of a measured material from the family. Typical material properties are density, specific heat, heat conductivity, melting temperature, thermal expansion coefficient, Young modulus, Poisson ratio, yield stress, ultimate tensile strength and elongation.

Initial and Boundary Conditions

With the model in hands, the next step is to set up the Initial and Boundary Conditions. The Initial Condition is the temperature field of the model before the starting of the welding process. Normally, the temperature is homogenous over the model and equal to the room temperature.

Boundary Conditions have mainly focus on global displacement and it is fundamental to grant that the model does not have the freedom to move. These movements are divided into translation and rotation around each axis. Therefore for a three-dimensional model, it is necessary to cover the six degrees of freedom (three of translation and three of rotation).

Again, it is important to highlight that the model will represent the reality, thus the boundary conditions need to represent the real restrictions. If the structure is clamped on some points or areas of its surface, for example, these characteristics will be taken into the simulation.

Some Boundary Conditions are difficult to be taken into a simulation, as a simply supported plate. Fu *et al.* [23] investigated some cases and concluded that the boundary conditions depicted in Figure 1(a) are a good approach for a free supported condition. Later, Caprace *et al.* [24] studied three boundary conditions during a benchmark for T-joint welding, using the one presented by Fu and two additional. These boundary conditions restrict the movements around the six degrees of freedom, but allow the model to expand freely on x and y directions. The higher restraints are on the z axis, which is imposed at least on three points. These examples shows how different may be the representation of reality in a simulation.

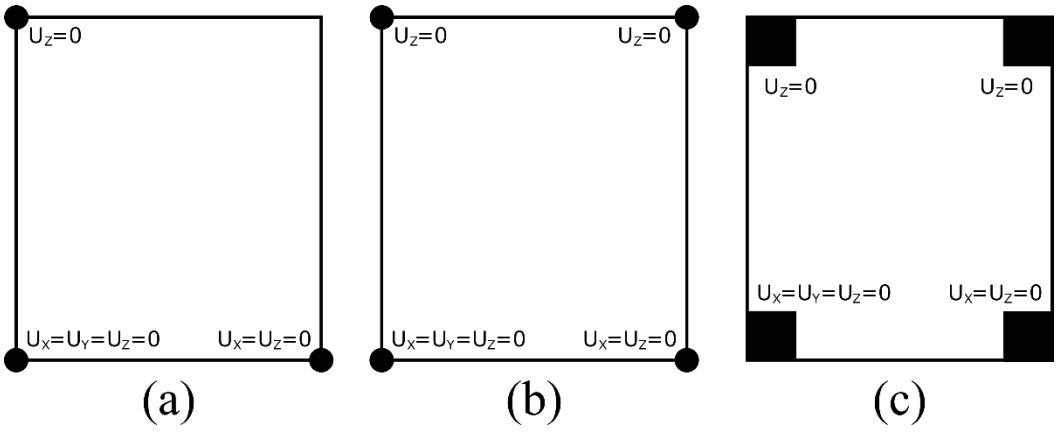

Figure 1 - Boundary conditions for a free supported butt welding plate. The dots on the edges represent the constraints that are imposed on a single point. On the last figure, the squares are areas where the constraints are defined.

The restriction of movement is the focus of boundary conditions; however, there are other important considerations on this phase. Forces or pressure that are imposed on the model, are also considered boundary conditions. Forces may be a resultant force that a part of the structure implies on itself, simplified for the simulation, for example. In the case of

submerged welding, under a certain depth, it is important to consider and set the pressure of surroundings in the simulation.

Especially on welding simulations, more boundary conditions may be considered. Radiation and Convection are important factors of energy loss during welding. Instead of the whole energy be directed into the welding itself, some part is lost due to radiation and convection. Therefore, these boundary conditions may be relevant to a welding simulation.

Welding Configuration

The next important step is to configure the characteristics of the welding process. Firstly are the welding parameters, which are mainly linked to the energy of the welding. Voltage (V) and Amperage (A) indicates the electrical energy amount that will be transformed into thermal energy per time. Generally, this amount of energy is given by the Power of the welding, which is the product between Voltage and Amperage. The last welding parameter is the Travel Speed (TS), indicating the velocity of the welding torch. This parameter also defines the Energy Input Rate (EIR), or the energy per length, that will be delivered into the welding bead. The EIR is given by:

$$EIR = \frac{V \times A}{TS}$$

With the amount of energy that will be delivered to the welding, it is necessary to define how this energy will flow. The device that will do this role is the Heat Source. Currently, this is one of the most important features in welding simulations. The main aspects of welding, as the shape of the weld bead and Heat Affected Zone (HAZ), may considerably vary due to the choice of the heat source. The next section will cover deeply the Heat Sources.

One last welding configuration is the welding sequence. For structures that have more than one welding, the sequence and direction become an important factor in the expected results, as distortion and residual stress. This will also be covered deeply, due to its importance in this study.

Mesh

The last topic of welding simulation is the mesh. Its principal role is to describe the model in a discrete way, dividing it into smaller parts called elements. These parts are used to calculate the response of mechanical and thermal procedures, also the response of each element due to the behavior of the other elements. The size of the elements will interfere in the accuracy of the results. Simplifying, smaller the elements, better the results. Although, it is recommended to make a sensitivity analysis of the mesh. Running simulations with different sizes of elements and evaluating when the results converge. The mesh will also interfere with the computational power that is necessary to run a simulation. Therefore, the choice of mesh size is a balance of required accuracy and computational effort.

2.2. HEAT SOURCE MODELS

Simulation of welding processes is a specific branch of finite element analysis, which requires numerous settings. Some of these configurations are common to a generic analysis, such as boundary conditions and material properties. However, when the scope is welding, the most important setting is the characteristics of the thermal procedure, which is given by a heat source.

Heat sources describe how the heat flows from the welding machine to the base material, which affects the temperature field over the weld bead. This temperature distribution determines the size and shape of the molten pool and the heat-affected zone (HAZ), which are important characteristics of a welding process. Therefore, each welding process, which generates a specific weld bead, has a related ideal heat source that is called Equivalent Heat Source (EHS).

2.2.1. EVOLUTION OF HEAT SOURCES

The evolution of heat sources may be divided into generations, although the complexity progression does not necessarily match with the chronological sequence. This classification tends to enclose heat sources to its capacities and accuracy, which are enhanced generation by generation, as Goldak and Akhlaghi [25] described.

First Generation

The first generation includes basically three simple heat sources proposed by Rosenthal [26] and Rykalin [27]: point, line and sheet heat sources. The point heat source may be useful for shallow weld pools, where a good representation of the temperature field may be achieved. The only necessary parameter is the rate of heat input, considering that all heat sources need to have a defined travel speed.

Line heat sources may be useful for full penetration welds, as laser and electron beam welding. Although the temperature distribution is not quite accurate near the molten pool, this heat source may be used when significant simplifications are acceptable. The parameters used to define it are the length of the line and the rate of heat input per unit of length.

The last heat source of the first generation, known as the sheet heat source, may be used to represent welds made with sheet electrodes on very thick plates. In this case, the parameters that define the heat source are the dimensions, length and width, and the rate of heat input per unit of area.

Second Generation

The second generation achieves better results in accuracy, which was possible due to the adoption of more complex function to heat flux distribution. Pavelic *et al.* [28] achieved advances proposing a heat source with a Gaussian distribution of heat flux, which is known as the disc heat source, due to its projection over the analyzed surface. This distribution of heat flux resulted in a volumetric heat source, which enhanced the results of temperature distribution studies. Although this heat source presents limitations for pointed weld pools, which presents high rates of depth/width on the molten pool.

In 1984, Goldak et al. [29] proposed the most complete heat source model of the second generation, known as double ellipsoidal heat source. Owing to its complex form, which is composed of two hemispheres of different ellipsoids, this heat source may generate better results in the analysis of fusion and heat affected zones. Therefore, this model has been chosen for the present work.

These heat sources increased the accuracy of weld simulations, through its capacities of representing complex shapes of weld pools. It is also possible to represent nonlinear

characteristics as temperature-dependent thermal conductivity, specific heat, radiation and convection boundary conditions.

On the other hand, this generation is limited to temperature distribution analysis outside the weld pool frontier. As long as real physics is not considered inside the molten pool, as the fluid velocity field. This results in fictitious temperatures inside and great accuracy on temperature distribution outside the boundaries of the molten pool.

Third, Fourth and Fifth Generations

The next generations of heat sources aimed to study what occurs inside the molten pool using various theories. Considerations as convection, velocity field and grain growth were used to improve these analyses. These generations will not be discussed in details as long as the aim of the present works remains at the second generation.

2.2.2. DOUBLE ELLIPSOIDAL HEAT SOURCE

Goldak proposed the double ellipsoid heat source in 1984 [29] in order to overcome the differences observed in temperature distribution observed for an ellipsoid heat source. The main contrast was present at the front and trailing edge of the heat source, where the temperature gradient diverged from the experimental experience. Using two different ellipsoids, one for the front and one for the rear, this problem was solved. The heat source scheme is presented in Figure 2.

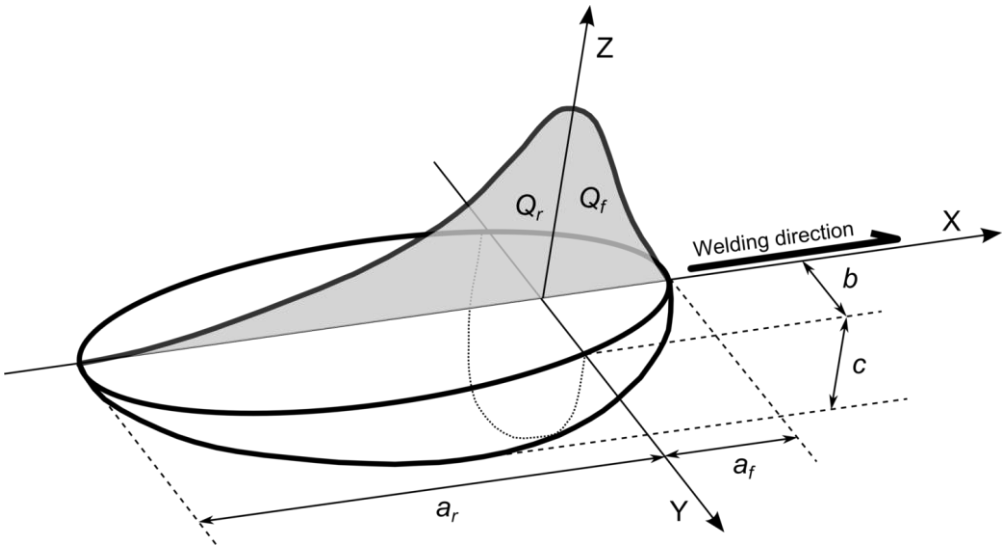

Figure 2 - Goldak double ellipsoidal heat source scheme

The power density distribution for the front quadrant of this model is given by:

$$q(x,y,z,t) = \frac{6\sqrt{3}f_f Q}{abc\pi\sqrt{\pi}} e^{-3y^2/b^2} e^{-3z^2/c^2} e^{-3[x+v(\tau-t)]^2/a_f^2}$$

And for the rear quadrant:

$$q(x,y,z,t) = \frac{6\sqrt{3}f_r Q}{abc\pi\sqrt{\pi}} e^{-3y^2/b^2} e^{-3z^2/c^2} e^{-3[x+v(\tau-t)]^2/a_r^2}$$

Such that:

$$f_f + f_r = 2$$

$$Q = \eta V I$$

For these equations x, y and z represents the spatial coordinates, t the temporal coordinate and v is the travel speed. The fractions of power density are divided in front and rear quadrant given by f_f and f_r respectively. Q is the power delivered to the base material, considering the efficiency (η), voltage (V) and amperage (I) of the welding process. The semi-axes of the double ellipsoid are represented by a_f for the front quadrant, a_r for the rear quadrant, b for the transverse and c for the vertical.

2.3. WELDING SEQUENCE ANALYSES

Welding sequence is a recurrent interest in many segments of the industry as nuclear [8,30,31], naval [6,9,32] and offshore [33]. The main objective is to control the distortion caused by welding, which may be achieved by a specific welding sequence. Distortions have a great impact on these industries influencing the ultimate strength [1,3,34] or the required tolerances [8,30,31].

Studies on welding sequence will have, at the most part of cases, the objective of distortions or residual stresses minimization. For some industries, distortions will complicate the assembling stage, as occurs on shipbuilding. The main current method used on shipyards is the construction by blocks, where stiffened plates are joined into blocks. Then these blocks are welded to form the ship, as presented in Figure 3. Stiffened panels already have a considerable number of welding beads, which may cause distortions that will difficult the assembling to form blocks. These distortions may also trouble the

joining between the blocks. Therefore, distortions may increase the time and resources spent on construction, which will increase the cost.

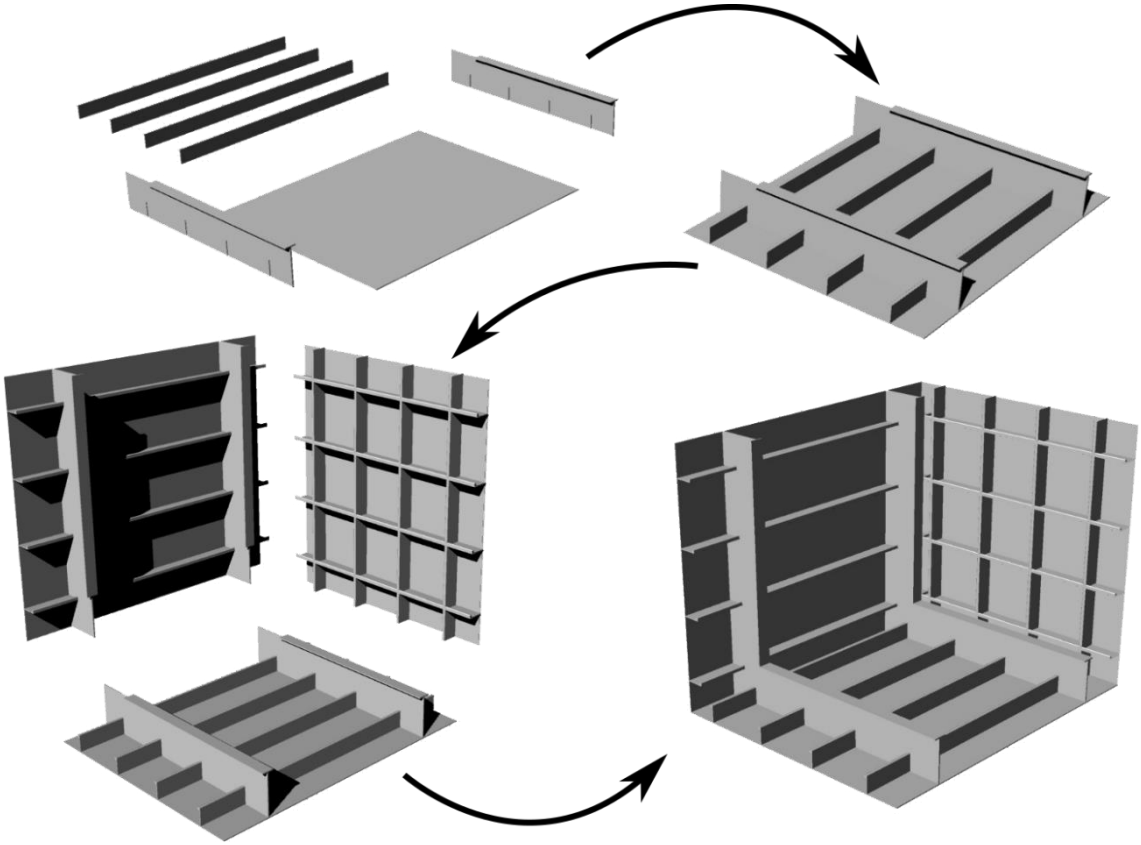

Figure 3 - Scheme of a block assembling. Starts on joining pieces into a stiffened plate. The stiffened plates are joined to form a block

Another important influence of distortions is on nuclear fusion equipment, as vacuum vessels. In this case, the problem does not rely on construction costs, but on the necessity of nearly perfect shaped structures. The pressure gradient that is imposed on this equipment is very severe, which may collapse due to weakened areas. Therefore, the tolerances are much more restricted when compared to the naval industry.

Finite Element Analysis (FEA) plays an important role in these studies due to the low cost, when compared to experiments. Optimization requires a considerable number of variations for a model, which may become financial impracticable depending on how efficient the optimization is desirable to be.

Studies on the influence of welding sequences are made for a wide range of structures. Going from small models, as simple T-joints, to larger models, as a complete stiffened panel. In this section, the studies will be presented according to its structures complexity. Going from the simplest to the most complexes. It is important to highlight that all studies

use FEA, using experiments only to validate the models. Exposing the importance of FEA for welding studies.

2.3.1. SMALL MODELS

Fu *et al.* [6] and Bai *et al.* [35] studied the welding sequence influence on T-joints and I-beams respectively. The first assessed different welding sequences using two or four welding beads to assembly the T-joint model, checking the resultant distortions and residual stresses. On Bai's study, the number of welds is kept constant, changing only the sequence and the direction of weld beads. For the I-beam model was used one weld bead for each side of joining, therefore two beads for lower and two beads for the upper assembly. In this case, it is also analyzed the distortions and residual stresses.

These studies concluded that the welding sequence has a great impact on distortions, as deflection and angular distortion. Distortions may reach differences of 25% in some points when angular distortion was considered. Bai also emphasizes that an optimum welding sequence was determined, based on four sequences previous defined.

Advancing on the analysis of simple structures, Shao *et al.* [36] and Bonnaud [37] introduced a new feature, optimization methods. Shao made a multi-objective optimization for a T-joint. The considered variables were welding parameters (current, voltage and travel speed) and welding sequence and direction. Results endorsed that the welding sequence influences on distortion and residual stresses. Also exposing the opposed relation on distortion and residual stresses, where the decrease on one, leads to an increase of the other.

Bonnaud [37] studied a different case, the impact of welding sequence on multi-pass welding. The models were a plate and a pipe with 10 mm of thickness, which receives 8 weld beads each (4 beads on each side). This work shows that even for multi-pass welds, the sequence is an important factor when distortion is analyzed.

2.3.2. LARGE MODELS

Large structures are treated here as structures that have a more complex design than a T-beam or an I-beam. Works reported in this section have a complex interaction between its weld beads, driving to a complicated interference of distortions. Examples of welding sequence on large structures are given by Xiu *et al.* [30] and Guirao *et al.* [31]. On these

works, authors focused on parts of vacuum vessels, which have tight tolerances for distortions due to welding.

Xiu *et al.* [30] studied a curved stiffened panel composed of two parallel plates and four stiffeners, joined by six weld beads. Distortions were evaluated on the outer and inner shells and for the stiffeners using six welding sequences. Were also used different constraint conditions. The results showed that different distortion distributions are generated for different welding sequence. Although all sequences had a decrease on distortion when the model is under the constraints. Additionally, the zone that is most affected by distortion, changes according to the considered sequence.

The second author focused on a different type of structure, which is a stiffened panel. However, the stiffeners are not only straight but also cylindrical. As pipes that cross the parallel plates. The weld beads are made on the straight stiffeners and on the cylindrical ones. The results show great differences in welding sequences, which may give 68% difference in radial distortion on the middle of the plate. Knowing the importance of the distortion control in this type of structures, this work reinforces the importance of welding sequence.

The naval industry is another segment that stiffened plates are commonly employed. Therefore, some studies are also aimed at straight panels. Chen *et al.* [9] investigated the influence of welding sequence for a panel composed of five transverse and two longitudinal stiffeners. The welding sequence considered only the five transverse ones. Studying six different sequences, the author analyzed the distortion through different longitudinal and transverse lines. Results show that welding sequence made a great impact on distortions, but also depends on the points that are studied. In this case, welding sequences that were the best choice on one line became one of the worsts on another line. Therefore, the right choice of evaluation points is a crucial step.

Li *et al.* [38] studied a similar panel, but composed of 5 longitudinals and 3 transversals. Each longitudinal was joined to the base plate by two welding beads of equal length. The authors also evaluated the use of interface elements, comparing the results with an experimental case. Which concluded that the combination of interface elements and FEA is more accurate to predict distortions than the traditional FEA. Additionally, an optimal welding sequence was defined among the considered cases.

As proposed on the present work, Shadkam *et al.* [32] used inherent strains to evaluate the welding sequence on a stiffened plate. The model was composed of three longitudinal and two transverse girders. Additionally, the authors also considered different types of stiffeners in order to analyze the influence on distortions. The results show the good agreement that inherent strains achieve on thermal elastic plastic simulations. Welding sequence influence was demonstrated for eight different cases, reaching an optimal one. Experiments were carried only on the first part of the work, which is the inherent strains phase.

Welding sequence was the main common subject of these presented works. Although another consideration connects them, which is the limited cases of welding sequences. These restricted cases lead to an optimal result, which may be a local or global optimum. In order to grant that the result is a global optimum, all the possible welding sequences need to be considered. As this may be impossible for some works due to the great number of possibilities, an optimization method is a solution. Although these methods may not achieve the exact optimum point, they lead to a closer one.

2.4. LOCAL/GLOBAL METHOD

Large and complex welded structures may be considered a challenging problem for Finite Element Analysis (FEA). The current computational power is not adequate to solve these types of models directly, due to the coupled thermal-elastic-plastic analysis. Some authors used hardware improvements to make the assessment viable, as Tian *et al.* [39], which ran simulations using a cluster composed of four high-performance personal computers. Another hardware solution was GPU (Graphics Processing Unit) parallel computing [40–42], that may decrease time and memory consumption for simulations of large structures.

Differing from this first group of researches, some authors focused on altering the methods behind the FEA. Instead of trying to accelerate the simulations through powerful machines, they proposed modifications as the Iterative Substructure Method (ISM). Akira *et al.* [43] and Bhatti *et al.* [44] are examples of this type of method, which reduces the nonlinear problem to the surroundings of the weld, simplifying the remaining model as a linear problem. This type of approach may be used on the mesh of the model, using an adaptive method that only refines it on the surroundings of the weld. Huang *et al.* [45] is an example that combined ISM with this adaptive mesh method to achieve high-

performance simulations. Another solution based on meshes was to combine 2D and 3D elements, where some parts of the mesh were made from shell elements and some parts from volume elements [46]. Regarding the complexity, the zone beneath the weld bead was described by volume elements.

The method chosen for this project is called Local/Global Method, used by many authors to study welded stiffened plates [30,32,47–51]. It starts with the subdivision of the Global Model (GM), which represents the structure. Similar weld beads will be represented by a single model, called Local Model (LM). The number of Local Models will depend on how the weld beads may be grouped. If the Global Model has many different types of welds, many Local Models will be necessary. On the other hand, if the Global Model is composed of a single type of weld bead, all of them may be represented by a single Local Model. These Local Models are composed by the weld bead and adjacent structures. In the case of stiffened panels, the adjacent structures are the base plate and stiffeners. An example of the Local Model composition is depicted in Figure 4.

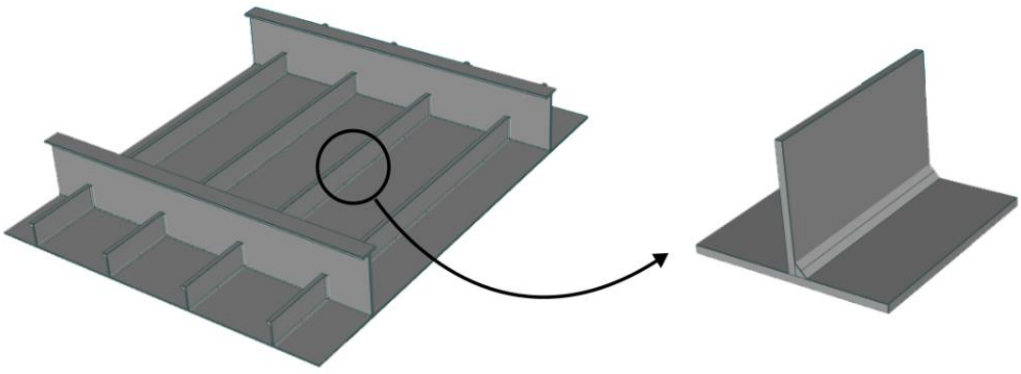

Figure 4 - Example of a Local Model composition

With the Local Models in hands, the next step is to run the simulations and define the mechanical consequences of the welding process. Each Local Model will be simulated using Finite Element Analysis (FEA), which will be a Thermo-Elastic-Plastic (TEP) Analysis. These simulations will give mainly the residual stresses and distortions on the adjacent structures. Based on the Inherent Strain Theory, a database containing the generated strains will be created using the results of the Local Models. The Inherent Strain Theory will be deeply discussed on the next section.

The last part of the method is to use the obtained strains to evaluate the global response of the welded structure. Thus, the welds of the Global Model are substituted by its

respective Local Model strains. A Finite Element Analysis (FEA) will calculate the overall response for each weld, using an Elastic Analysis. The Local/Global Method is schemed in Figure 5.

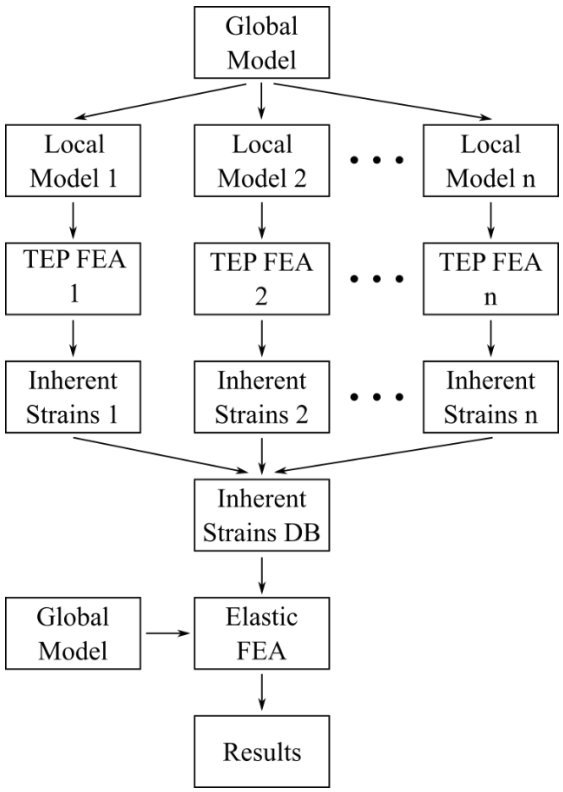

Figure 5 - Local/Global method scheme based on Inherent Strains

The main advantage of the method is that the GM only requires a mechanical analysis, using the results from the LM simulations. Thermo-mechanical analysis, which is heavier to compute, runs only on the LM. Therefore, less computational power is needed to run a large structure. It is important to highlight that this method is interesting for models that have numerous homogenous weld beads. Because the computational effort will be lowered on running a reduced number of thermo-mechanical analysis. If all the welds on the model are different from each other, will be necessary to create a local model for each weld. Losing the advantage of the method.

2.5. INHERENT STRAINS THEORY

The concept of Inherent Strains was introduced by Ueda *et al.* [52] in 1975 as a more general definition of residual stresses sources in a welded structure. Current methods available at the time were based on the relaxation of stresses, measuring respective

deformations caused by sequential cuts. Therefore, these methods were infeasible for complex structures, being this the motivation for a more general method.

2.5.1. CONCEPTUAL MODEL

As an introduction to the Inherent Strains concept, the model presented in Figure 6 may be used. The model is composed by a central bar C and two sidebars S, all fixed on rigid walls, although the rigid wall on the right is free to move along the horizontal axis. This model represents the vicinity of a weld bead, considering the heating of the central bar C.

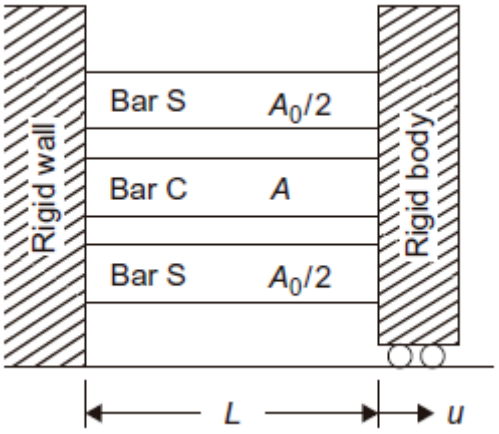

Figure 6 - Conceptual Model of Inherent Strains

Some simplifications are considered in this model and the first is that the material is perfectly plastic. This means that the material will have fixed stress for plastic deformation, being equal to the yield stress (σ_Y). This behavior is presented in Figure 7. Will also be considered that the material properties are not dependent on temperature.

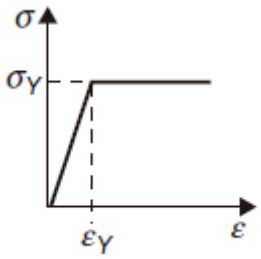

Figure 7 - Stress-Strain Simplification

The inherent strain is influenced by the maximum temperature (T_{max}) reached during the heating process. There are bands of temperature that defines the elastic-plastic behavior, which are based on the yield temperature (T_Y), given by:

$$T_Y = \frac{\sigma_Y}{\alpha E}$$

Where,

$$\alpha \equiv coefficient\ of\ thermal\ expansion$$

$$E \equiv elastic\ modulus$$

This is the temperature where the material reaches the yield stress only with the temperature variation. The bands of elastic-plastic behavior are defined as:

1. Low Temperature $T_{max} \leq T_Y$
2. Medium Temperature $T_Y \leq T_{max} \leq 2T_Y$
3. High Temperature $2T_Y \leq T_{max}$

The model will be analyzed for these three bands and the thermal cycle given by:

$$0°C \rightarrow T_{max} \rightarrow 0°C$$

Conceptual Model for Low-Temperature Cycle

The simpler way to understand the behavior of the model during the thermal cycle is using the Stress/Strain x Temperature graphic. Figure 8 gives the behavior of the model for the Low-Temperature cycle. In this case, the maximum temperature is equal to the yield temperature (T_Y) and when the model reaches this temperature, is also reached the yield stress (σ_Y). However, these values are not exceeded, generating only elastic strain, as may be seen on the right vertical axis. During the cooling stage, the central bar returns to the initial state, with no residual stresses.

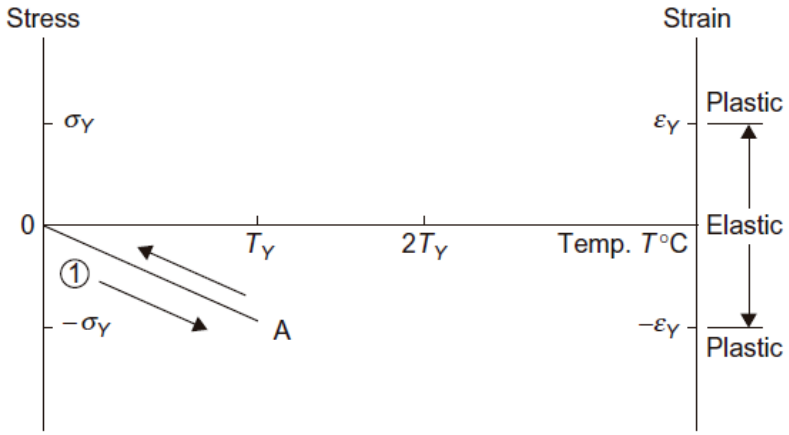

Figure 8 - Stress/Strain behavior during the Low Temperature cycle

Considering the model mathematically, the central bar heating and consequent elongation leads a displacement u of the free rigid wall. Remembering that the displacement corresponds to the volumetric variation of the central bar due to heating. However, it is different from a free bar variation, because the side bars restrain some part of this variation. The total strain may be given by:

$$\varepsilon = \frac{u}{L}$$

For each bar the strain are given by:

Bar S: $\varepsilon = \varepsilon^e$

Bar C: $\varepsilon = \varepsilon^e + \varepsilon^T$

Where:

$$\varepsilon^e \equiv elastic\ strain$$

$$\varepsilon^T \equiv thermal\ strain$$

Hence the strains and stresses are given by:

Bar S	$\varepsilon^e = u/L$	$\sigma = Eu/L$
Bar C	$\varepsilon^e = u/L - \alpha T$	$\sigma = E(u/L - \alpha T)$

In equilibrium, the summation of the forces on the system must be equal to zero. Knowing that $A_0/2$ are the sectional area of each side bar and A the sectional area of the central bar, the equilibrium gives:

$$0 = A_0 \frac{Eu}{L} + AE\left(\frac{u}{L} - \alpha T\right)$$

Rewriting on u:

$$u = \frac{A}{(A + A_0)} \alpha T L$$

Then it is possible to obtain the stresses in function of the temperature, substituting u in the stress relations found:

Bar S: $$\sigma = E \frac{A}{(A + A_0)} \alpha T$$

Bar C: $$\sigma = -E \frac{A_0}{(A + A_0)} \alpha T$$

When the central bar reaches the temperature T_Y, the displacement of the free rigid wall is u_Y, and using the stress relation:

$$\sigma_Y = E\left(\frac{u_Y}{L} - \alpha T_Y\right)$$

Then:

$$T_Y = \left(\frac{\sigma_Y}{E} + \frac{u_Y}{L}\right)/\alpha$$

The relations may be rewritten substituting u_Y and T_Y, thus:

$$T_Y = \frac{A + A_0}{A_0} \frac{\sigma_Y}{E\alpha}$$

$$u_Y = \frac{A}{(A + A_0)} \alpha \left(\frac{A + A_0}{A_0}\right) \frac{\sigma_Y L}{E\alpha} = \frac{A}{A_0} \frac{\sigma_Y L}{E}$$

After the cooling stage, the bars return to the original state. As the yield stress was not exceeded, the deformations occurred in the elastic zone.

Conceptual Model for Medium Temperature Cycle

In this second case, the central bar C will be heated to a maximum temperature T_{max}, such that $T_Y \leq T_{max} \leq 2T_Y$. Using again the Stress/Strain x Temperature graphic, the medium thermal cycle is presented in Figure 9. During the heating stage, the point A is reached, where the temperature is equal to T_Y. The transition from elastic behavior to plastic behavior occurs at this point. As the model was simplified considering the material perfectly plastics, the stress is kept constant and the free rigid wall does not move anymore. All the increase in temperature from this point will generate compression plastic strain over the central bar, reaching the point B. After the cooling stage, the point D is reached, which indicates that the stress is not zero anymore. This point represents the residual stress over the central bar, resultant from the thermal cycle.

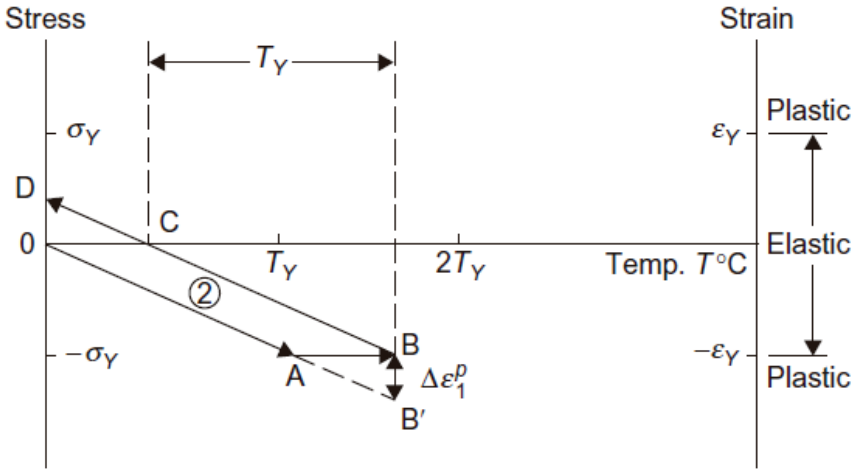

Figure 9 - Stress/Strain behavior during the Medium Temperature cycle

Considering the model, it can be considered that the strain increment after point A is given by $\Delta\varepsilon$. This increment is composed by a plastic and a thermal portion:

$$\Delta\varepsilon = \Delta\varepsilon^P + \Delta\varepsilon^T$$

As there is no more deformation over point A, $\Delta\varepsilon = 0$, thus:

$$0 = \Delta\varepsilon^P + \Delta\varepsilon^T$$

$$\Delta\varepsilon^P = -\Delta\varepsilon^T$$

$$\Delta\varepsilon^P = -\alpha(T_{max} - T_Y)$$

The cooling stage will be divided into two stages, the first goes from T_{max} to $T = T_{max} - T_Y$, which represents a cooling of T_Y. And the second stage goes from T to $0°C$. At the first stage, the variation of temperature generates a shrinkage strain increment $\Delta\varepsilon^T$ that is given by:

$$\Delta\varepsilon^T = -\alpha T_Y$$

Each bar is experiencing the first cooling stage differently. Although strain is equal for these bars because the strain is related to the displacement of the free rigid wall. Considering that $\Delta\varepsilon$ is the strain measured on the free rigid wall and Δu the displacement of the free rigid wall, the relations for each bar may be obtained:

Bar S: $$\Delta\varepsilon = \frac{\Delta u}{L} = \Delta\varepsilon^e$$

Bar C: $$\Delta\varepsilon = \frac{\Delta u}{L} = \Delta\varepsilon^e + \alpha T_Y$$

Where,

$$\Delta\varepsilon^e \equiv elastic\ strain\ increment$$

Thus, the increments of stress may be expressed by:

Bar S: $$\Delta\sigma = E\frac{\Delta u}{L}$$

Bar C: $$\Delta\sigma = E\left(\frac{\Delta u}{L} - \alpha T_Y\right)$$

The increment of displacement may be obtained by the equilibrium of forces, that gives:

$$A_0 E\frac{\Delta u}{L} + AE\left(\frac{\Delta u}{L} - \alpha T_Y\right) = 0$$

Thus,

$$\Delta u = -\frac{A}{A + A_0}\alpha T_Y L = -\frac{A}{A_0}\frac{\sigma_Y L}{E}$$

At this point, given by C on Figure 9 the increment of displacement is equal to the total displacement generated by the heating stage. Therefore, the model becomes to the initial position without displacement, stress and strain.

On the second cooling stage, the temperatures will be decreased to $0°C$ and reach the point D on Figure 9. The total strain on bar C is composed by elastic and thermal strains, that are related to the strain of the free rigid wall and given by:

$$\Delta\varepsilon = \frac{\Delta u}{L} = \Delta\varepsilon^{e} - (T_{max} - T_Y)$$

In addition, stress may be:

$$\Delta\sigma = E\left\{\frac{\Delta u}{L} + \alpha(T_{max} - T_Y)\right\}$$

The increment of displacement may be calculated by the equilibrium of forces:

$$A_0\frac{\Delta u}{L} + A\left\{\frac{\Delta u}{L} + \alpha(T_{max} - T_Y)\right\} = 0$$

Solving the equation for Δu:

$$\Delta u = -\frac{A}{A + A_0}\,\alpha L(T_{max} - T_Y)$$

The final stresses on the bars may be given by:

Bar S: $$\sigma = -E\frac{A}{A + A_0}\alpha(T_{max} - T_Y)$$

Bar C: $$\sigma = E\left\{-\frac{A}{A - A_0}\alpha(T_{max} - T_Y) + \alpha(T_{max} - T_Y)\right\}$$

Simplifying:

Bar S: $$\sigma = -E\frac{A}{A + A_0}\alpha(T_{max} - T_Y)$$

Bar C: $$\sigma = E\frac{A_0}{A - A_0}\alpha(T_{max} - T_Y)$$

Might be logic that this second cooling stage is responsible by the residual stresses. Although, these stresses are generated at the heating stage when the yield temperature is surpassed due to plastic strains. The source of residual stresses is the plastic strain, that receives the name of Inherent Strain (ε^*). Numerically the Inherent Strain is given by:

$$\varepsilon^* = \Delta\varepsilon_1^p = -\alpha(T_{max} - T_Y)$$

Integrating the Inherent Strain is found the Inherent Displacement (ΔL^*):

$$\Delta L^* = \varepsilon^* L = -\alpha(T_{max} - T_Y)L$$

Conceptual Model for High-Temperature Cycle

In this cycle, the maximum temperature (T_{max}) reached is equal or higher than $2T_Y$, that results in different residual stresses. As presented for the previous cycles, is used the Stress/Strain x Temperature graphic depicted in Figure 10. On the heating stage, the model reaches the point A, which represents the boundary between elastic and plastic behavior. The model is kept under heating and goes to point P, due to the perfectly plastic material consideration, that keep constant the stress on plastic strain. After the heating stage, the model is cooled reaching the point R, which is another boundary of stress due to the perfectly plastic material consideration. At this point, the model continues to loose heat and goes to point G. Therefore the model does not go to the initial state, were generated residual stresses on the workpiece. It is important to note that in high temperature cycle, the model suffers two plastic strains, one of compression on heating and another of tension on cooling.

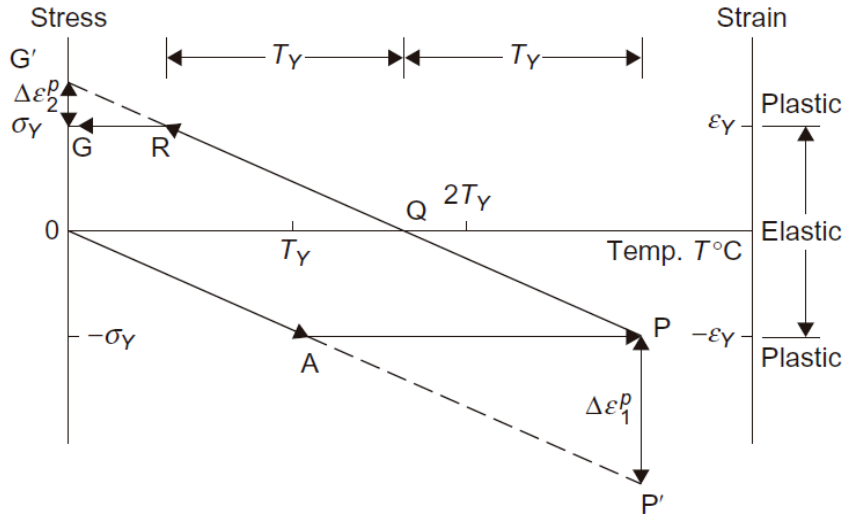

Figure 10 - Stress/Strain behavior during the High-Temperature cycle

Mathematically, it is important to analyze the second heating stage, where the model goes from point A to point P. At this phase there is no strain on the free rigid wall, which may be described as:

$$\Delta\varepsilon = \Delta\varepsilon^P + \Delta\varepsilon^T = 0$$

Rewriting:

$$\Delta\varepsilon^P = -\Delta\varepsilon^T = -\alpha(T_{max} - T_Y)$$

This formulation exposes that all thermal strain ($\Delta\varepsilon^T$) is generating compressive plastic strain ($\Delta\varepsilon^P$) on the model. In addition, the plastic strain is numerically equal to the extrapolation to the point P', which gives $\Delta\varepsilon^P = \Delta\varepsilon_1^p$. The cooling stage will be separated into three stages. The first cooling the model by T_Y, which goes from point P to point Q. A second stage being cooled also by T_Y, reaching the point R, and the last stage cooling the model to $0°C$, reaching the final state at point G.

The first cooling stage leads the model to a free stress state that is represented by point Q. As done in the first stage, the model is cooled again by T_Y, going from point Q to point R. At this cooling stage, the central bar enters again the stress zone, however under a tension stress. Point R represents the boundary between elastic and plastic tension strain, this indicates that the next cooling stage will generate plastic strain on the central bar. As occurred in the heating stage, all the thermal stress turns into plastic strain, which may be represented by:

$$\Delta\varepsilon^P = -\Delta\varepsilon^T = \alpha(T_{max} - 2T_Y) = \Delta\varepsilon_2^p$$

The residual stresses on each bar are given by:

Bar C: $\sigma = \sigma_Y$

Bar S: $\sigma = -\left(\frac{A}{A_0}\right)\sigma_Y$

As mentioned before, plastic strains are generated in the heating and cooling stages. On the first stage, compressive plastic strains are generated and tensile plastic strains on the second stage. The residual plastic strain is given by the sum of these two strains applied on the central bar, which gives:

$$\Delta\varepsilon^P = -\alpha(T_{max} - T_Y) + \alpha(T_{max} - 2T_Y) = -\alpha T_Y$$

Remembering that the generated plastic strain corresponds to the Inherent Strains (ε^*), it may be resumed by:

$$\varepsilon^* = \Delta\varepsilon_1^p + \Delta\varepsilon_2^p = -\alpha T_Y$$

The corresponding Inherent Deformation:

$$\Delta L^* = \varepsilon^* L = -\alpha T_Y L$$

It should be noted that as done in earlier thermal cycles, T_Y may be expressed as:

$$T_Y = \frac{A}{A + A_0}\frac{\sigma_Y}{E\alpha}$$

2.5.2. USING INHERENT STRAIN IN LOCAL/GLOBAL MODELS

Inherent Strain concept was first developed aiming a more general model to analyze the residual stresses generated by fusion welding processes. Later it was adopted by Local/Global methods in Finite Elements Analysis (FEA), which uses Inherent Strains as a tool to transfer information from a Local Model to a Global Model.

Considering that the local models results are in hands, these data may be transferred to the global model. At this point, the Inherent Strains are applied to the global model and some steps are necessary to determine the residual stresses or distortions distribution. It starts with the calculation of the equivalent nodal forces for each element $\{f\}^e$, which is found using the work done on each element. The external work done by nodal forces is given by:

$$\{\delta a\}^{e^T}\{q\}^e$$

Where

$$\{\delta a\}^e \equiv virtual\ displacement\ of\ nodes$$

$$\{q\}^e \equiv individual\ forces\ on\ nodes$$

It is also possible to calculate the internal work due to stress and body forces:

$$\{\delta\varepsilon\}^T\{\sigma\} - \{\delta u\}^T\{b\}$$

Where,

$$\{\delta\varepsilon\} \equiv virtual\ strain\ within\ the\ element$$

$$\{\sigma\} \equiv stress\ on\ the\ element$$

$$\{\delta u\} \equiv virtual\ displacement\ within\ the\ element$$

$$\{b\} \equiv distributed\ body\ forces$$

Considering that $\{u\} = [N]\{a\}$, $\{\varepsilon\} = [B]\{a\}$ and that $([A][B])^T = [B]^T[A]^T$, the work done by internal forces may be rewritten as:

$$\{\delta a\}^{eT}([B]^T\{\sigma\} - [N]^T[b])$$

Where,

$$[B] \equiv strain - displacement\ matrix$$

$$[N] \equiv shape\ functions\ matrix$$

The external work must be equal to the internal work integrated over the element volume, thus:

$$\{\delta a\}^{eT}\{q\}^e = \{\delta a\}^{eT}\left(\int_{V^e}[B]^T\{\sigma\}\,dV^e - \int_{V^e}[N]^T\{b\}\,dV^e\right)$$

Hence:

$$\{q\}^e = \int_{V^e}[B]^T\{\sigma\}\,dV^e - \int_{V^e}[N]^T\{b\}\,dV^e$$

Knowing that:

$$\{q\}^e = [K]^e\{a\}^e + \{f\}^e$$

Where,

$$[K]^e \equiv stiffness\ matrix\ for\ the\ element$$

$$\{f\}^e \equiv equivalent\ nodal\ force$$

As $[K]^e$ is given by:

$$[K]^e = \int_{V^e}[B]^T[D][B]\,dV^e$$

The equivalent nodal force may be given by:

$$\{f\}^e = -\int_{V^e} [N]^T\{b\}dV^e - \int_{V^e} [B]^T[D]\{\varepsilon_0\}\,dV^e + \int_{V^e} [B]^T\{\sigma_0\}\,dV^e$$

Where

$$\{\varepsilon_0\} \equiv initial\ strain$$

$$\{\sigma_0\} \equiv initial\ stress$$

In the specific case of Inherent Strain, the body forces and initial stress are not considered. Therefore, considering $\{\varepsilon_0\} = \{\varepsilon^*\}$, the nodal force is given by:

$$\{f\}^e = -\int_{V^e} [B]^T[D]\{\varepsilon^*\}\,dV^e = -[L]^e\{\varepsilon^*\}^e$$

These equivalent nodal forces are summed all over the model, giving an equivalent force $\{f\}$:

$$\{f\} = \sum \{f\}^e = \sum -[L]^e\{\varepsilon^*\}^e = -[L]\{\varepsilon^*\}$$

Using the stiffness matrix, these forces are converted into nodal displacements:

$$\{u\} = -[K]^{-1}\{f\} = -[C]\{f\} = [C][L]\{\varepsilon^*\}$$

Considering again each element, the strain is composed of an elastic and a plastic component, relating to the displacements on elements by:

$$\{\varepsilon\}^e + \{\varepsilon^*\}^e = [B]^e\{u\}^e = [B]^e[T]^e\{u\}$$

Where,

$$[T]^e \equiv displacement\ transformation\ matrix$$

This matrix transforms the displacements into displacements for a single element. Substituting the previously found relation of displacements:

$$\{\varepsilon\}^e + \{\varepsilon^*\}^e = [B]^e[T]^e[C][L]\{\varepsilon^*\}$$

Considering a matrix that converts the total inherent strain into inherent strain for each element, it is given:

$$\{\varepsilon^*\}^e = [U]^e\{\varepsilon^*\}$$

Where,

$$[U]^e \equiv inherent\ strain\ transformation\ matrix$$

Thus, the elastic strain on each element may be given by:

$$\{\varepsilon\}^e = [B]^e[T]^e[C][L]\{\varepsilon^*\} - [U]^e\{\varepsilon^*\}$$

That may be condensed in:

$$\{\varepsilon\}^e = [H^*]^e\{\varepsilon^*\}$$

To achieve the elastic strains and residual stresses on the model, it is necessary to summarize the elastic strains ($\{\varepsilon\}_i^e$) and residual stresses ($\{\sigma\}_i^e$) on each element i. Considering that the elements are A, B, …, respectively, the elastic strain and residual seresses on the model are given by:

$$\{\varepsilon\} = \lfloor \lfloor\varepsilon\rfloor_A^e, \lfloor\varepsilon\rfloor_B^e, \dots \rfloor^T = [H^{*\prime}]\{\varepsilon^*\}$$

$$\{\sigma\} = \lfloor \lfloor\sigma\rfloor_A^e, \lfloor\sigma\rfloor_B^e, \dots \rfloor^T = [M']\{\varepsilon^*\}$$

2.6. OPTIMIZATION METHOD

One of the crucial phases of this project is the optimization of the welding sequence. Due to the time consumed in each simulation, it is important to achieve an optimal result with the lower number of iterations as possible. This goal success relies on the right choice of the optimization method. Virfac, the software used for the welding simulations, presents an enhanced optimization code based on a genetic algorithm, which is a known method in welding optimization [53,54].

The main advantages of genetic algorithms, when compared to conventional algorithms, are the effectiveness in reaching the global optimum, the governing function does not need to be continuous and the transition rule is probabilistic. These characteristics appropriately match with welding optimization needs [55].

2.6.1. GENETIC ALGORITHMS

Inspired by the biological process of natural selection, Genetic Algorithms (GA) mimics the advantages of sexual reproduction under environmental pressure. As described by Kramer [56], a basic genetic algorithm may be represented by the flow chart depicted in

Figure 11. It starts by setting an initial population, where each individual is represented by a vector or a string of bits. The entries of the vector or bit string determine the genotype of each individual and represent the characteristics under study. It is also necessary to define the domain of each entry, which always might be respected when a genotype is defined.

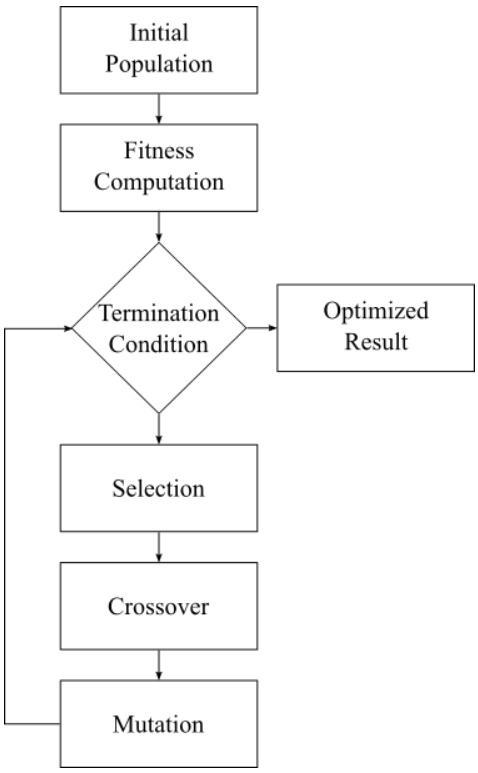

Figure 11 - Flow chart of a generic genetic algorithm

The next step is the evaluation of the individual genotype, given in the flow chart by the Fitness Computation. This evaluation is made based on the phenotype, which is the resultant characteristic exerted by the genotype. For a single objective optimization, only one phenotype is considered. However, more phenotypes may be evaluated in the case of multi-objective optimizations. The concept of phenotypes may be illustrated considering the optimization of welding parameters: voltage, amperage, travel speed, etc. Phenotypes are the weld bead characteristics generated by a combination of welding parameters, which may be the depth and width of the bead, the quality, etc.

On all types of optimizations, it is necessary to define a termination condition, which tells when the algorithm loop stops. This condition will depend on how much time is available for the complete optimization, considering the computational effort and the time spent on each iteration. A common termination for heavy optimizations is the number of iterations.

In this case, the user is able to estimate the time that will be spent to run the complete algorithm. For lighter studies, may be used the stagnation parameter. When the difference between the results obtained during iterations becomes too small.

Selection is the stage where individuals from a generation are selected to be the parents of the next generation. On nature, the selected individuals are those who are better adapted to the environment. On optimization, the selection is made based on the phenotypes that are better suited to the optimization objective. In the case of minimization, the phenotype should be the lower of its generation. For maximization, the individual should be the one with the higher results of its generation.

Genetically, the main feature of sexual reproduction is the crossover. This phenomenon is characterized by the combination of the genetic material of parents. It is also the most important step in a genetic algorithm, being the main responsible of domain coverage. The crossover may be depicted by Figure 12, where the offspring receives a part of the first parent genotype and a part of the second parent genotype. In this case, the portions of genotype passed from each parent are equal, however this may adjusted. A possibility is assume a random percentage, where the unique constraint should the sum of portions from each parent, which needs to be equal 100%.

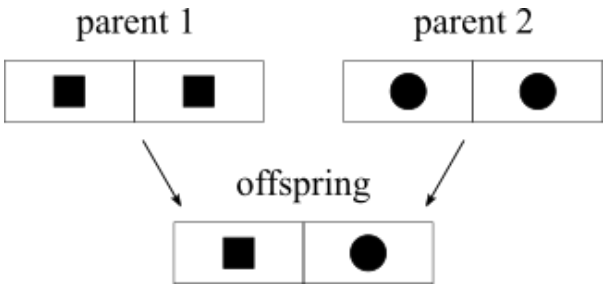

Figure 12 - Crossover scheme

The last step in the genetic algorithm presented in Figure 11 is the mutation. This is a natural process of genotype construction, which is independent of sexual reproduction. It is adopted in the genetic algorithm as another method of domain coverage, as crossover may stick the optimization into a local optimum. There are three main requirements for mutation. The first is reachability, i.e., each point of solution space must be reachable by mutation. The second requirement is unbiasedness, which is the prevention of bias in a particular direction of the domain. The last one is scalability. This concept may be translated as the rate of mutation that should occur in the algorithm. A common adoption

is a Gaussian distribution for mutation probability, as many natural processes are modeled by this distribution.

The concepts addressed here are the base of genetic algorithms. However, some modifications are made in order to enhance the efficiency of these algorithms. A promising approach is the use of neural networks inside a genetic algorithm [57,58]. This is a concept adopted by Virfac optimization module and will be better discussed in the next section.

2.6.2. XTREME TECHNOLOGY

Xtreme is a technology developed by Optimal Computing [59] and present in Virfac optimization module. It is an advanced genetic algorithm enhanced by a neural network, which performs as a simplified simulation model. The Xtreme algorithm, depicted in Figure 13, sends back the results obtained from each simulation to the neural network. This procedure provides data to train the neural network as an approximate simulation. Hence, an inner optimization is made by the genetic algorithm and the neural network, providing models to the main simulation that are closer to the optimal point. This inner optimization allows a faster convergence, working as a filter to points that could distance the current model from the optimal point.

The neural network performance is clearly linked to the size of the database that is created to train it. Therefore, as the optimization advances in iterations, better should be the predictions made by the neural network. Filtering more effectively models that could drive the optimization to undesired directions.

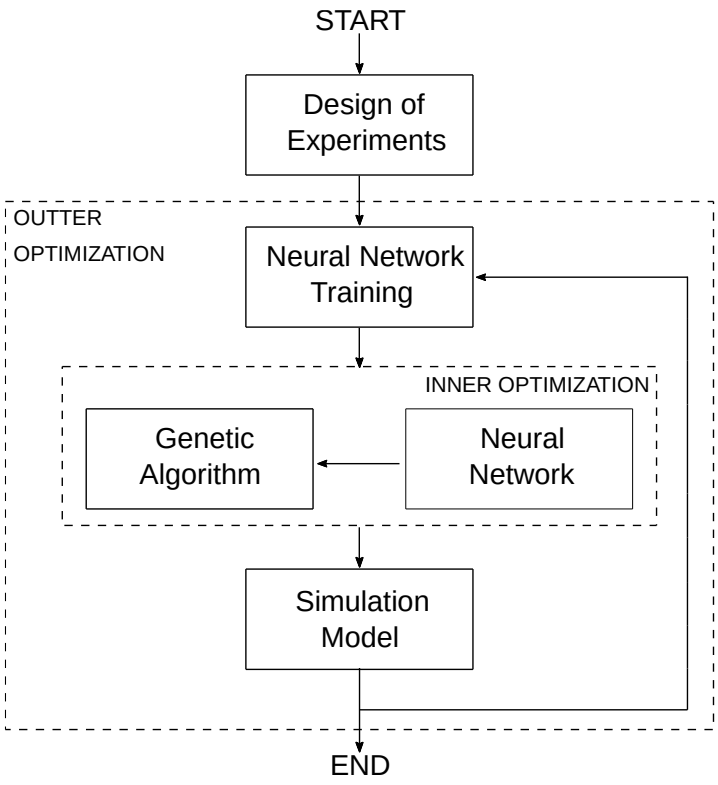

Figure 13 - Xtreme Technology algorithm scheme

The algorithm may be more clearly explained considering a model with one design variable and one minimization objective. Figure 14 depicts the algorithm after three iterations, where the triangles represent the results obtained by the main simulation of three different models. The neural network is trained using these models and it builds a simplified simulation, represented by the curve. It allows finding an optimum model by the genetic algorithm, depicted by the circle in Figure 14.

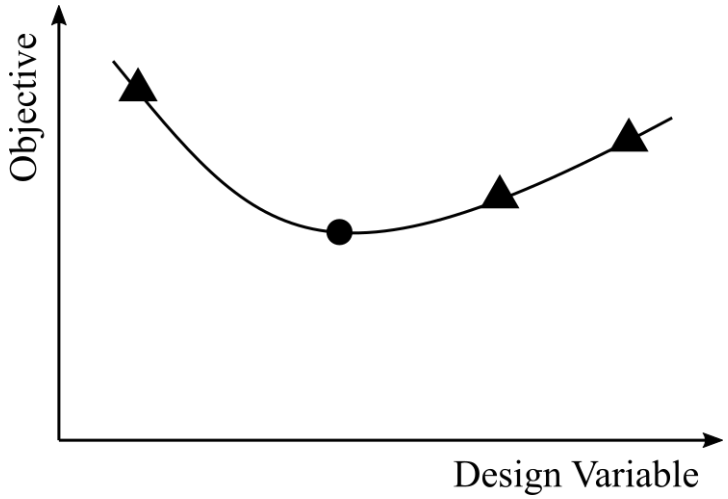

Figure 14 - Explanation of Xtreme algorithm in a first stage

The current model is analyzed by the main simulation, resulting in a new point on the data available for the neural network. This stage is presented in Figure 15. The neural network is trained and it results in a more accurate simplified simulation, represented by the new curve. Therefore, a new inner optimization is made, given by the circle on the minimum of the curve.

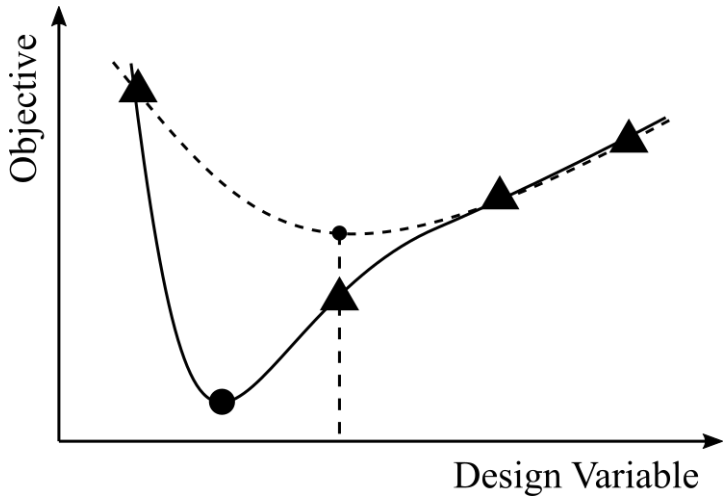

Figure 15 - Explanation of Xtreme algorithm in a second stage

The expectation is a more efficient optimization, converging in fewer iterations when compared to a standard genetic algorithm. The company promises drastically acceleration, achieving up to 100 times faster the optimal solution. However, the efficiency will strongly depend on the performance of the neural network, which would be affected by the nature of the evaluated model.

3. METHODOLOGY

The method developed for this project is quite similar to the local/global method. However, instead of ending it with the global model, optimization is applied. A detailed scheme of the method is presented in Figure 16. It starts with the stiffened plate, considering how the weld beads should be grouped to determine an ideal set of local models. These groups should comprehend similar beads, although it is normal to exist variations among the considered similar beads. In practice, the beads may vary due to fluctuations in welding equipment or welder skills.

With the groups determined, the local models are developed in a CAD tool or software. A common procedure is to develop a CAD model for the global model and cut the local models from it. Easier than creating every single model, this procedure also grants the geometry equivalence. It is important to take some precautions in this phase. As the aim of this method is to map the distortions field and use it into a global model, the models should grant that a level of similarity is achieved. An important factor is the size of the model. It needs to give space for the thermal field development during the welding. Therefore, the plates that are being welded need to have a considerable length and width. Although there is no recommendation or rule of thumb, it is an important feature that should be considered.

Finite elements analysis has some crucial settings as constraints, which will prevent the translation and rotation of the model. In the case of local models, constraints have a more important role, because a part of the global model is being simulated separately. Thus, the boundaries of the local model need to have similar behavior as it is being simulated inside the global model. The recommendation of Virfac manuals is to restraint the translation of the generated faces, preventing them to move in any direction. This approach is not the ideal one, as expansion or retraction of the adjacent material is expected. However, it is a better approximation than a free condition, as the rest of the global model exerts resistance for these movements.

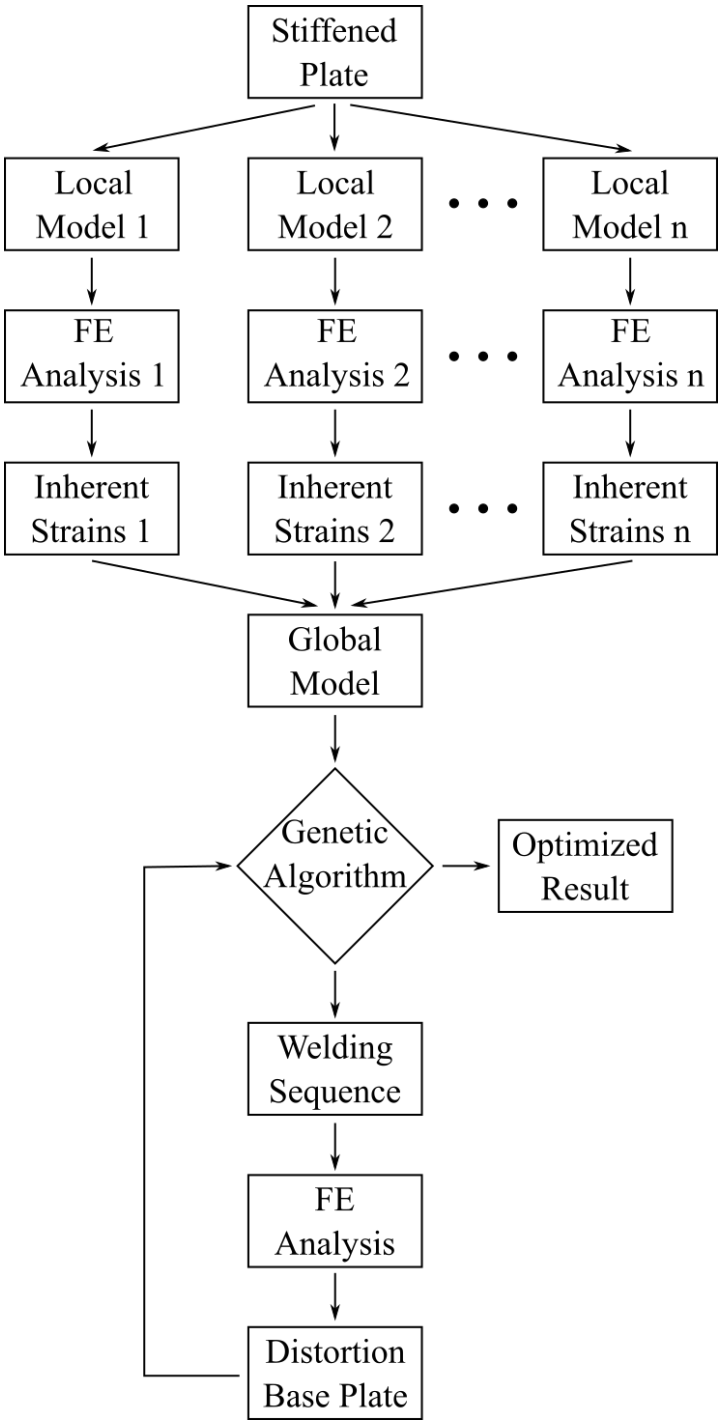

Figure 16 - Method flowchart

Another essential setting in welding simulations is the choice and adjustment of the heat source. It will define how the heat flows from the welding equipment to the weld bead and base material. Therefore, this is one critical step of the method. The choice of the heat source is an easier task, as the Goldak [29] heat source is currently the best option when the analysis is restricted to the outside part of the welding pool.

For the adjustment of this heat source, a considerable effort is necessary as it is made by trial and error method. Simulations are ran using guesses for the first set of parameters and variations are made according to the results. The main feature used for the adjustment is the generated molten pool, which must match with the weld bead shape. Width (w_f) and depth (d_f) are the typical parameters used to describe the shape of the molten pool, as presented in Figure 17. A second feature may be used for the adjustment, as the Heat Affected Zone (HAZ) shape.

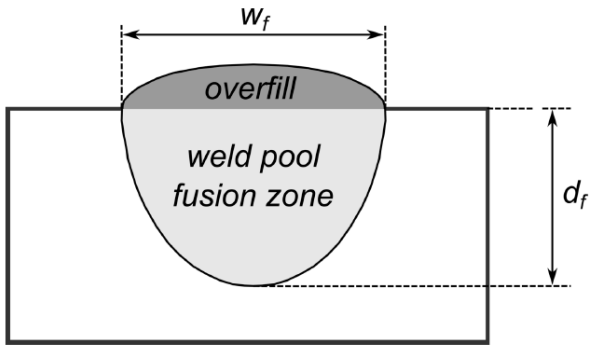

Figure 17 - Molten pool shape, described by width and depth

The results of each local model are then transferred into a database through the inherent strains method, as explained in section 2.5.2. This data is commonly called the inherent strains of the local model. Using the stiffened plate CAD, it is possible to build a global model based on the local models. As made for the local models simulations, important characteristics of the global model are defined in this phase.

Again, the constraints are one of the most important features that need to be set. However, in the global model, the restrictions will depend on how the simulation intends to represent the real experiment. Some constraints, as simply supported case, are complicated to represent due to the limitations of finite elements. In the real experiment, translation and rotation are avoided by a combination of gravity and friction. Although some level of movement is allowed. This need for translation and rotation restriction will lead sometimes to approaches that are far different from the real experience. However, will be a tool to represent as close as possible the reality.

In the Local/Global method, another important feature is the welding sequence, which will be driven by the optimization algorithm in this project. The sequence is modified in order to reduce the distortions, which are assessed by a mechanical simulation based on local/global method. This part of the method is described by a loop, which has the number

of iterations as the stoppage criterion. The choice of the iterations as the criterion is due to the elevated time consumption of these simulations. If another criterion was chosen, as a relative decrease on distortion, it would be possible that the optimization runs for long terms, like weeks. Thus, it is essential for the project the right choice of the stoppage criterion.

It is expected that this method will give an optimized welding sequence, which reduces considerably the distortion over the base plate. Also supported by other works on this field. The next section will show the application of this method for a real large stiffened plate and next to the results obtained from it.

4. CASE STUDY

4.1. AIM OF STUDY

The object of analysis in this project is a stiffened plate that was assembled and studied by DAMEN in order to validate Virfac welding module. We received its specifications and used it as the base of our study. Shown in Figure 18, the stiffener plate is composed by a base plate, two girders and four stiffeners. This is a common composition for straight stiffened plates in shipyards, maybe varying in number of stiffeners and girders. However, these variations are not a problem for an application of the proposed method.

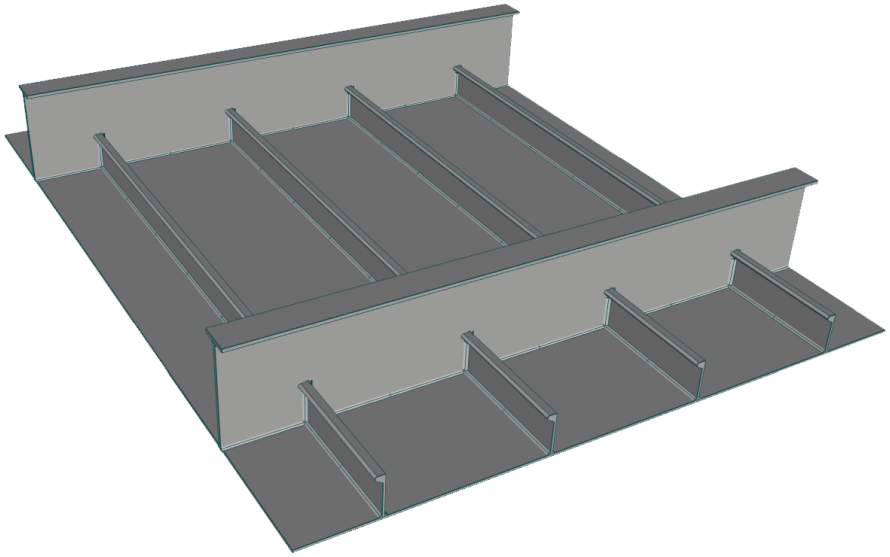

Figure 18 - Studied stiffened plate, composed by two girders and four stiffeners

4.1.1. MAIN DIMENSIONS AND MATERIALS

Starting the description with the base plate, its dimensions are 1500 mm in length, 1200 mm width and 4 mm thickness. Over the base plate two girders are disposed, with a spacing of 1000 mm, and four stiffeners, with a spacing of 300 mm. The girders are T profiles composed by 6 mm thickness welded plates, with 200 mm height for the web and 60 mm width for the flange. Stiffeners are HP3.7x80 profiles, meaning 3.7 mm thickness and 80 mm height. These profiles are visually represented in Figure 19.

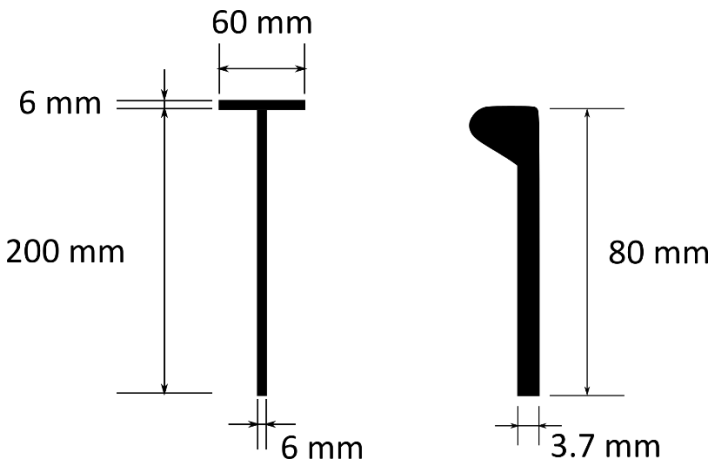

Figure 19 - Dimensions of girder and hp profiles

This stiffened panel is composed by two aluminum alloys. Base plate and webs are made of Al 5457 0/H111, while flange and stiffeners are made of Al 6082 T6. The main mechanical and thermal properties of these materials are given in Table 1, which was passed by Damen. It is important to highlight the similarity of these materials, which have near properties as density, elasticity modulus and thermal expansion. The other properties have a considerable difference, like thermal conductivity that presents almost 20% of variation and tensile strength with 50%.

	Aluminum 5754 0/H111	**Aluminum 6082 T6**
Density $[kg/m^3]$	2660	2700
Melting point $[°C]$	600	555
Modulus of Elasticity $[GPa]$	68	70
Thermal expansion $[m/K]$	2.40E-05	2.40E-05
Thermal conductivity $[W/m.K]$	147	180
Yield Tensile strength $[MPa]$	160 - 200	295

Table 1 - Materials main properties

4.1.2. WELDING BEADS

The objective of this project is the simulation and optimization of a large structure. The main feature of this stiffened plate is the number of weld beads, which enables to classify it as a large structure. There are 166 beads in total, joining the girders and stiffeners to the base plate and the girders web to the flange. In the experiment, stiffeners and girders were firstly tacked before welding, but this procedure was not considered in the simulation model. The main nomenclature of the weld beads is presented in the next figure:

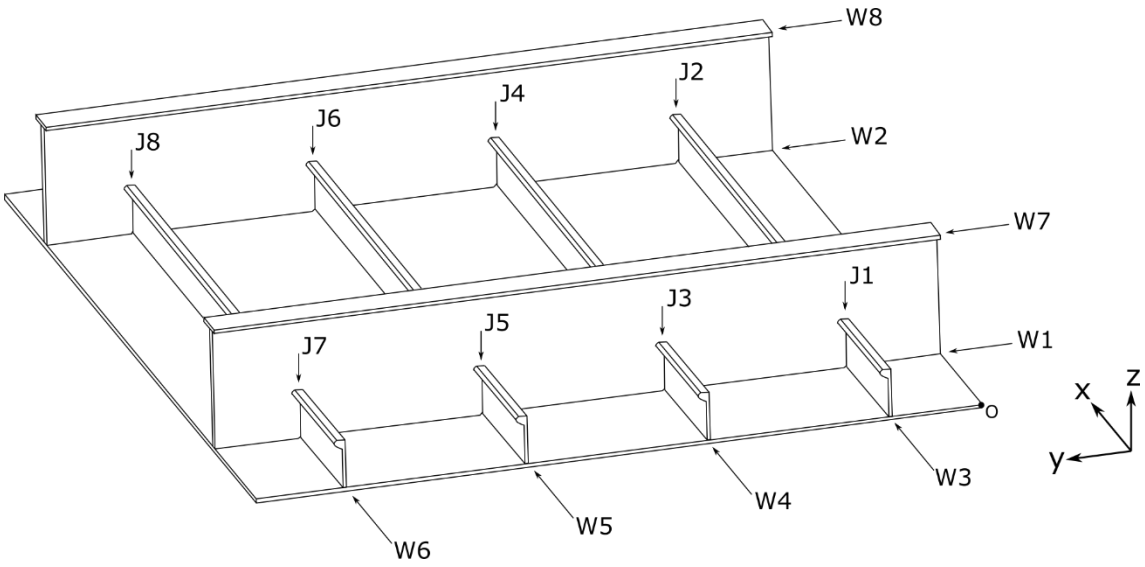

Figure 20 - Weld beads main nomenclature

There is a secondary classification for the beads, as there are beads on both sides of horizontal welding lines and four beads for the vertical welding lines. For the horizontal beads, the classification is made by a simple Fore (F) and Aft (A) prefix and a number that represents the position of the bead. For the vertical beads the classification is also made by a Fore and Aft system, but instead using a number as the second prefix, it is used a second Fore and Aft system. The adopted system is presented next:

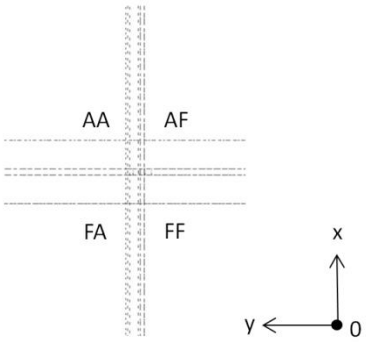

Figure 21 - Vertical beads nomenclature convention

For the joining of the parts was used a MIG procedure, using 100% argon gas as shield. During the experiment, welding parameters were kept constant. However, variations on the weld beads are observed, as the travel speed is varied from for bead. The parameters used in the welding process are given in Table 2. The variations also may become from the variation of the power supplied by the welding machine. Using these given parameters, we see that there is a minimum of 2120 W, when both parameters are minimal, and a maximum of 3270 W when both parameters are on its maximum.

Welding Parameters	
Voltage [V]	25 ± 5
Amperage [A]	106 ± 3
Wire Speed [mm/s]	12.2

Table 2 - Welding parameters used in all welding processes

The first beads to be exposed are the beads belonging to W1 and W2 welding lines. These beads are responsible for the joining of girders to the base plate. On each side, there are eight weld beads, as depicted in Figure 22.

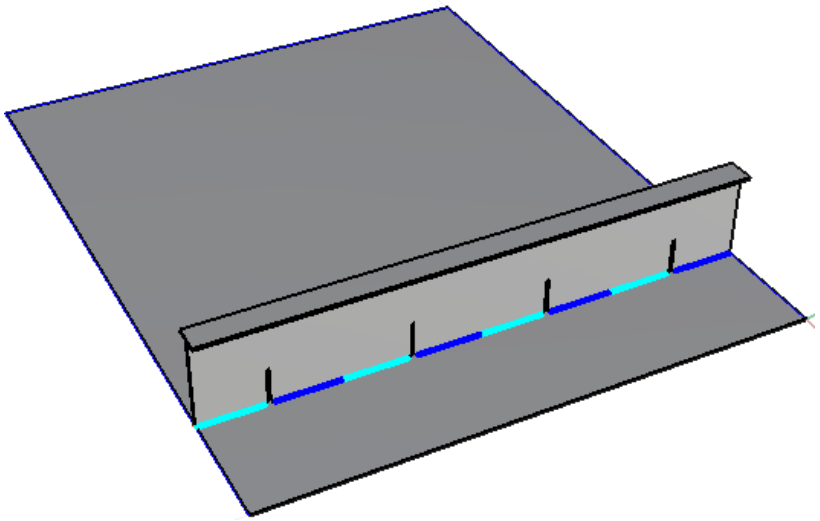

Figure 22 - Weld beads of W1 and W2 welding lines

Considering upward as the positive direction of x-axis and right to left the positive direction of the y-axis, the beads of W1 and W2 welding lines are named as:

W1A8	W1A7	W1A6	W1A5	W1A4	W1A3	W1A2	W1A1
W1F8	W1F7	W1F6	W1F5	W1F4	W1F3	W1F2	W1F1

Figure 23 - Identification of W1 weld beads

W2A8	W2A7	W2A6	W2A5	W2A4	W2A3	W2A2	W2A1
W2F8	W2F7	W2F6	W2F5	W2F4	W2F3	W2F2	W2F1

Figure 24 - Identification of W2 weld beads

The experiment resulted in different sizes of weld beads, in both length and throat. This resulted from the adoption of different traveling speeds and welding machine fluctuations, as mentioned before. As the focus of the project is the optimization of welding sequence using a local/global method, the beads were homogenized to group them into one local model. The original characteristics of each bead are given in APPENDIX A.

.

For the model, the length of the beads is given by an equal division of the free space on the welding line. This resulted in 142 mm in length for each bead. For the throat, was used the mean value, given by 3.55 mm. The profile of the weld bead for W1 and W2 welding lines is given next:

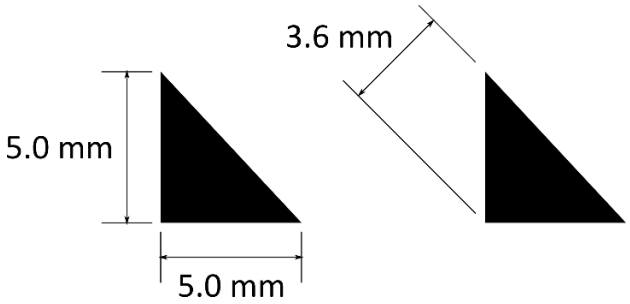

Figure 25 - Profile of W1 and W2 weld beads

The next is the longitudinal weld beads, which joins the stiffeners to the base plate. These beads belong to W3, W4, W5 and W6 welding lines and are 10 beads on each side. They are depicted in Figure 26. Following the same consideration for the axis, the nomenclature present in Figure 27 is for welding line W3, but may be extended to the other welding lines. The only change is the “W3”, modified to “W4”, “W5” or “W6”.

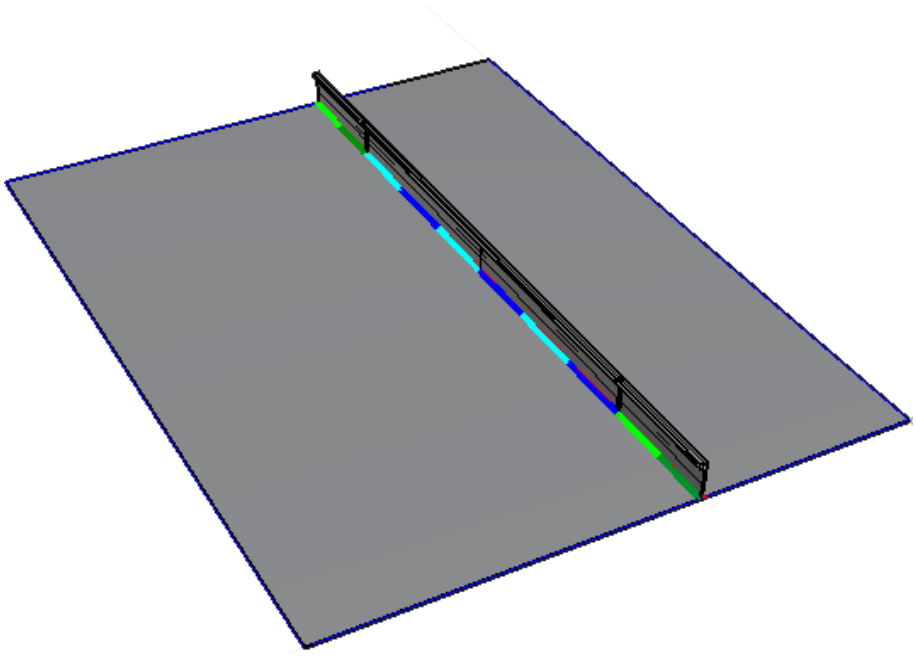

Figure 26 - Weld beads of W3, W4, W5 and W6 welding lines

W3A10	W3F10
W3A9	W3F9
W3A8	W3F8
W3A7	W3F7
W3A6	W3F6
W3A5	W3F5
W3A4	W3F4
W3A3	W3F3
W3A2	W3F2
W3A1	W3F1

Figure 27 - Identification of W3 welds beads

Again, the beads shape and characteristics vary from each other. The original information from these beads may be found in APPENDIX A. The same simplification was made in this case, homogenizing the beads shape. Here one difference is observed, the length of beads are different. For the beads that lie among the girders (blue beads in Figure 26), the length is equal to 166 mm. While 125 mm for the others (green beads in Figure 26). Although differences may be found in the length, the shape was kept equal for all beads in these welding lines. The mean throat is 4.06 mm, given resulting in the shape presented in Figure 28.

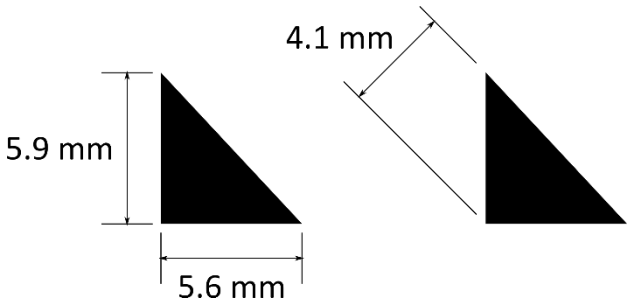

Figure 28 - Profile of W3, W4, W5 and W6 weld beads

W7 and W8 represent the welding lines that join the girder flange to the web. In these welding lines, the number of weld beads varies, being 5 beads on each side for W7 and 6 beads on each side for W8. In Figure 29 is seen the representation of W8 welding line. However, the only change for W7 is the number of weld beads.

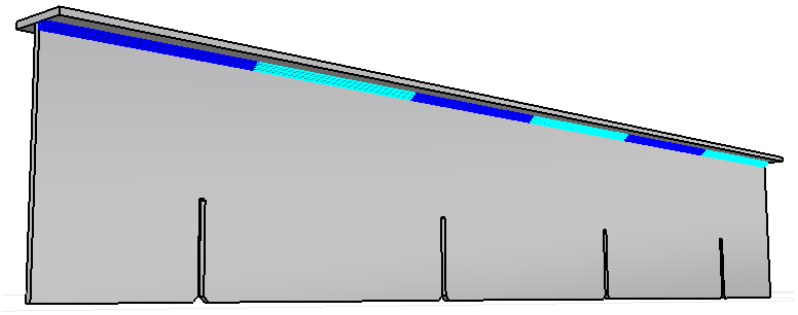

Figure 29 - Weld beads of W8 welding line

For the W7 welding line, the nomenclature is given by:

W7F5	W7F4	W7F3	W7F2	W7F1
W7A5	W7A4	W7A3	W7A2	W7A1

Figure 30 - Identification of W7 welds beads

And for the W8 welding line:

W8A6	W8A5	W8A4	W8A3	W8A2	W8A1
W8F6	W8F5	W8F4	W8F3	W8F2	W8F1

Figure 31 - Identification of W7 welds beads

The shapes of weld beads were simplified as done before for the other welding lines and original information may be found in APPENDIX A. Here differences are seen in the length of weld beds between welding lines W7 and W8. Due to the number of weld beads, the length for W7 is 240 mm and for W8 is 200 mm. The throat of weld beads is given by the mean value, equal to 4.04 mm, and the final shape is:

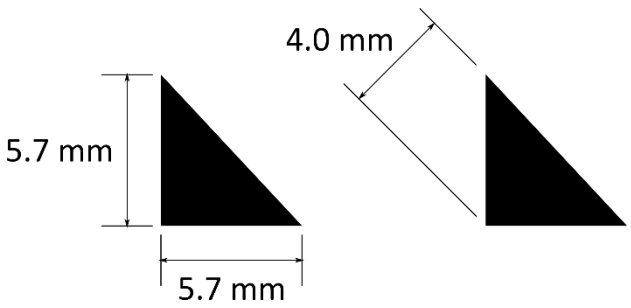

Figure 32 - Profile of W7 and W8 weld beads

The vertical beads, given by the welding lines J1 to J8 represents the assembly between girders and stiffeners. In this group of weld beads, there are 2 weld beads on each side. However, in this case, the beads are different in height from each other, as seen in Figure 33. The height for the short beads (light blue) is 58 mm and for the tall beads (dark blue) is 74 mm.

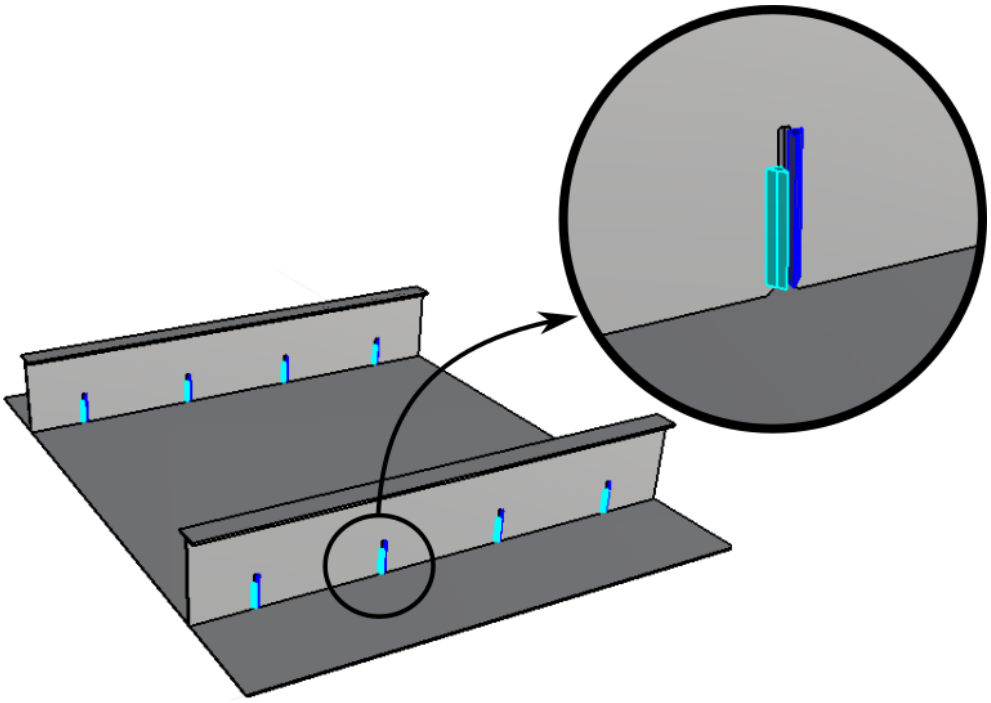

Figure 33 - Weld beads of J1 to J8 welding lines

Vertical weld beads identification is given in Figure 34. It is presented only the nomenclature for the J1 group. However, to identify the other groups, it is just necessary to change the “J1” for the respective group, as “J2” to “J8”.

J1AA	J1AF
J1FA	J1FF

Figure 34 - Identification of J1 to J8 welds beads

The shape simplification was made for all beads. Thus, the mean value comprises the short and tall beads throats, which is given by 5.18 mm. The original values and characteristics may be found in APPENDIX A. The shape of the beads is:

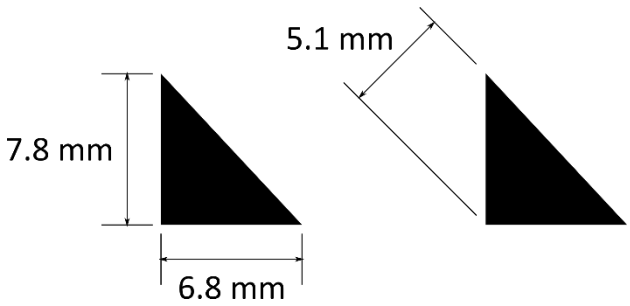

Figure 35 - Profile of J1 to J2 weld beads

4.2. LOCAL MODELS

As presented earlier in section 1, the first main step of the methodology is the creation of the local models. It is necessary to define how to group the weld beads, to set the simulation of each local model e and then run the models to obtain the distribution of distortions.

In this project, the groups of weld beads are almost defined by itself due to its characteristics. The first attempt of grouping is division in longitudinal welds (W3, W4, W5 and W6), transversal welds (W1, W2, W7 and W8) and vertical welds (J1,…,J8). However, the transversal welds considerably differ in shape between the flange/web and girder/plate beads. Hence, it is necessary to subdivide this group. Another problem is observed in the vertical welds group. Where the height of weld beads differs and may present a different distortion pattern due to proximity to the bulb profile. Thus, another subdivision is made in this group.

With these considerations, the groups of local models were created as described in the next table:

Model	Weld Lines
LM01	W3, W4, W5 and W6
LM02	J1...J8 - AA and FA
LM03	J1...J8 - FF and AF
LM04	W1 and W2
LM05	W7 and W8

Table 3 - Description of local models

Visually, the local models were stated as:

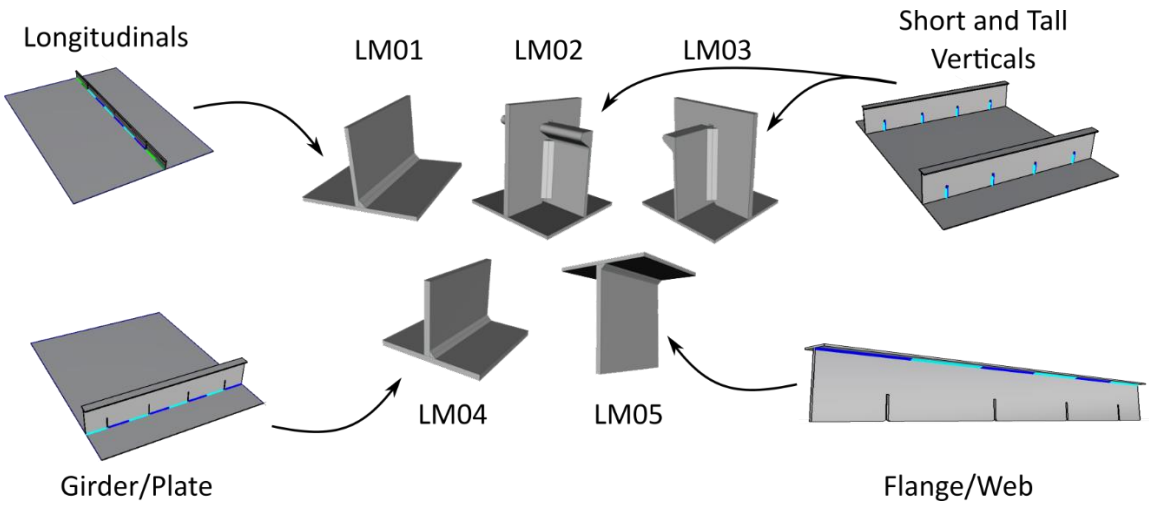

Figure 36 - Designed Local Models

One last parameter that was missing in the description of welding beads, made in the previous section, is the travel speed. It was calculated for each local model by the mean value and the results are presented in Table 4. The original values of travel speed for each weld bead are given in APPENDIX A.

	Travel Speed [mm/s]
LM01	11,4
LM02	8,8
LM03	9,6
LM04	15,2
LM05	12,9

Table 4 - Travel Speed for each model

The crucial step of this phase was the adjustment of the heat source for each simulation and it was made based on the throat and width of the weld bead. This means that the depth of the generated molten pool should be equal to the throat of the weld bead and the width of the molten pool should be equal to the width of the weld bead. Remembering that the Goldak heat source is defined by four shape parameters ($a_f, a_r, b\ and\ c$) and by the heat input (power), these are too much parameters to define based only on the bead throat and width. Therefore, some considerations are needed to reduce the number of parameters combination, as presented next:

$$a_r = 4a_f$$

$$b = a_f$$

This adopted approach was reported by Fu [60] and intends to reduce the number of variables in the heat source adjustment. In this consideration, only the front length and the depth are adjusted, the other parameters are linked to the front length. As mentioned before, the adjustment was made by trial and error method. This means that a great time was consumed in this phase, as the simulations need some hours to be completed. The combinations of parameters are shown in Table 5. It is important to highlight that in some cases, as in LM02 and LM03, was needed to disrespect the considerations mentioned above. In these cases, the defined width of the heat source was not enough to reach the width of the weld bead. Thus, some modifications were made.

Model	Power [W]	Travel Speed [mm/s]	af [mm]	ar [mm]	b [mm]	c [mm]
LM01	2850	11,4	1	4	1	1
LM02	3070	8,8	1	4	6	1
LM03	2900	9,6	1	4	6	1
LM04	3270	8,2	1	4	1	1
LM05	3270	12,9	1	4	1	1

Table 5 - Parameters obtained on the heat source adjustment phase

It is important to remark that LM04 did not form the proper molten pool, even with the maximum power (3270 W), and was needed to decrease its travel speed. This is possible due to the large difference present in the travel speed of each weld bead of the experiment. Therefore, this reduction will not interfere with the Global Analysis. It is important to emphasize that all models have efficiency equal to 100%.

The constraints for each model are the restriction of movement on the faces that were created by cutting the local model from the global model. Restrictions were made in all three directions, which also grants the restriction for rotation. This type of constraints is indicated by Virfac manual on local/global analysis.

Another important feature of the local models composition are the materials settings. The aluminum alloys used in the experiment were described earlier in section 4.1.1. However, the data required as input for Virfac were not available for the simulations. Another aluminum alloy was adopted as a solution, AA7075 presents similar characteristics with the original alloys. The differences in composition are depicted in Figure 37.

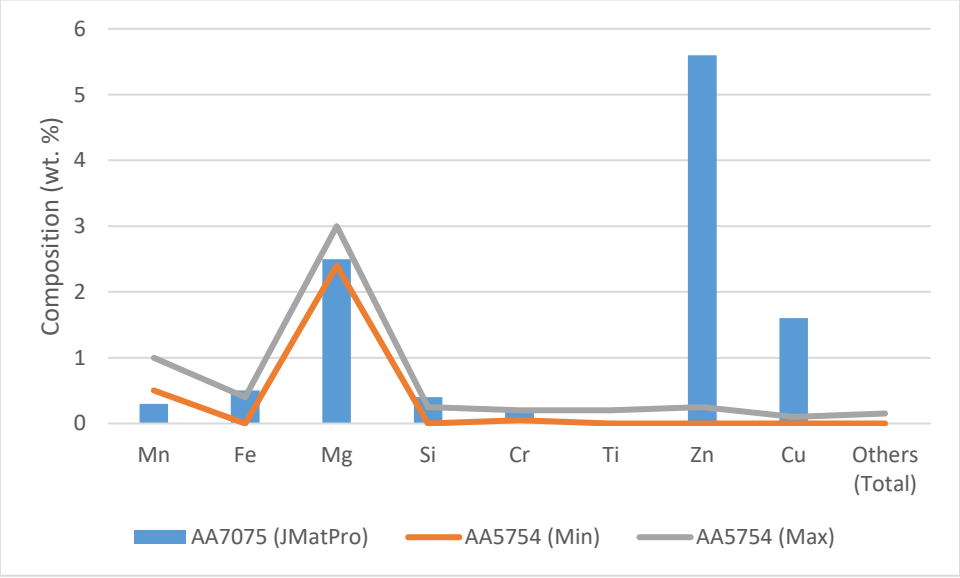

Figure 37 - Differences between aluminum alloys AA5754 and AA7075

As the composition of these materials are quite similar and the original one is not available, the aluminum alloy AA7075 was used for the simulations. Table 6 presents the features of each material under normal conditions, like room temperature. However, for the simulations are necessary the behavior of the material varying with the temperature. This type of data is difficult to obtain, which justifies the use of AA7075.

	AA 5754	**AA 6082**	**AA 7075**
Density $[kg/m^3]$	2660	2700	2810
Melting point $[°C]$	600	555	477 - 635
Modulus of Elasticity $[GPa]$	68	70	71.7
Thermal expansion $[m/K]$	2.40E-05	2.40E-05	2.34E-05
Thermal conductivity $[W/m.K]$	147	180	173
Yield Tensile strength $[MPa]$	160 - 200	295	228

Table 6 - Mechanical and thermal characteristics of aluminum alloys

Materials change its behavior by temperature variation, hence for thermo-mechanical simulations is required the properties of the material for a range of temperature. On Figure 38 are depicted Young's Modulus, Poisson Ratio, Yield Strength and Coefficient of Thermal Expansion. The physical properties Thermal Conductivity, Specific Heat and Density becomes on Figure 39. Are also presented the Hardening Coefficient and Hardening Exponent on Figure 40.

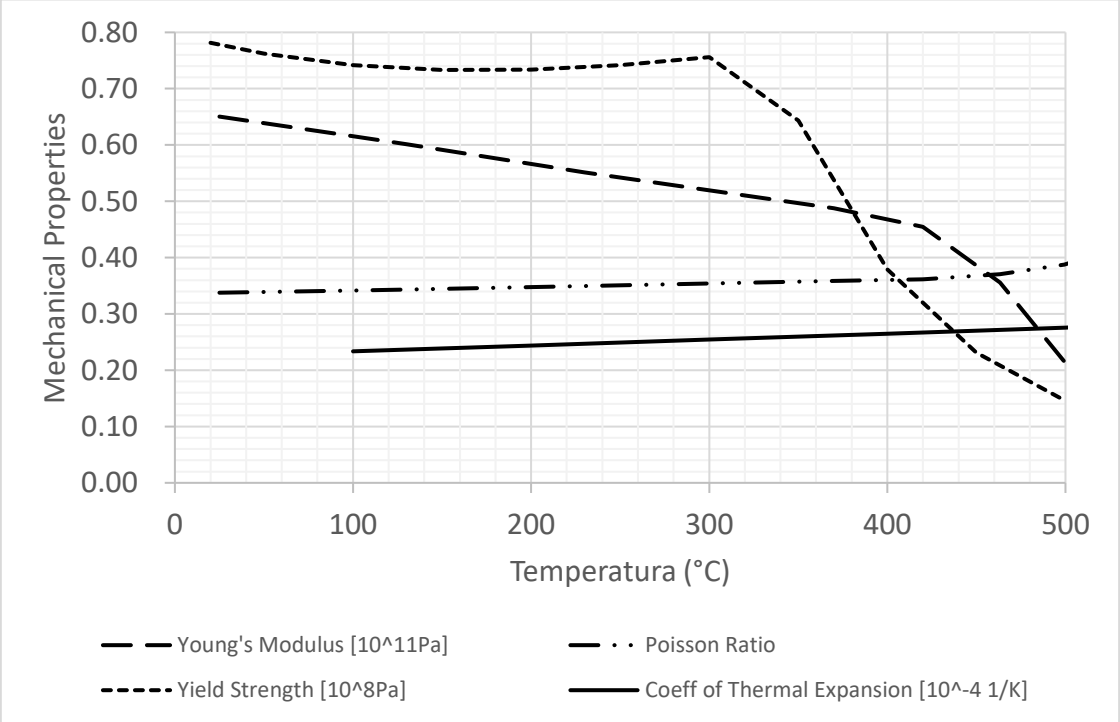

Figure 38 - Mechanical properties of AA7075 for temperature variation

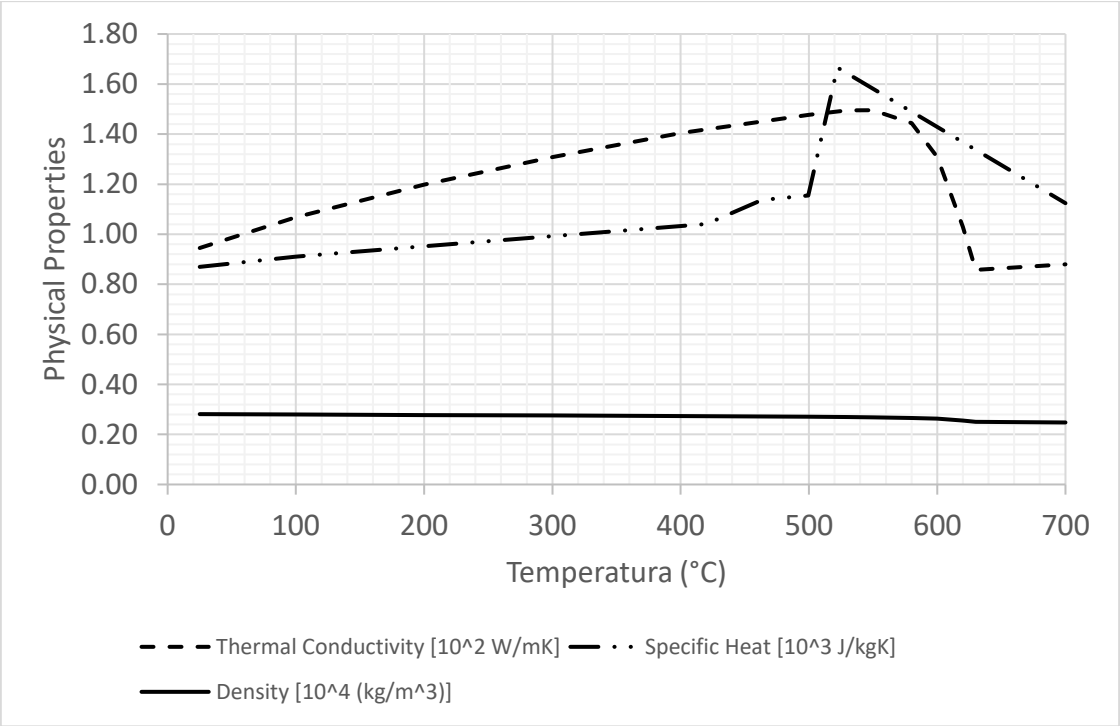

Figure 39 - Physical properties of AA7075 for temperature variation

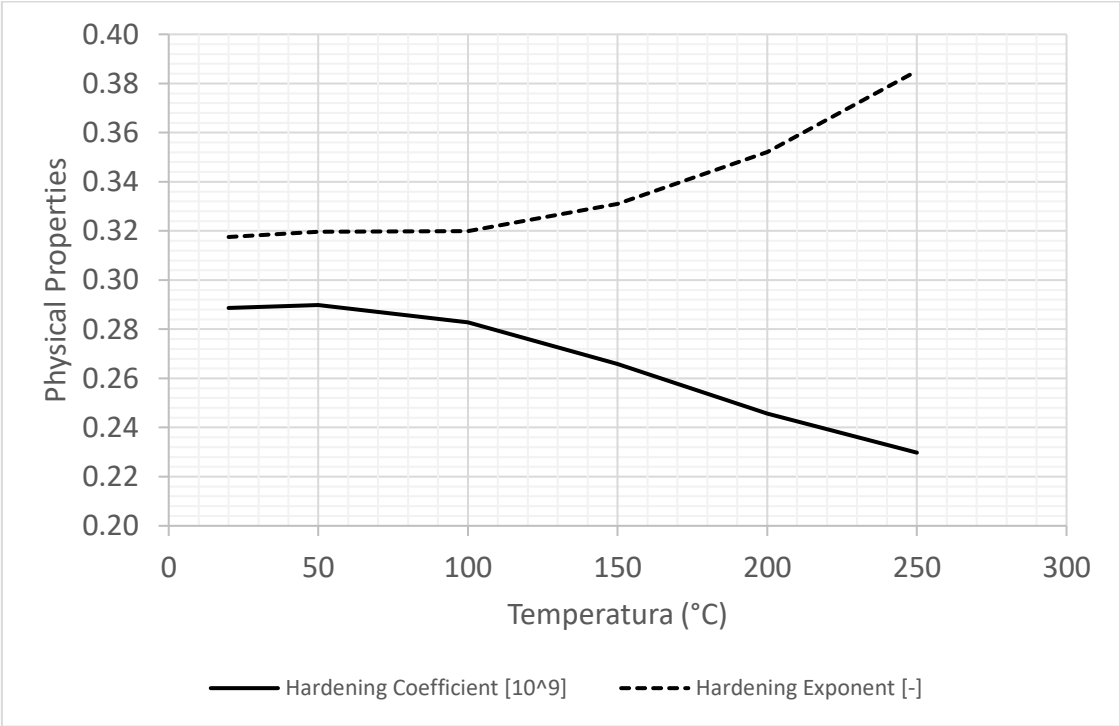

Figure 40 - Coefficients for the power law empirical relation

The local models were simulated on a cluster in Belgium, as our available computers were not capable to hold the simulations due to the refinement of the mesh. The used mesh had a maximum cell size of 6 mm and a minimum cell size of 0.5 mm. Also granting that inside a radius around the weld bead, the cell size should be equal to the minimum cell

size. This radius varied with the bead shape, going from 5.4 mm in LM05 to 7.7 mm in LM02 and LM03.

Local Models have an initial temperature of 17,8°C. This is the average ambient temperature of the experiment, which was carried in three days. Another necessary study was the cooling time needed to reach the initial temperature. This parameter was set as 1000 seconds, although the models did not reach the ambient temperature, they ended with temperatures around 30°C. The problem of setting large cooling times is that the time consumption grows considerably.

4.2.1. LOCAL MODEL RESULTS

Local models were run on a cluster at Belgium as a partnership with GeonX, decreasing the time spent in this phase. Normally, the evaluated results for welding simulations are the shrinkage and bending of the base plate. However, the considered boundary conditions do not allow this study. All of the displacements were constrained on the faces that were created on the local models.

In order to assess the behavior of the local models after the welding simulation, the displacements were captured over two lines. One longitudinal, right under the weld bead, and a second transversal to the weld bead. Both lines are parallel to the base plate. Next will be presented the local models and its respective axis orientation, followed by the displacements, in mm, over the defined lines.

Local Model 01

Axis orientation:

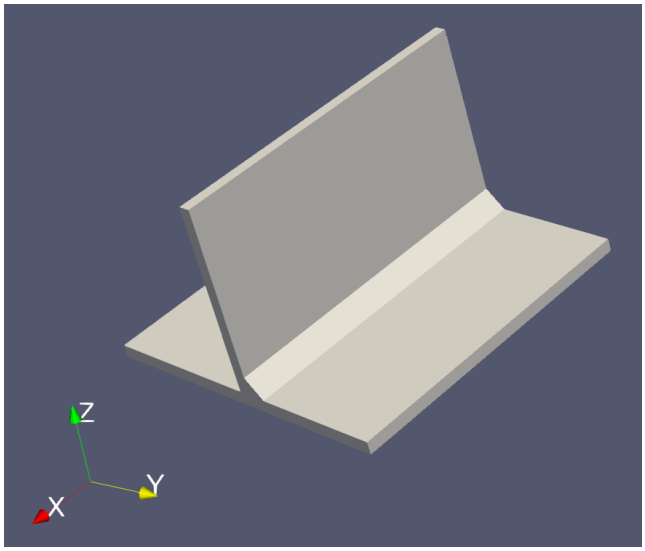

Figure 41 - Axis orientation for Local Model 01

Studied lines:

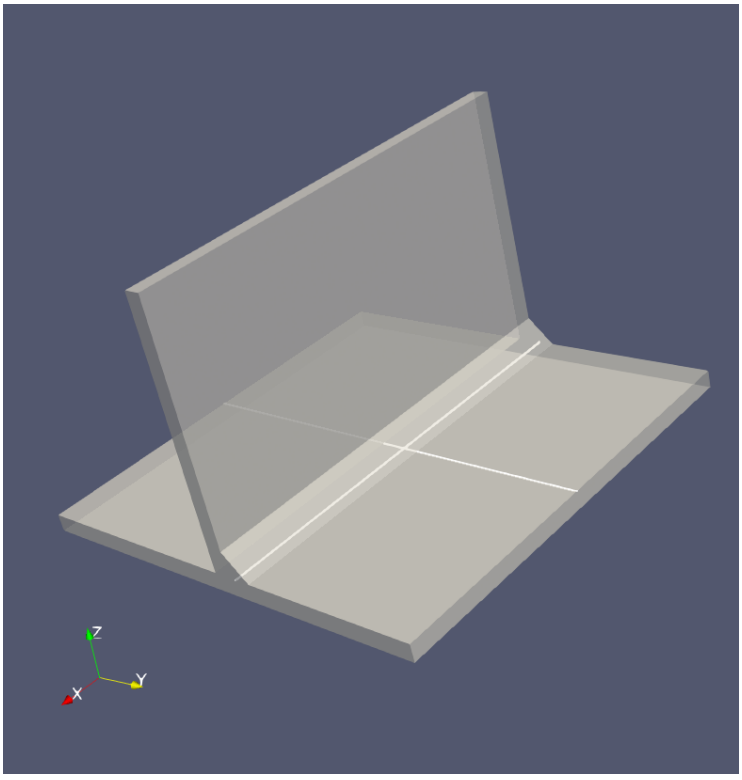

Figure 42 - Longitudinal and transversal lines for Local Model 01

Results for the longitudinal line:

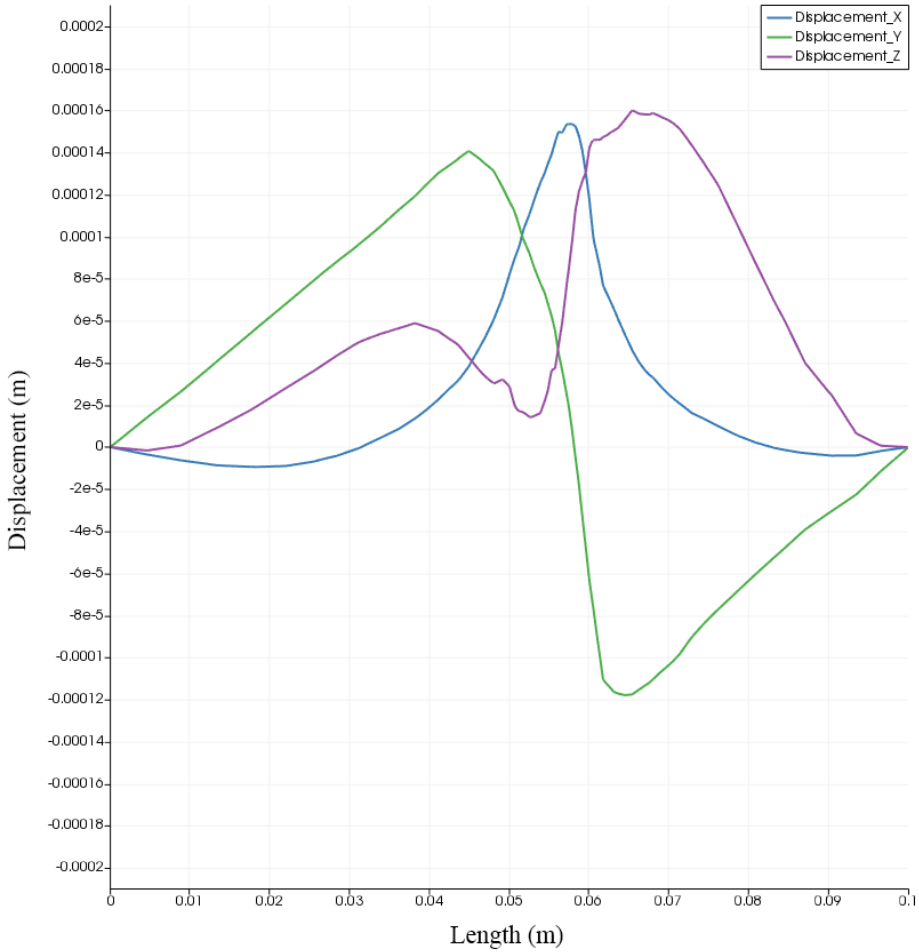

Figure 43 - Displacements for longitudinal line in Local Model 01

Results for the transversal line:

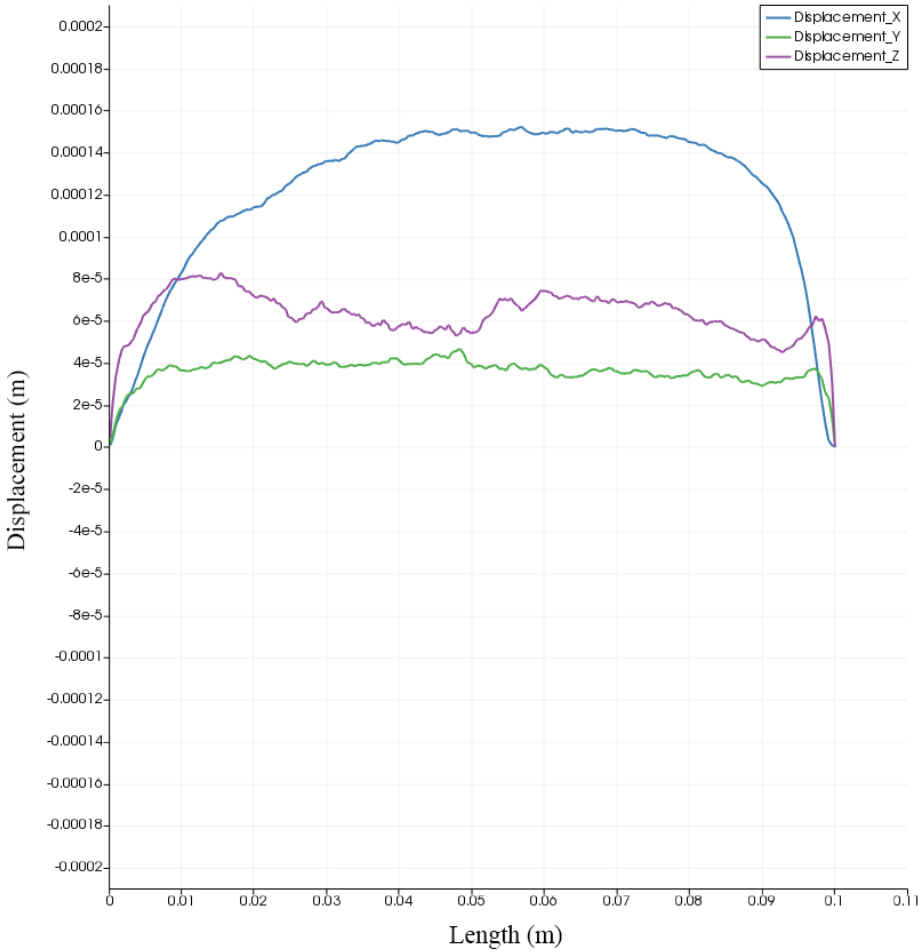

Figure 44 - Displacements for transversal line in Local Model 01

Local Model 02

Axis orientation:

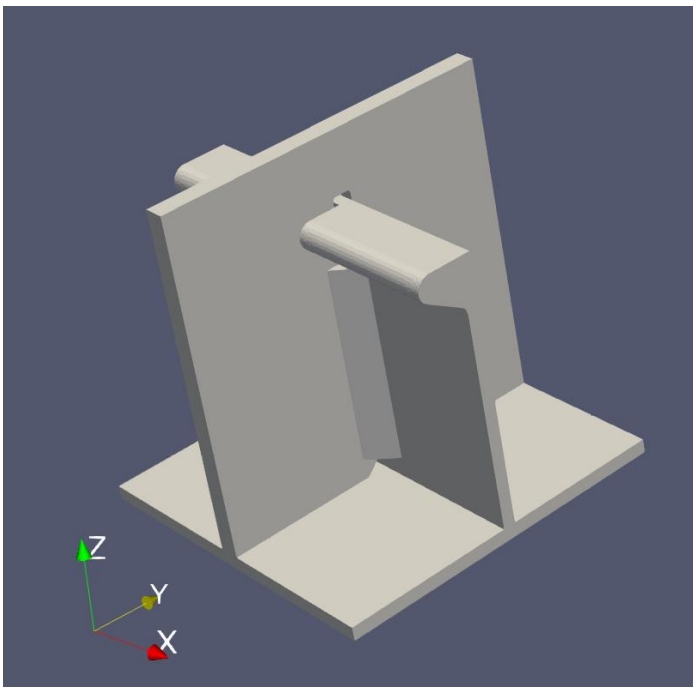

Figure 45 - Axis orientation for Local Model 02

For this local model were considered two longitudinal and two transversal lines. The first set of longitudinal and transversal lines considered the plate as a base plate. The second set considered the stiffener as the base plate:

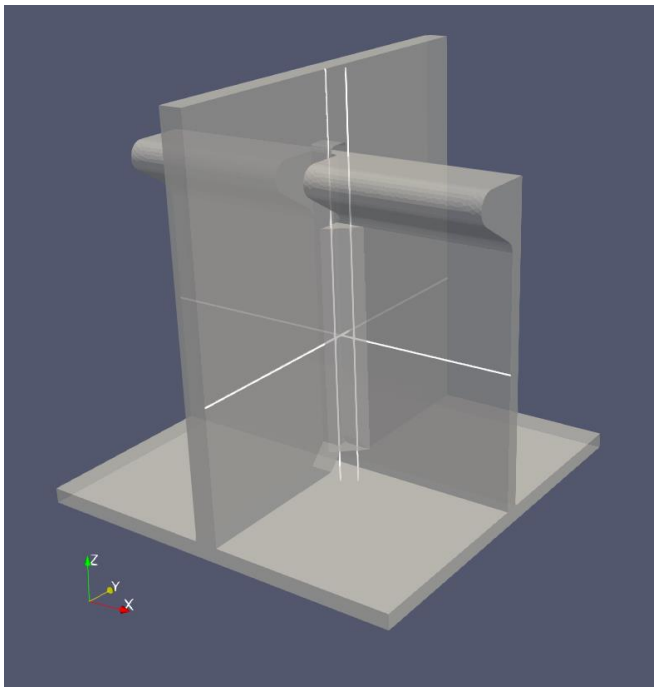

Figure 46 - Longitudinal and transversal lines for Local Model 02

For the first longitudinal line:

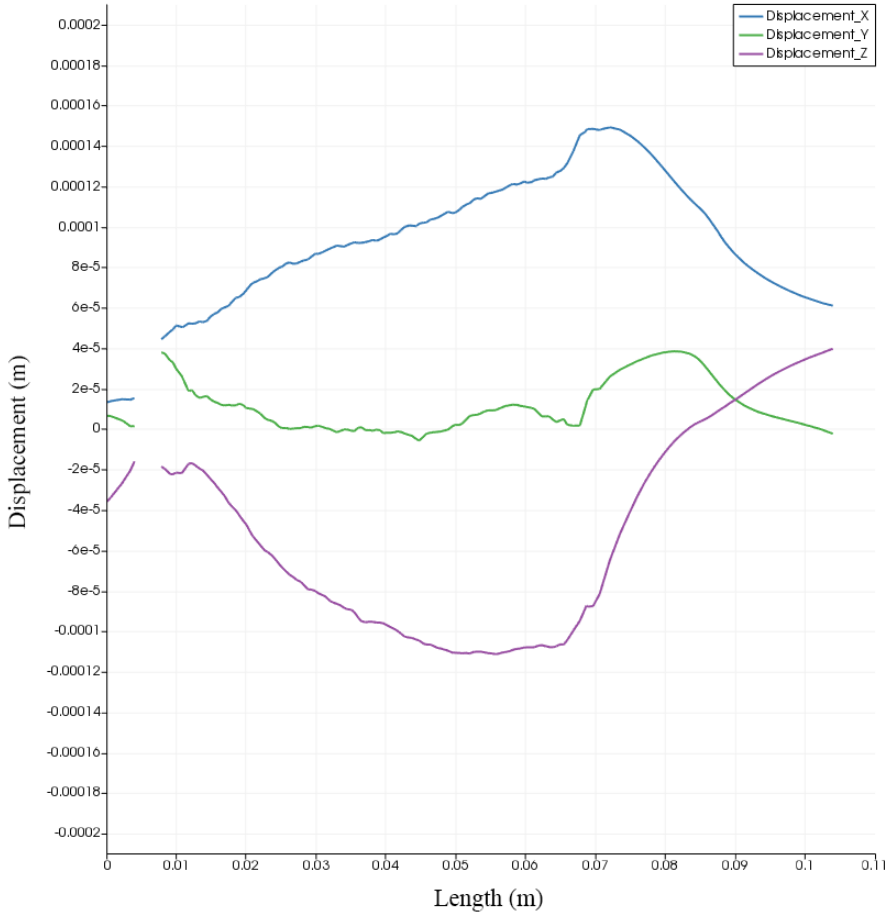

Figure 47 - Displacements for the first longitudinal line in Local Model 02

For the first transversal line:

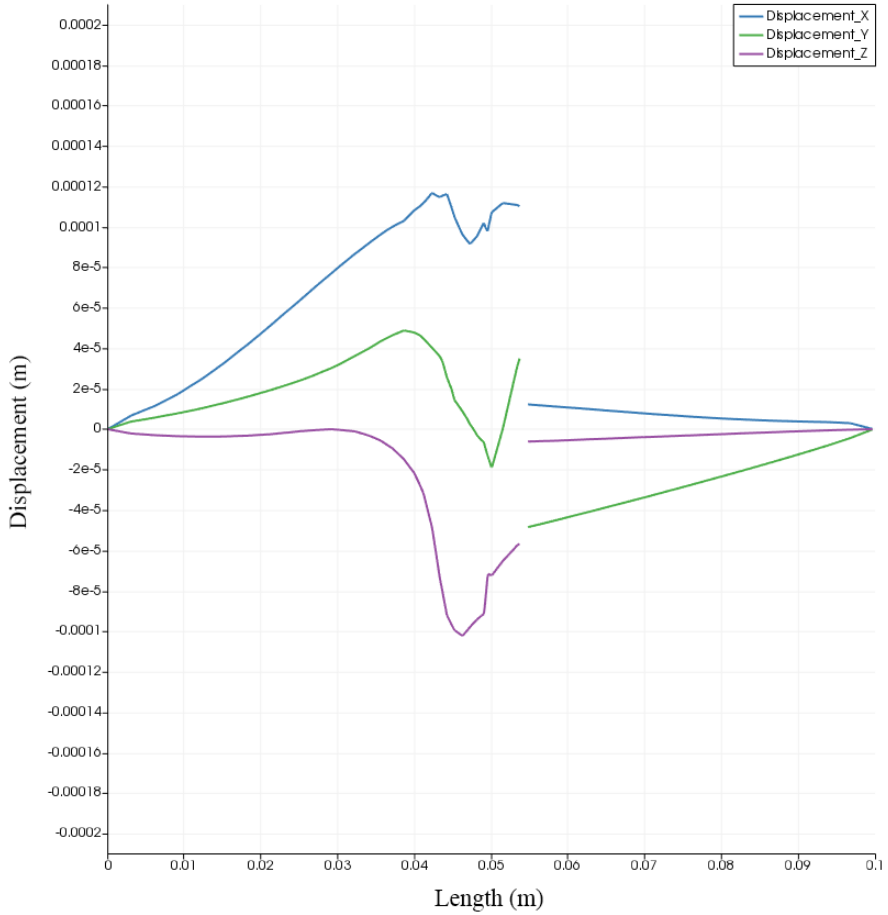

Figure 48 - Displacements for the first transversal line in Local Model 02

For the second longitudinal line:

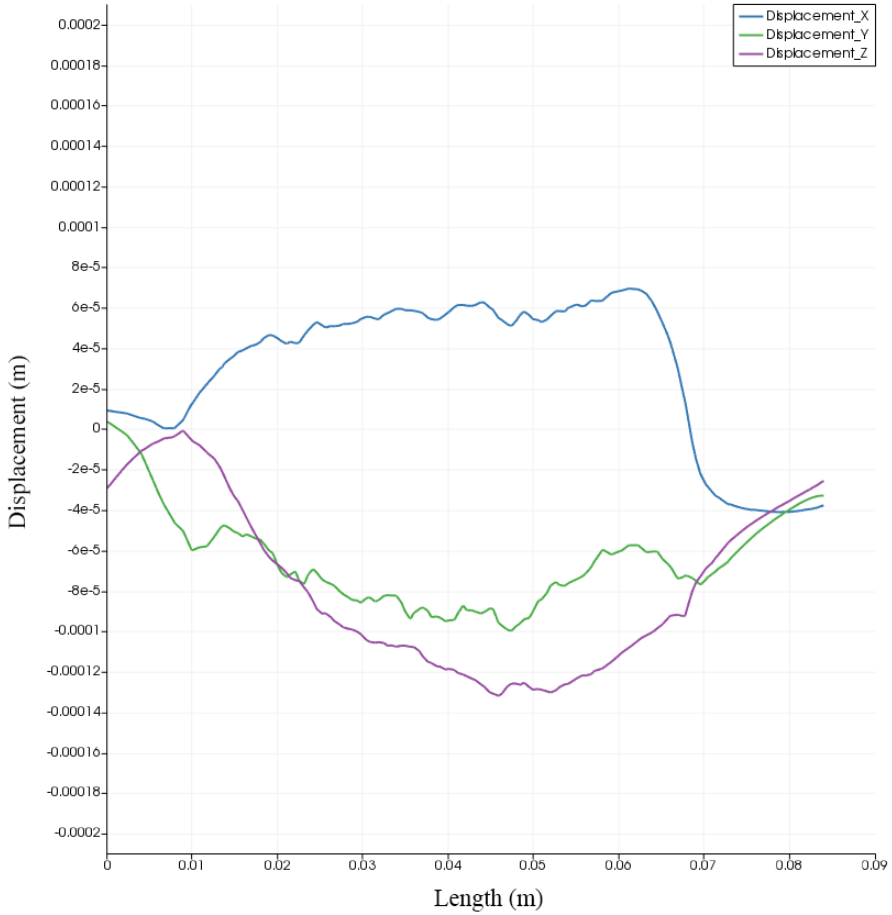

Figure 49 - Displacements for the second longitudinal line in Local Model 02

For the seconds transversal line:

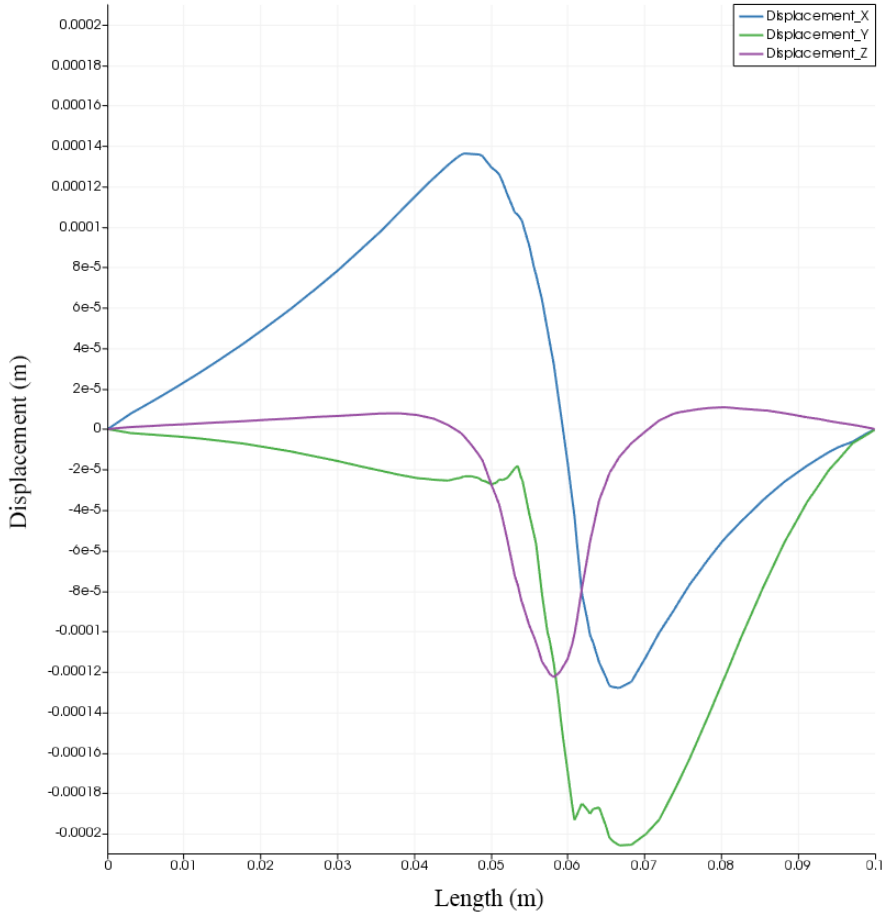

Figure 50 - Displacements for the second transversal line in Local Model 02

Local Model 03

Axis orientation:

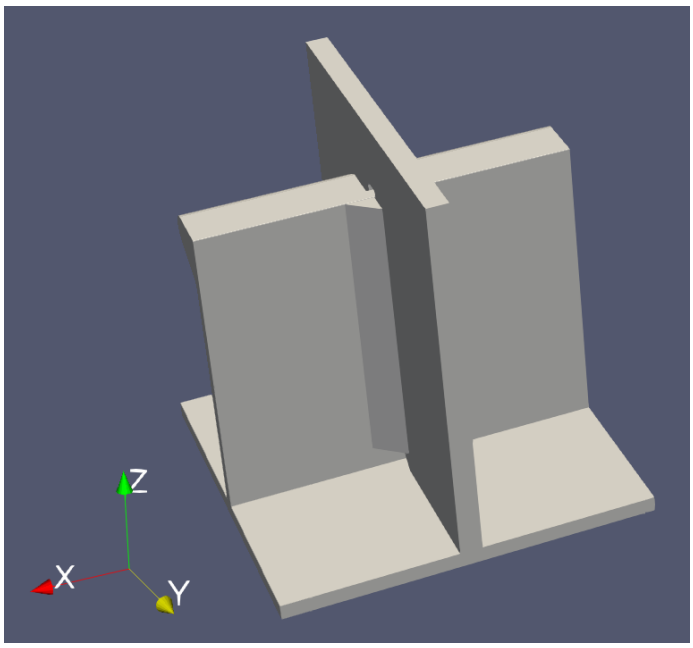

Figure 51 - Axis orientation for Local Model 03

In this case, were also considered two sets of longitudinal and transversal lines, as defined on LM02:

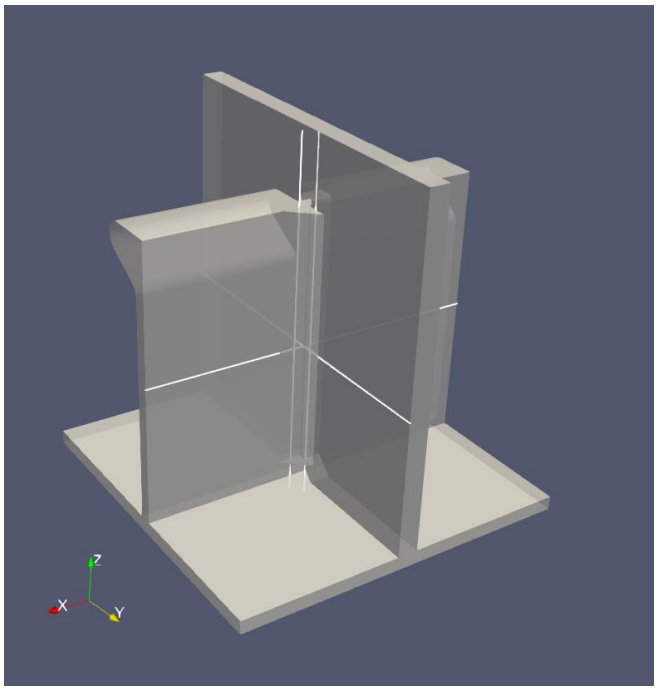

Figure 52 - Longitudinal and transversal lines for Local Model 03

For the first longitudinal line:

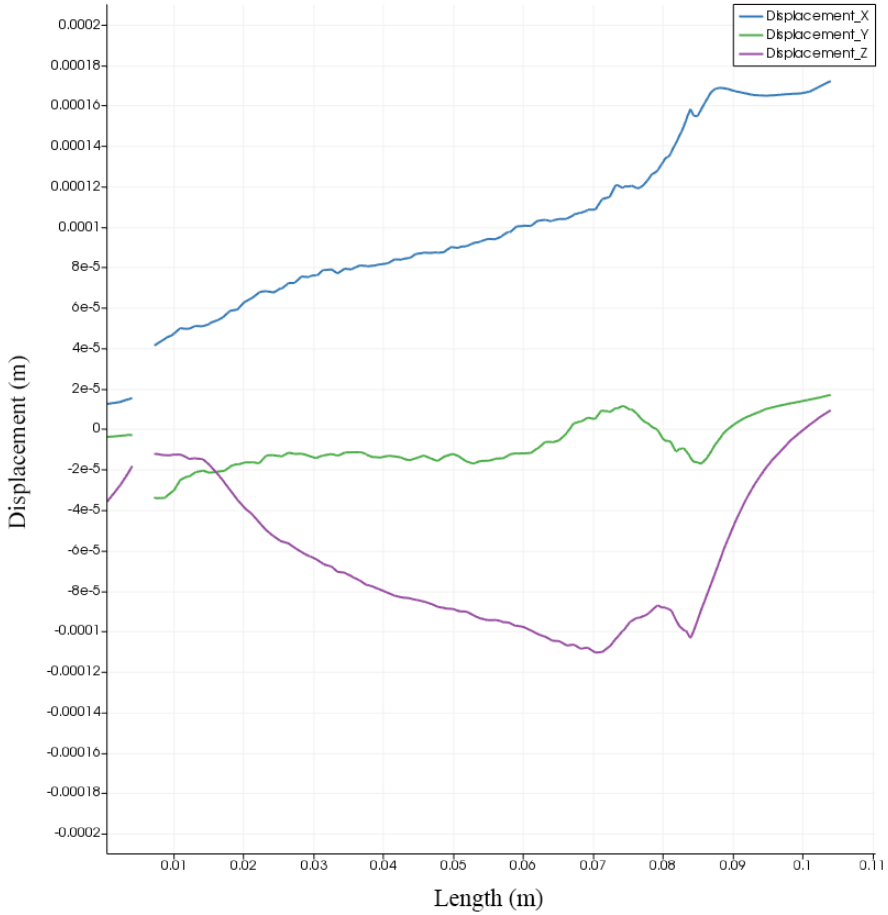

Figure 53 - Displacements for the first longitudinal line in Local Model 03

For the first transversal line:

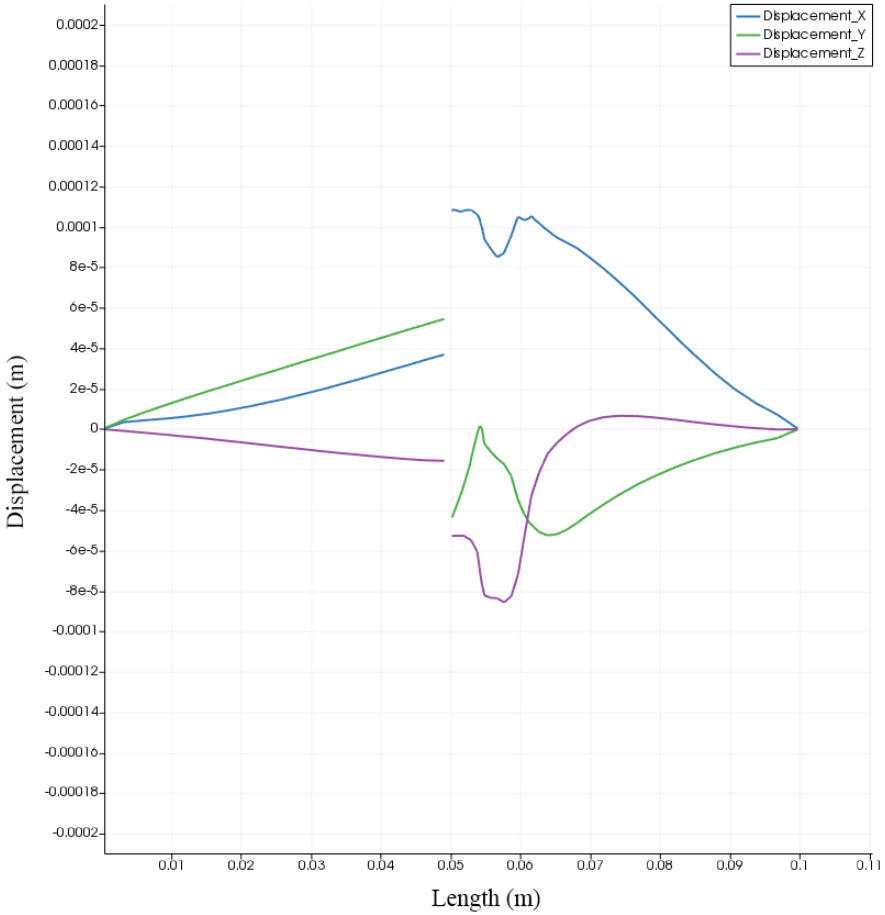

Figure 54 - Displacements for the first transversal line in Local Model 03

For the second longitudinal line:

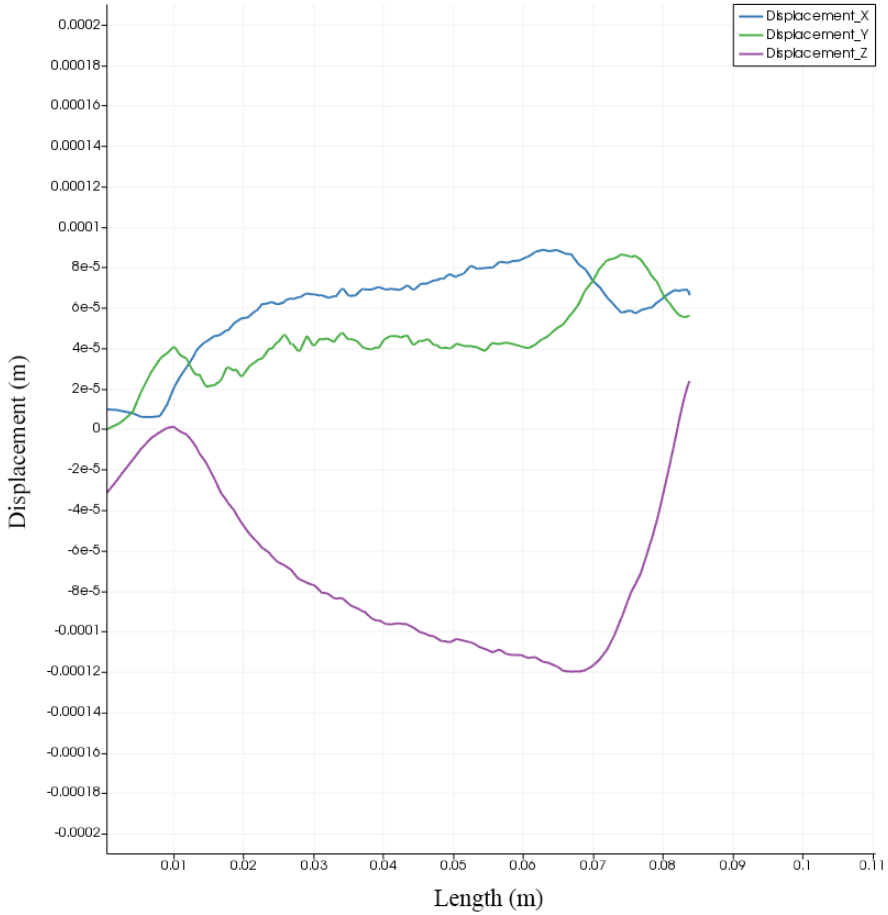

Figure 55 - Displacements for the second longitudinal line in Local Model 03

For the second transversal line:

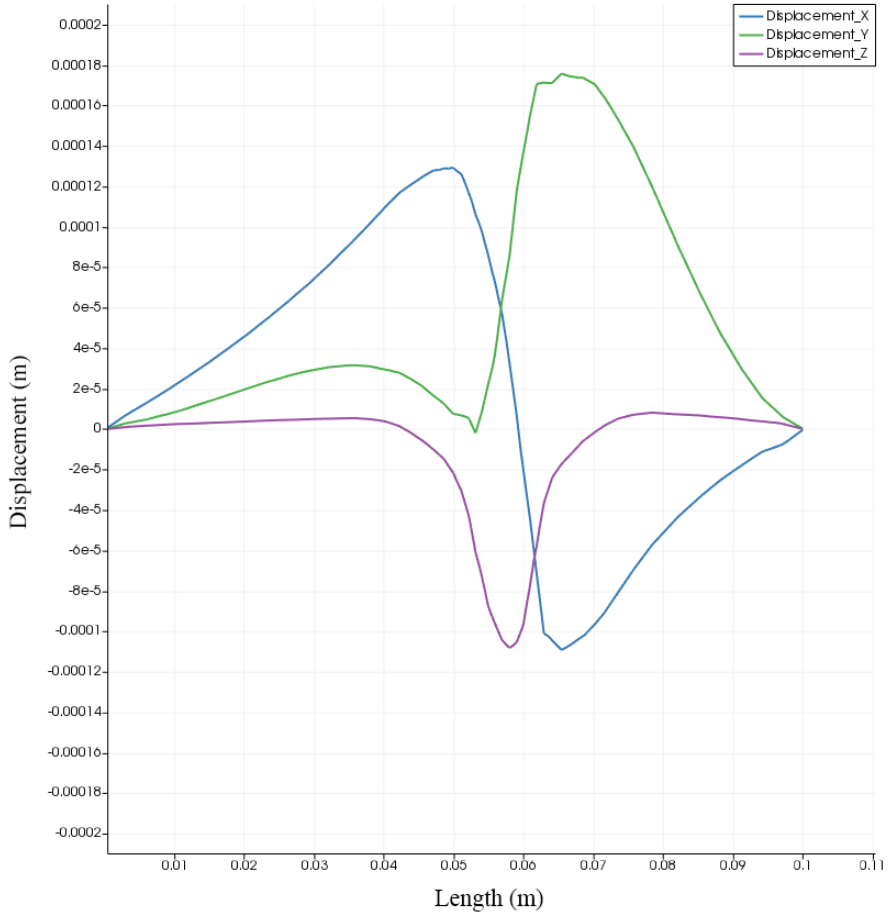

Figure 56 - Displacements for the second transversal line in Local Model 03

Local Model 04

Axis orientation:

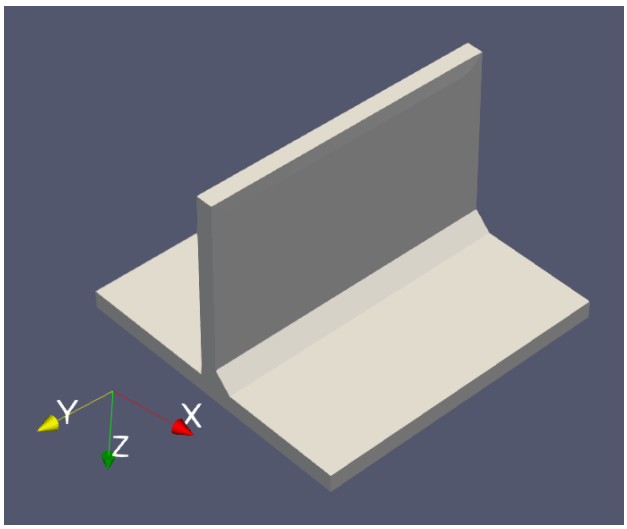

Figure 57 - Axis orientation for Local Model 04

Studied lines:

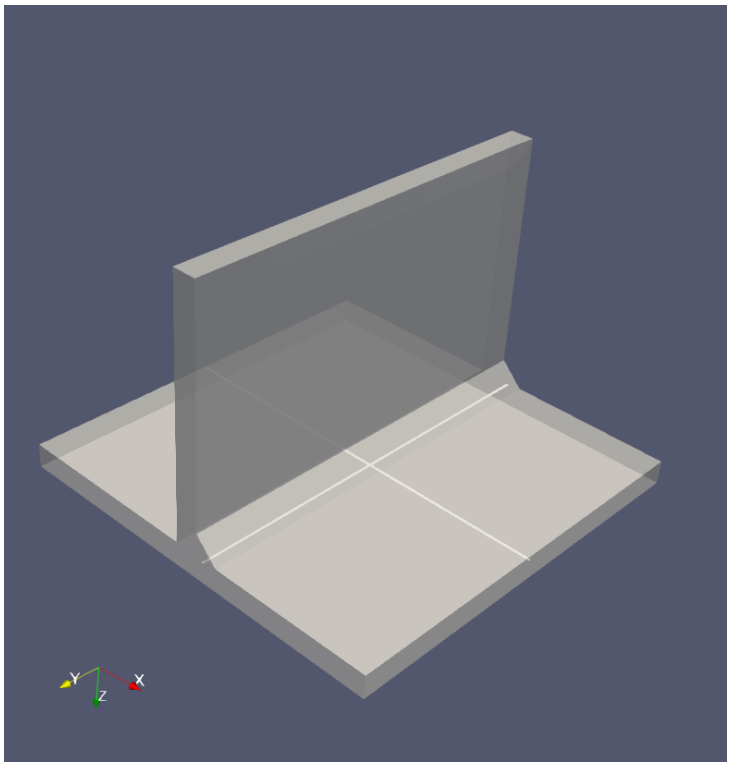

Figure 58 - Longitudinal and transversal lines for Local Model 04

For the longitudinal line:

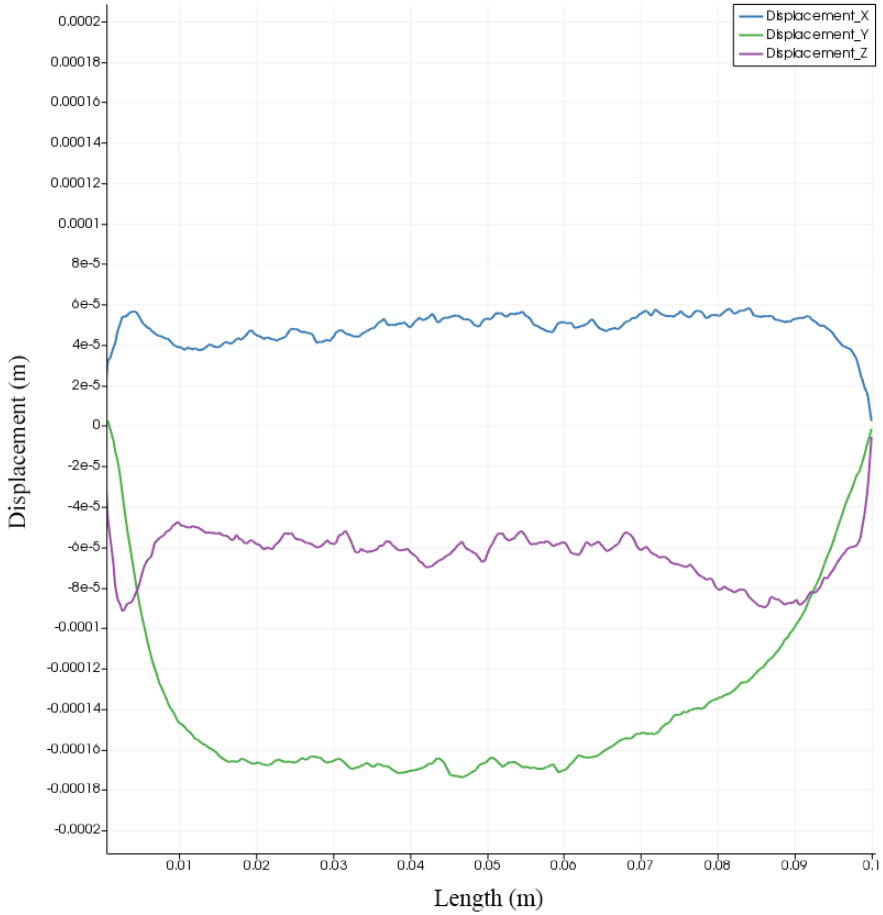

Figure 59 - Displacements for longitudinal line in Local Model 04

For the transversal line:

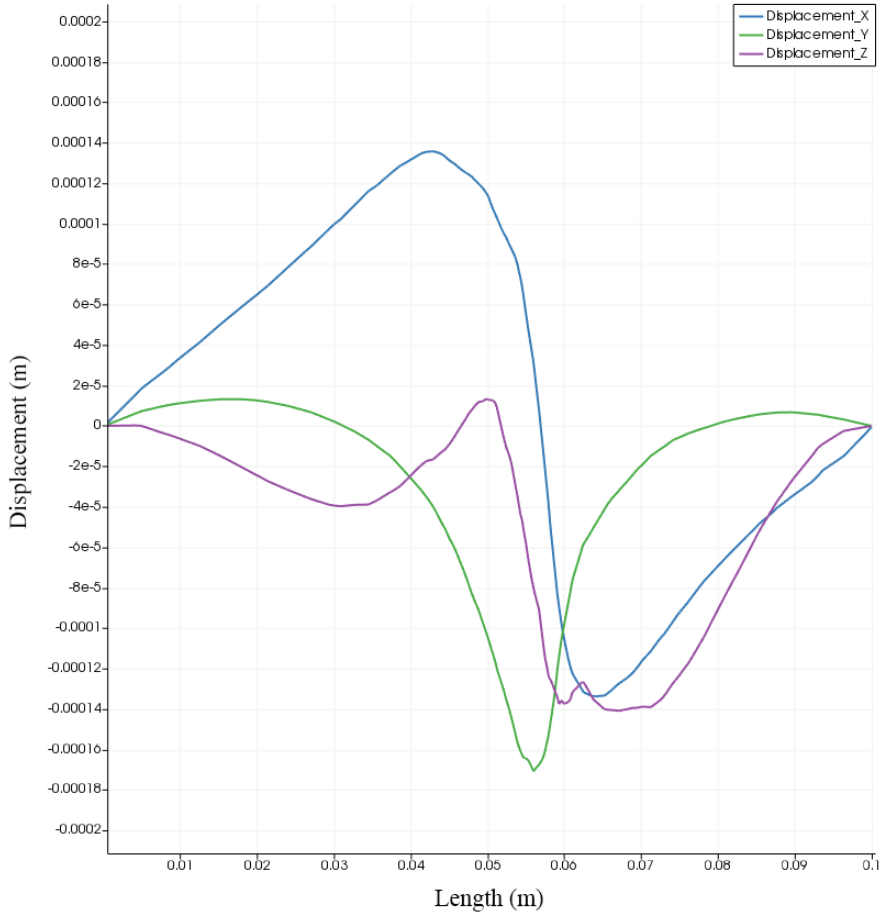

Figure 60 - Displacements for transversal line in Local Model 01

Local Model 05

Axis orientation:

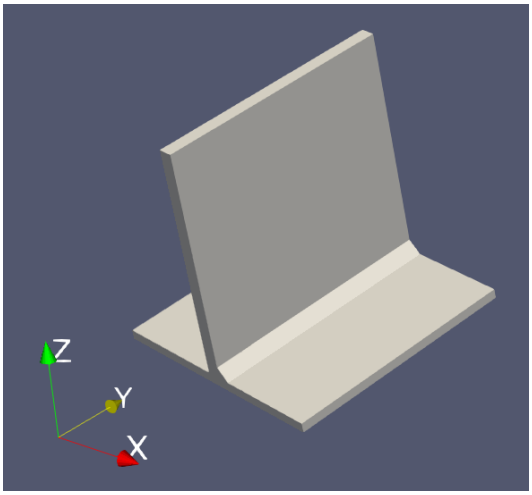

Figure 61 - Axis orientation for Local Model 05

Studied lines:

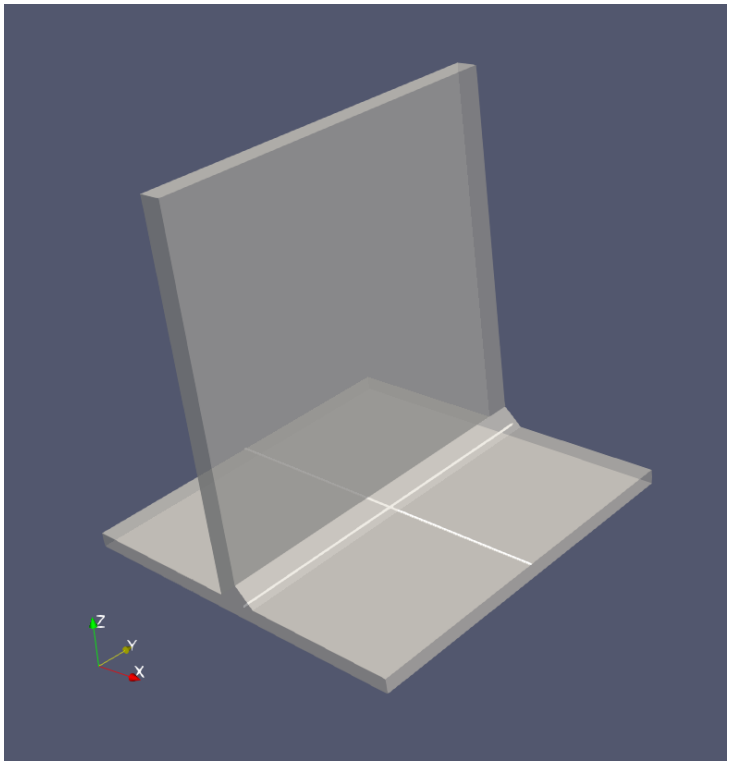

Figure 62 - Longitudinal and transversal lines for Local Model 05

For longitudinal line:

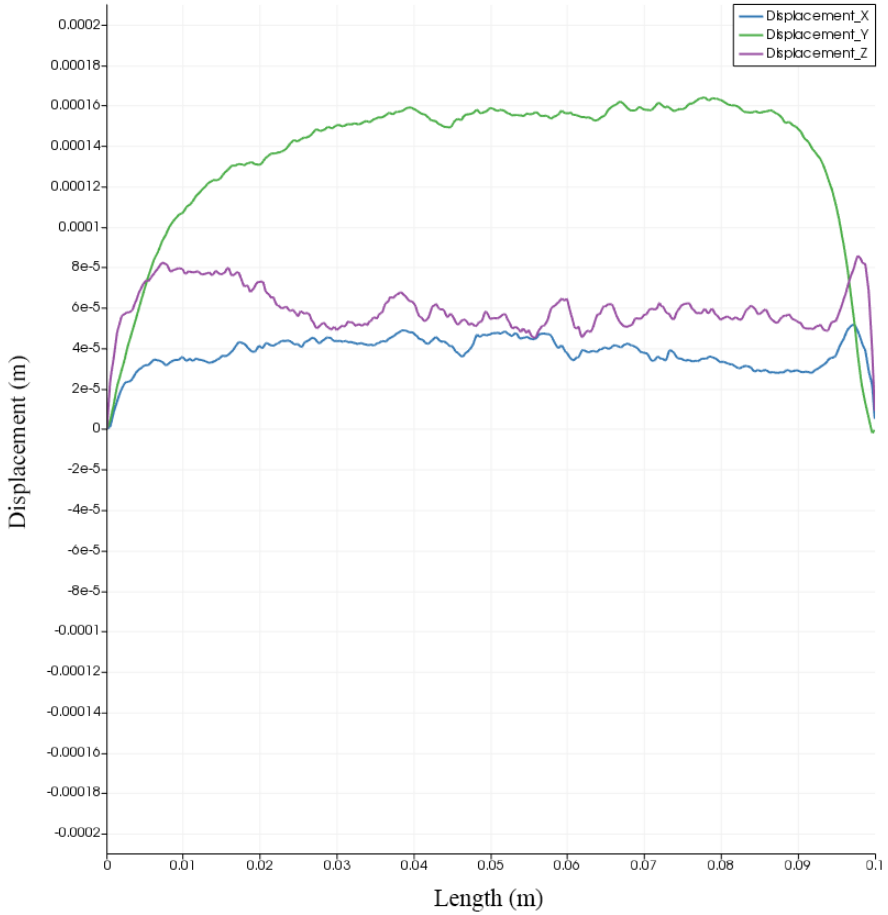

Figure 63 - Displacements for longitudinal line in Local Model 05

For the transversal line:

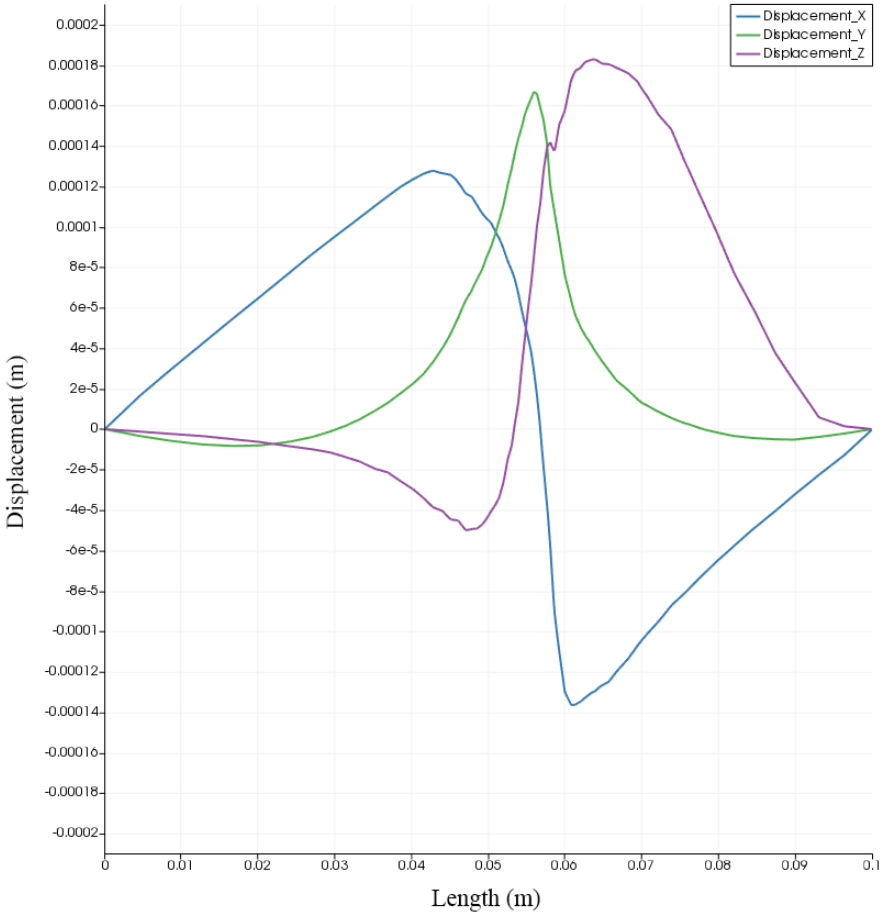

Figure 64 - Displacements for transversal line in Local Model 05

4.3. GLOBAL MODEL

4.3.1. GENERAL SETTINGS OF THE GLOBAL MODEL

Initially, the method of the project was designed to run an optimization of the global model using Virfac welding module. This method depends on external optimization software. However, during the project execution was launched a new version of Virfac, which includes an optimization module.

This new feature of Virfac is based on Jweld, a solver developed by JSOL [61], and have some different approaches. The main difference is that Jweld uses shell elements to represent the model, which reduces the time spent in a simulation. For the purpose of the project, this new tool represents a possibility to improve on the number of iterations on the optimization. Therefore, was decided to adopt this new module to the project.

In addition, the module presents an optimization code, which is specifically designed for welding optimization. This optimization code is based on Xtreme technology [59], explained in section 2.6.2. Was also decided to adopt the optimization code to the project method, as it would accelerate and facilitate the implantation of the optimization.

For this new welding module, a new global model was necessary. Figure 65 depicts the generated model, only based on 2D elements. In the software, it is possible to determine the thickness of each face. However, emerged a problem with the HP profile stiffeners. They were unable to be represented in this software. To overcome this, these stiffeners were transformed into flat bars by the inertia.

Rhinoceros was used to calculate the moment of inertia of the HP profile, giving $2.7 \times 10^{-7}\ m^4$. Thus, the correspondent flat bar may be calculated by:

$$I = \frac{bh^3}{12}$$

Rearranging:

$$h = \left(\frac{12I}{b}\right)^{1/3}$$

For the flat bar, b is the thickness. Keeping the same thickness of the HP profile, which is 3.7 mm:

$$h = \left(\frac{12 \times 2.7 \times 10^{-7}}{3.7 \times 10^{-3}}\right)^{1/3}$$

$$h = 0.096\, m$$

This calculation allowed the creation of the model that is presented next:

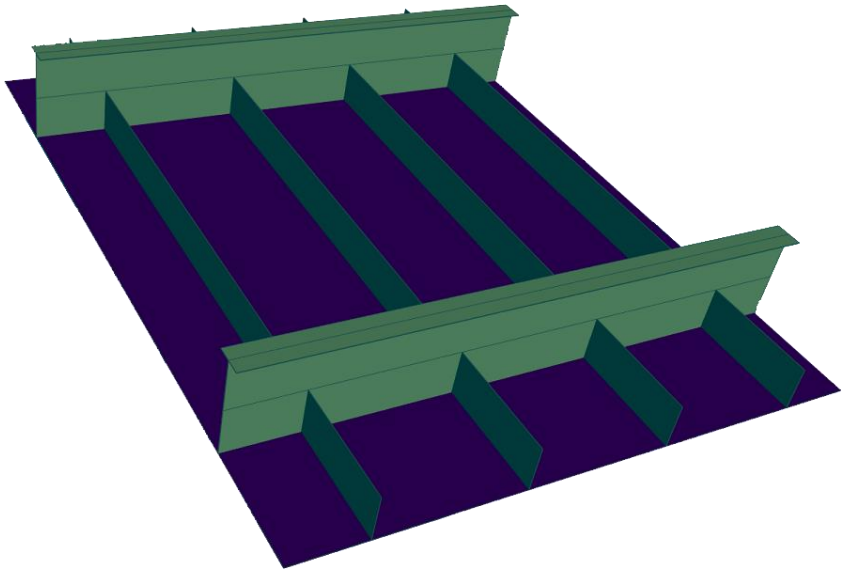

Figure 65 - Global Model constructed for Jweld solver, only composed by 2D elements

An important setting of the model are the constraints. For the global model was used a group of constraints that works as a free supported condition, which tries to simulate the real condition of the experiment. Figure 66 shows the used restraints that consist of one extreme point with movement restraint on three directions, another restrained on longitudinal and vertical directions and a last one restrained on the vertical direction. These constraints were used by Caprace [24] and restraints translation and rotation on all three directions. However, no other regions of the base are restricted, only the three defined points.

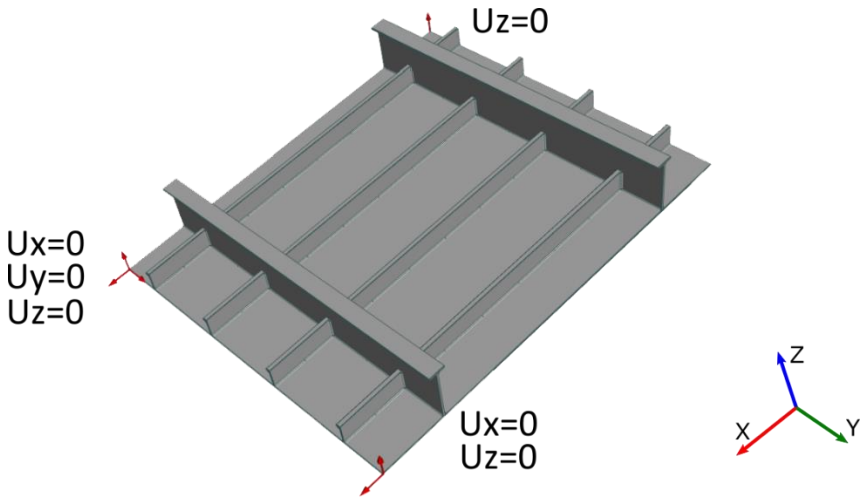

Figure 66 - Constraints for the Global Model that works as a free supported condition

4.3.2. INHERENT STRAINS DATABASE

The results obtained in the simulations of local models need to be imported to Virfac database. Based on the inherent strain method, this procedure is made by Mega Inverse module. At the end of importation, Virfac presents a comparison between the imported results and the original data from local models. Therefore, the configuration of the parameters that will be presented next is based on these results.

Importation starts by sectioning the weld bead, dividing it into smaller portions. All local models were equally sectioned into four parts. The sections were defined by the length or height of the weld bead, starting at 0% and going through 25%, 50%, 75% and ending in 100%.

The next important parameters are the sampling points, as presented in Figure 67. These points are distributed along seven longitudinal lines, one in the middle of the base plate, two on each side of the base plate and two on the web. The settable parameters are the number of points in each longitudinal line, the distance between points and distance between lines.

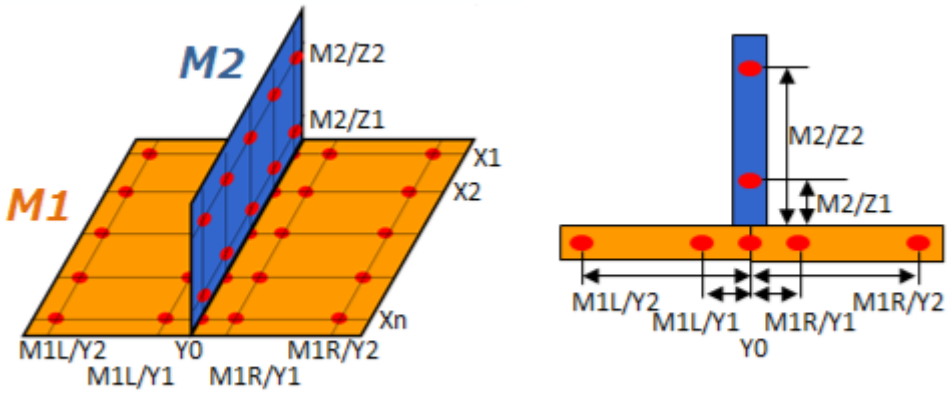

Figure 67 - Scheme of sampling points distribution

For all local models were used ten points, starting at 10% of the length and ending at 90% of the length. These points are all equally spaced by 18,9% of the length. The lines on the base plate are distributed on 10% and 90% of the width of each side. For the lines on the web, also the 10% and 90% of the height were used. The obtained model may be seen in Figure 68, which represents the Local Model 01 (LM01). The same configurations were used for other models, which presented better results when compared to the original data.

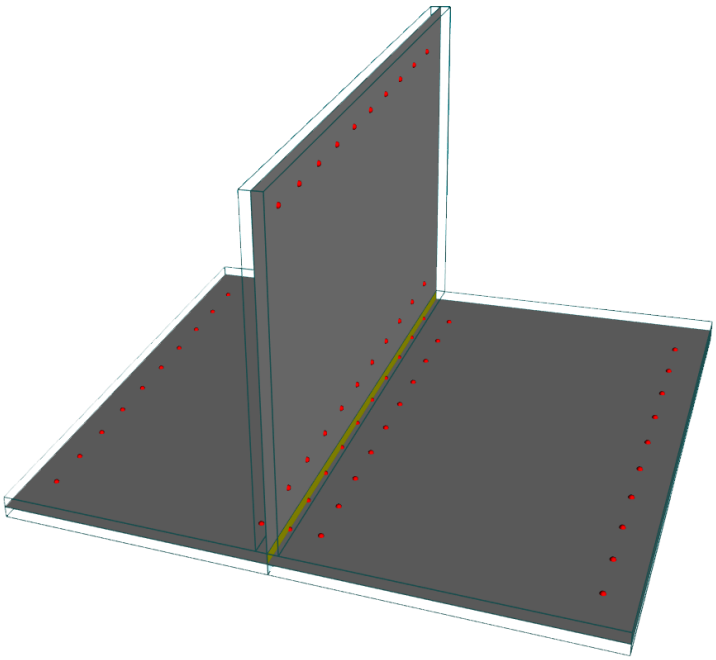

Figure 68 - Configuration of Local Model 01 with 10 sampling points

Results obtained for each local model presented a similar behavior, with good agreement when compared to the original data. The assessed data are the displacement and rotation over the X and Y axes for each point. Only rotation over X axis had a deviation from the original data. This behavior was present on all models, although was the best achieved

during the importation of inherent strains. The comparison of imported and original results may be seen in Figure 69 and Figure 70.

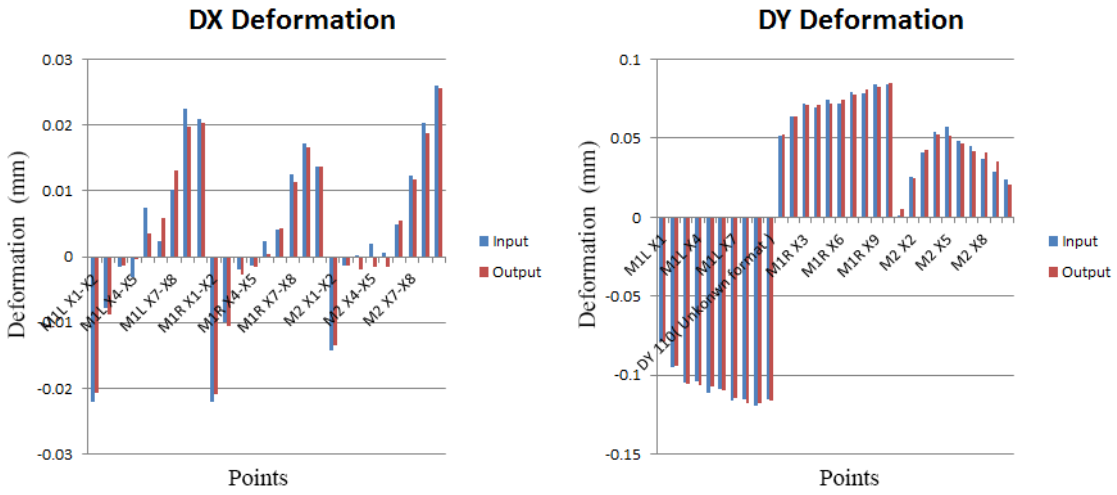

Figure 69 - Comparison of imported and original displacement for LM01

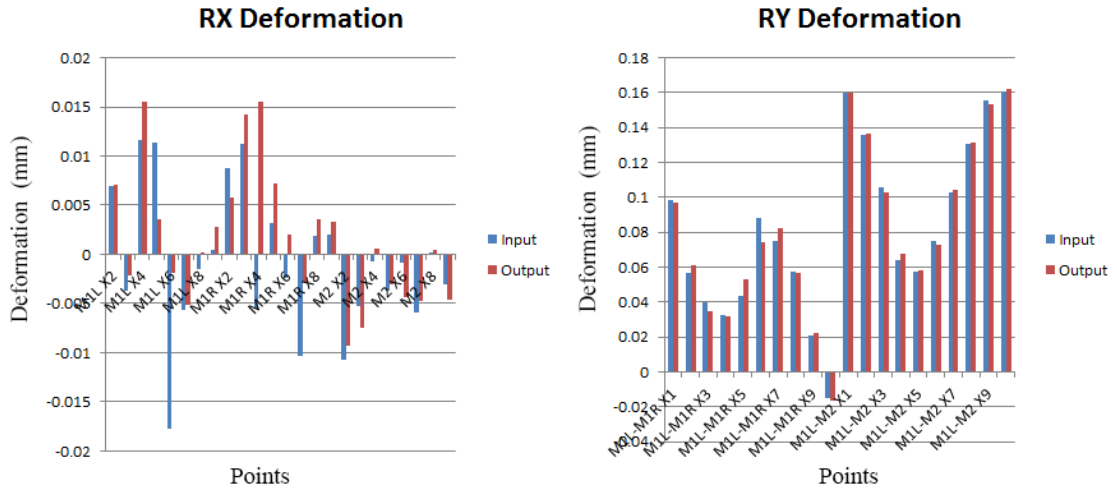

Figure 70 - Comparison of imported and original rotation for LM01

4.3.3. WELDING SEQUENCE

The original welding sequence, made by DAMEN, was an experimental sequence, greatly differing from the patterns used in shipyards. As the aim of the procedure was to evaluate the induced distortions, a non-standard welding sequence would be better. The original sequence is presented in APPENDIX B, due to the elevated number of entries, it will not be effectively presented here in the text, but a brief description.

Although the sequence is not a usual one, some patterns are adopted. It may be seen by the steps present next:

1. W8 and W7 welding lines. These welding lines are responsible to join the respective flanges to the webs of the girders. One welding line is fully welded before the other is started. The sequence of welded beads does not follow a pattern, sometimes one bead is welded in one side (fore or aft) and followed by its matching on the other side. However, this pattern is not ever followed.
2. W1 and W2 welding lines. These welds make the assembly of girders to the weld plate. W1 is completed before W2 is started. Again, no pattern is observed on the welding sequence for each welding line.
3. W4 and W5 welding lines. These are the middle longitudinal welds that join the HP stiffeners to the base plate. As occurred on the other welds, W4 is completed before W5 starts and no pattern is observed.
4. J1 to J8 welding lines. The next is the vertical welding lines, which join the stiffeners to the girders. Here some patterns are observed, where the first beads are the FF beads of odd welding lines, i.e., the sequence is J1FF, J3FF, J5FF, and J7FF. This same pattern is applied for FA, AF and AA, respectively. For the even welds J2, J4, J6 and J8, the same pattern is applied. However, it starts with AF, followed by AA, FF and FA.
5. W3 and W6 welding lines. These are responsible for the joining of outer stiffeners to the base plate. Again, no logical pattern is followed, although the W3 is fully completed before W6 is started.

As mentioned before, these welds are not a common pattern practiced in industry. Thus, was decided to construct a second model, which should be a more realistic model. The second model will allow a comparison between this non-conventional welding pattern and a more common practice. Hence, some simplifications were made to develop the second model.

The first simplification is the merge of neighboring longitudinal beads. Presented in Figure 71, all the beads of the same side were merged together. This implied on a several decreases of the number of weld beads. Going from 20 weld beads on each welding line to only two beads.

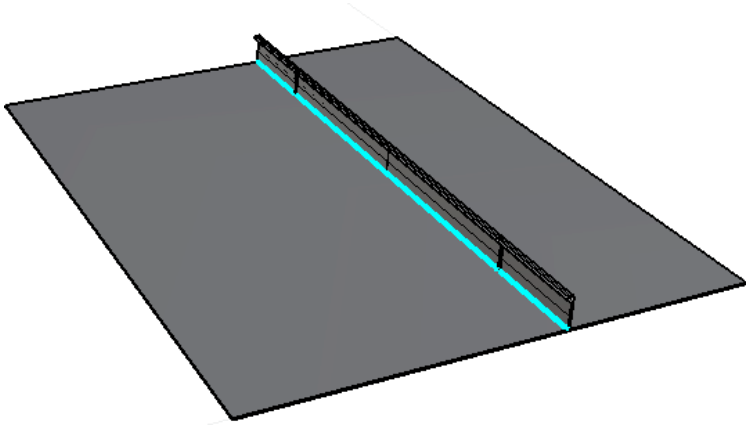

Figure 71 - Longitudinal weld beads merge

The same simplification was applied for W7 and W8 welding lines, the ones that join the flanges to the webs of the girders. In the original model, W7 had 10 beads in total and W8 had 12 beads. These were reduced to two beads on each welding line, which may be seen in the next figure:

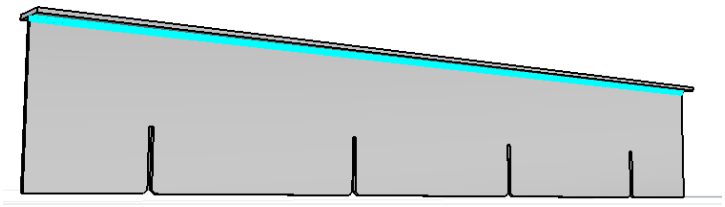

Figure 72 - W7 and W8 weld beads merge

The last simplification was made for W1 and W2 welding lines. However, in this case, it is not possible to merge all neighboring beads due to the already merged longitudinal beads. Thus, only the beads that lie between the stiffeners were merged, as depicted in Figure 73. In each welding line were present 16 beads, which were reduced to 10 after the mergence.

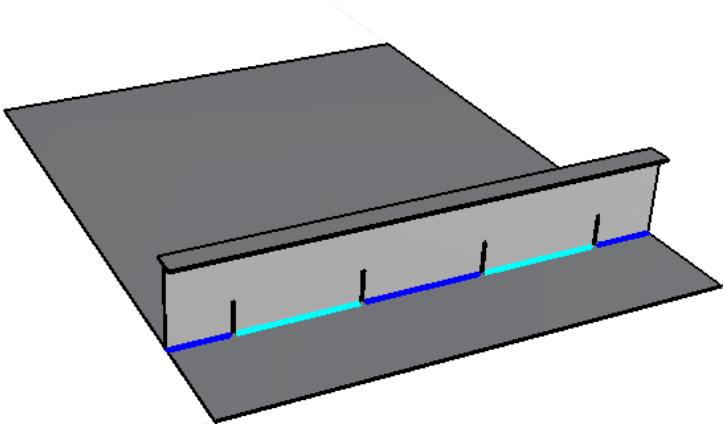

Figure 73 - W1 and W2 welding lines simplification

For this second model, the welding sequence was also determined to represent an industry practice. The first welding lines to be welded were W7 and W8, joining the flanges to the web girders. Starting the assembly by these welding lines may result in an easier welding procedure, as the girders may be welded in different positions than the original. The next parts to be welded are the longitudinal stiffeners, following the numerical sequence: W3, W4, W5 and W6. Ending the horizontal welding lines, the girder is assembled on the base plate by the welding lines W1 and W2. The last welds to be made are the verticals, where the entire group of four welds are sequentially made in each weld line J1 to J8. The exact welding sequence may be found in APPENDIX B.

From now on, the first model, which simulates the original experiment, will be called Original Welding Sequence Model. The second and simplified model will be called Common Welding Sequence Model. The adoption of a second model will enable the comparison of the optimized welding sequence. Revealing if a more complex structure is better or worse for the distortions over the base plate.

4.3.4. MESH SENSITIVITY ANALYSIS

In order to understand the behavior of the results according to the mesh refinement, a mesh sensitivity analysis was made. In this assessment were evaluated four different points on the base plate, which are represented in Figure 74.

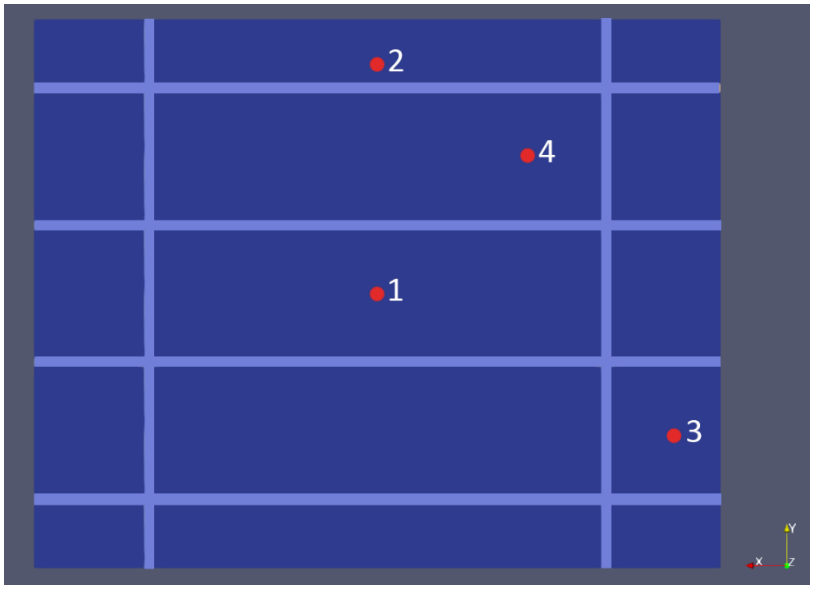

Figure 74 - Considered points to in mesh sensitivity analysis

The coordinates of these points are given by:

Point	x (mm)	y (mm)	z (mm)
1	750	600	0
2	750	1100	0
3	100	290	0
4	420	900	0

Table 7 - Coordinates of considered points

Two parameters were used to assess the meshes, the distortion magnitude and the distortion on z direction. The distortion magnitude is given by the square root of the sum of the squared distortion in each direction, as given next:

$$d = \sqrt{d_x^2 + d_y^2 + d_z^2}$$

The evaluated meshes were generated with no restrictions, i.e., the mesh all over the stiffened plate may assume similar elements sizes. It was not made any refinement near the welding areas, as the objective of the optimization is on the base plate. In this case, without constraints, the mesh generator algorithm in Virfac tries to use the maximum cell size as much as possible. Thus, the main parameter for mesh evaluation is the maximum cell size.

During the sensitivity analysis, the maximum cell size was minimized as possible. The minimum value that the computer was able to run the simulation was 2.5 mm. For values lower than this, the computer was not able to finish the simulation due to memory bottleneck. The next tables present the results obtained:

Run	Max Cell Size	Min Cell Size	Distortion Magnitude			
			Point 1	Point 2	Point 3	Point 4
5	0.0025	0.0005	1.267	2.744	3.339	2.352
2	0.003	0.0005	1.365	2.933	3.536	2.356
1	0.005	0.0005	1.176	3.245	2.670	2.878
3	0.008	0.0005	2.008	3.718	2.948	3.459
4	0.010	0.0005	2.447	4.182	2.005	3.523

Table 8 - Mesh analysis for distortion magnitude

Run	Max Cell Size	Min Cell Size	Distortion Z Direction			
			Point 1	Point 2	Point 3	Point 4
5	0.0025	0.0005	0.391	-2.615	3.131	-2.269
2	0.003	0.0005	0.101	-2.772	3.284	-2.248
1	0.005	0.0005	-0.463	-3.161	2.459	-2.825
3	0.008	0.0005	-1.324	-3.557	2.570	-3.371
4	0.010	0.0005	-2.233	-4.126	1.756	-3.487

Table 9 - Mesh analysis for distortion on z-direction

With these results in graphics presented in Figure 75 and Figure 76, it is possible to note that the points tends to behave equally. The tendency of increase or decrease is repeated by almost all points, the exception is point 3 that behaves differently. Although point 3 presents a strange variation in distortion magnitude, it is possible to see a more defined tendency of distortion on z direction.

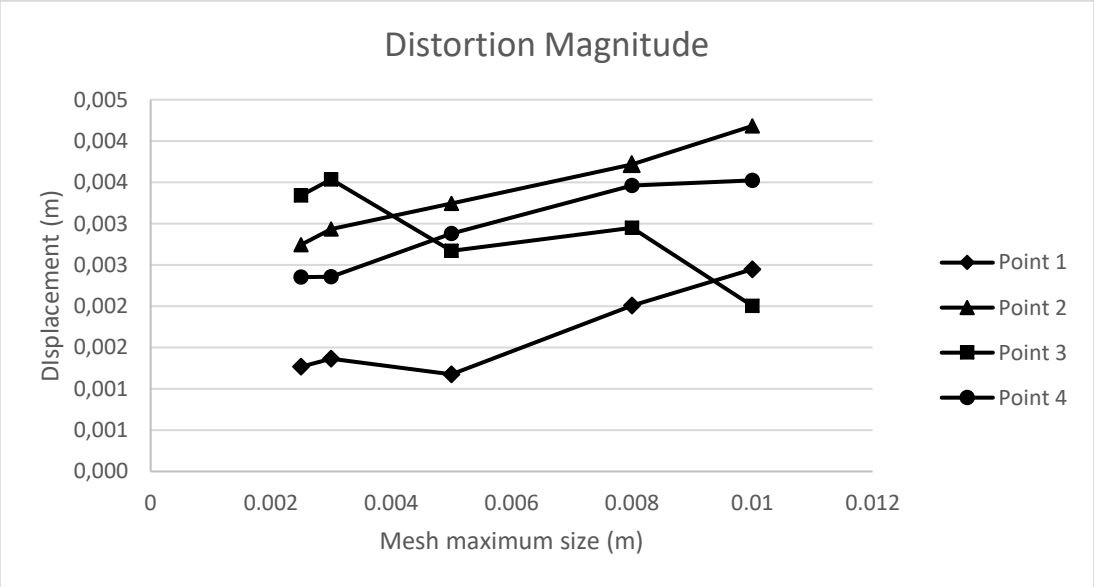

Figure 75 - Distortion magnitude generated according to mesh size

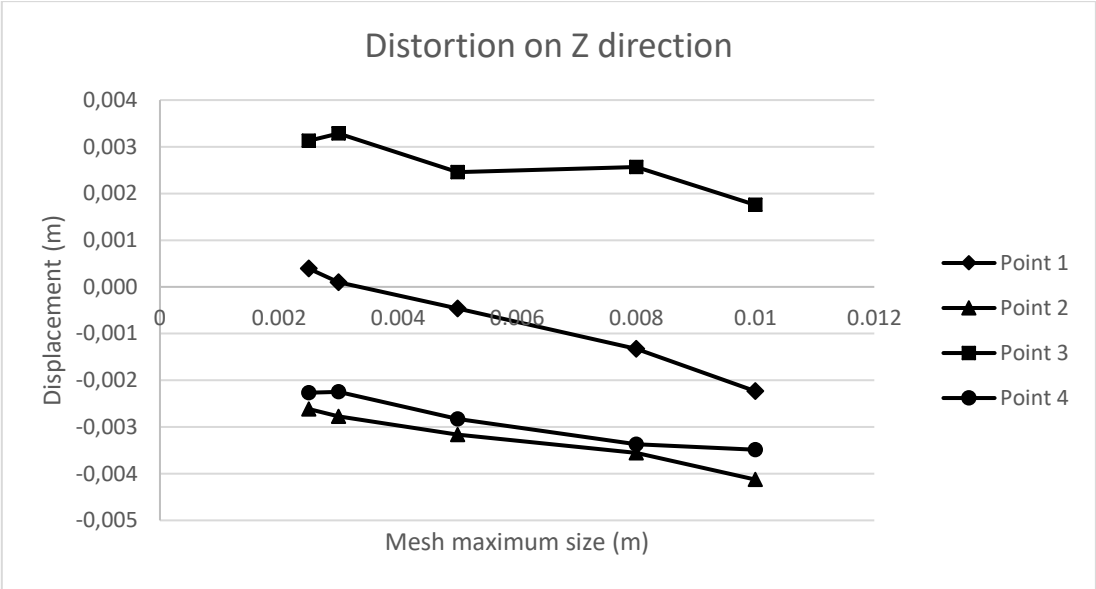

Figure 76 - Distortion magnitude generated according to mesh size

The great limiting of this project is the time consumed in each simulation. Any variation in the time spent to achieve results will generate a great variation on the optimization, due to the elevated number of iterations. In *Table 10* is possible to note the great difference that the cell size refinement generates. Reducing the cell size by 4, Run 4 to Run 5, the time is increased 26 times. This may turn the optimization unfeasible.

Run	Max Cell Size	Min Cell Size	Time
5	0.0025	0.0005	07:35
2	0.003	0.0005	04:18
1	0.005	0.0005	01:17
3	0.008	0.0005	00:30
4	0.010	0.0005	00:17

Table 10 - Time consumption according to the mesh refinement

The choice for the project was the coarser mesh, which has 10 mm for the cell maximum size and spends 17 minutes to run the simulation. As the points over the base plate tends to have a similar behavior and the focus of the project is to minimize distortions, was assumed that the same minimization will be achieved with the coarser mesh.

4.4. OPTIMIZATION

The objective for both models was the same, the minimization of distortions on the base plate. As mentioned before, the assessed distortion is given by its magnitude $\left(d = \sqrt{d_x^2 + d_y^2 + d_z^2}\right)$. Therefore, it is not possible to minimize only the vertical distortion. However, the main contributions for the magnitude are the vertical

displacements, as the resistance on longitudinal and transversal directions are considerable greater.

The main difference on optimization settings of the models is seen on the constraints. The Original Sequence Model (OSM) has no constraints, while the Common Sequence Model (CSM) was constrained by welding lines. The weld beads on W7 and W8 welding lines are the firsts to be joined. The order among beads of these welding lines is optimized, but they need to be completed before the next group. The second are the longitudinal welding lines W3 to W6. Again, these weld beads may be permutated among them, although may be completed before the next group starts to be welded. Next are the welding lines W1 and W2, which joins the girders to the base plate. Lastly, the vertical welds are performed. The mathematical formulation for the optimization problem of the Original Sequence Model (OSM) may be seen on equations 1 to 9:

$$\text{minimize } d(S) = \sqrt{[d_x(S)]^2 + \left[d_y(S)\right]^2 + [d_z(S)]^2} \tag{1}$$

Subject to:

$$\sum_{j=0}^{n+1} x_{ij} = 1 \quad \forall\, i = \{0,1,\dots,n,n+1\} \tag{2}$$

$$\sum_{i=0}^{n+1} x_{ij} = 1 \quad \forall\, j = \{0,1,\dots,n,n+1\} \tag{3}$$

$$\sum_{i\in K}\sum_{j\in K} x_{ij} \leq |K| - 1 \quad \forall i,j \tag{4}$$

$$x_{ij} = \{0,1\} \tag{5}$$

$$S = \{s_1, s_2, \dots, s_n\} \tag{6}$$

$$s_1 = j \mid x_{0j} = 1 \quad \forall\, j = \{1,2,\dots,n\} \tag{7}$$

$$s_p = j \mid x_{s_{p-1}j} = 1 \quad \forall\, j = \{1,2,\dots,n\}, p = \{2,3,\dots,n\} \tag{8}$$

$$x_{n+1;0} = 1 \tag{9}$$

Where:

$$x_{ij} \equiv path\ of\ the\ welding, going\ from\ the\ end\ of\ bead\ i\ to\ the\ start\ of\ bead\ j$$

$$n \equiv number\ of\ weld\ beads$$

$$K \equiv set\ of\ a\ possible\ sub-route$$

$$S \equiv welding\ sequence\ vector$$

Equation (1) is the objective function, which is dedicated to minimize the distortions for a given welding sequence S. Constraints start in (2), imposing one single end for each bead, while (3) imposes one single start for each bead. Equation (4) works against sub-routes. In (5) is stated the values that x_{ij} may assume, one if the path goes from the end of bead i to the start of bead j. The variable may assume zero if that path is not part of the sequence. The welding sequence vector is defined in (6) and the first entry of the vector is given in (7). The following entries of the vector are given by (8). The points 0 and n+1 are virtual nodes, used to impose the start on 0 and end on n+1. The last constraint (9) forces the sequence to be closed by going from the last virtual node to the first virtual node.

It is important to remember that the OSM has no constraints on the welding sequence. However, for the Common Sequence Model (CSM) were set rules, imposing that sequence starts on flange/web beads on girders, going to longitudinal stiffeners/base plate, next are girders/base plate beads and the last are the vertical beads joining longitudinal stiffeners to girders. For CSM the number of weld beads is 64 ($n = 64$). Therefore, the groups of beads may be given by:

$$\text{flange/web beads} = \{1, \dots, 4\}$$

$$\text{longitudinal stiffeners/base plate beads} = \{5, \dots, 12\}$$

$$\text{girders/base plate beads} = \{13, \dots, 32\}$$

$$\text{longitudinal stiffeners/girders beads} = \{33, \dots, 64\}$$

The mathematical formulation for the CSM is also given by equations 1 to 9, adding the constraints 10 to 13:

$$s_p = \{1, \dots, 4\} \quad \forall\, i = \{1, \dots, 4\} \tag{10}$$

$$s_p = \{5, \dots, 12\} \quad \forall\, i = \{5, \dots, 12\} \tag{11}$$

$$s_p = \{13, \dots, 32\} \quad \forall\, i = \{13, \dots, 32\} \tag{12}$$

$$s_p = \{33, \dots, 64\} \quad \forall\, i = \{33, \dots, 64\} \tag{13}$$

Constraint (10) imposes that flange/web beads are the first set to be made. The next set of beads are longitudinal stiffeners/base plate beads (11), followed by girders/base plate beads (12). The last set to be welded are longitudinal stiffeners/girders beads, given in (13).

Genetic algorithms are based on random procedures, which may generate different results for runs with the same settings. Therefore, the indicated stop criterion is the number of iterations. If a reduction in distortion is adopted, the time spent in a run may vary greatly. In this project were adopted two runs for each model, one with 100 iterations and another with 200 iterations.

5. RESULTS AND DISCUSSION

As expected, the models consumed several hours to achieve the determined number of iterations. They were run by an Intel Core i7-4770 3.40GHz with 16GB of RAM memory. The Original Sequence Model (OSM) spent 22 hours to complete 100 iterations and almost 47 hours to complete 200 iterations. For the Common Sequence Model (CSM), less time was spent in optimization, as the number of beads is lower when compared to the OSM. Hence, were necessary 8 hours to achieve 100 iterations and almost 16 hours to achieve 200 iterations. The initial and optimized welding sequences are available on APPENDIX B.

These time spans may be improved using a cluster or a more powerful computer, which is not an expensive acquisition for industry segments. However, even the obtained time terms are practicable for the industry. If considered that the optimizations are run along the detailed project and even during the constructions phase, the practiced terms are truly practicable.

Follows in Figure 77 the optimization of Original Sequence Model with 100 iterations. The model starts with 10.7 mm of average distortion on the first iteration, is minimized to 6.4 mm on the 98th iteration. This represents a decrease of 40.2% in the total distortion over the base plate, which is a considerable reduction that may facilitate the assembling of panels and blocks.

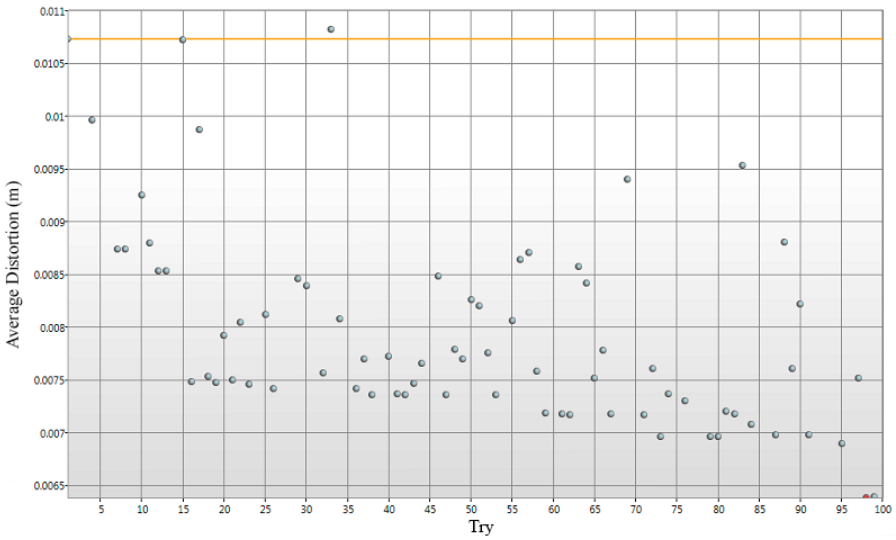

Figure 77 - Optimization of Original Sequence Model for 100 iterations

Next is presented the optimization of OSM with 200 iterations in Figure 78. Again, the model starts with 10.7 mm of average distortion over the base plate. However, the doubled

number of iterations was not capable to achieve a better result. Instead, the optimization reached only 6.8 mm of distortion on 194th try, which represents a decrease of 36.5%.

This unexpected result may be a side effect of the chosen optimization method. One probable explanation is the seed used on each optimization, which maybe different and led to a local minimum. Another explanation for this behavior is the Xtreme technology [59]. The neural network present in the optimization method may not work properly, mistakenly modeling the problem. As the optimization code is not open, the assessment of this problem is not effectively possible.

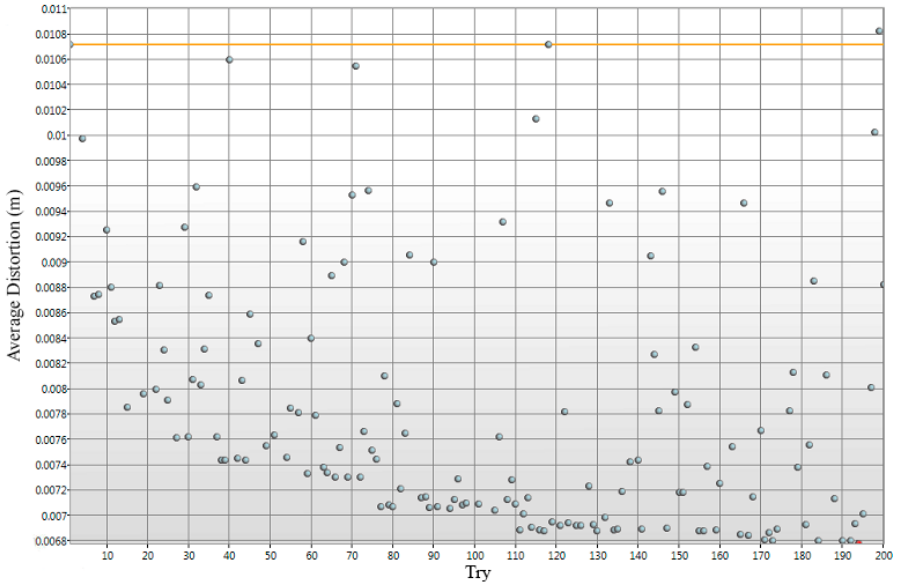

Figure 78 - Optimization of Original Sequence Model for 200 iterations

Now changing to the second model, the Common Sequence Model (CSM), is presented in Figure 79 the results for 100 iterations optimization. The model starts with 11.7 mm of average distortion, reaching 10.3 mm in 85th iteration. This is a 12.0% reduction is distortion over the base plate. If compared to the decrease obtained on the OSM, this optimization was not too efficient.

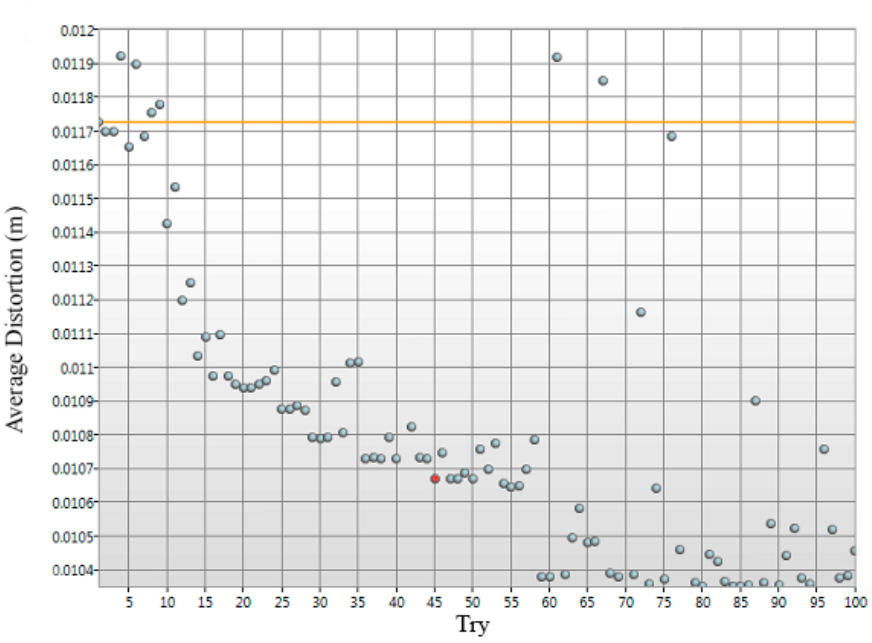

Figure 79 - Optimization of Common Sequence Model for 100 iterations

The last is the 200 iterations optimization for the CSM. It results in a decrease to 7.1 mm of average distortion on 199th iteration, presented in Figure 80. This represents 39.3% of reduction, approaching to the results obtained for the OSM. Remembering that CSM has simplifications and constraints that approximate it to real practice, this reduction may be interesting to industry. This must facilitate the assembly of panels and blocks.

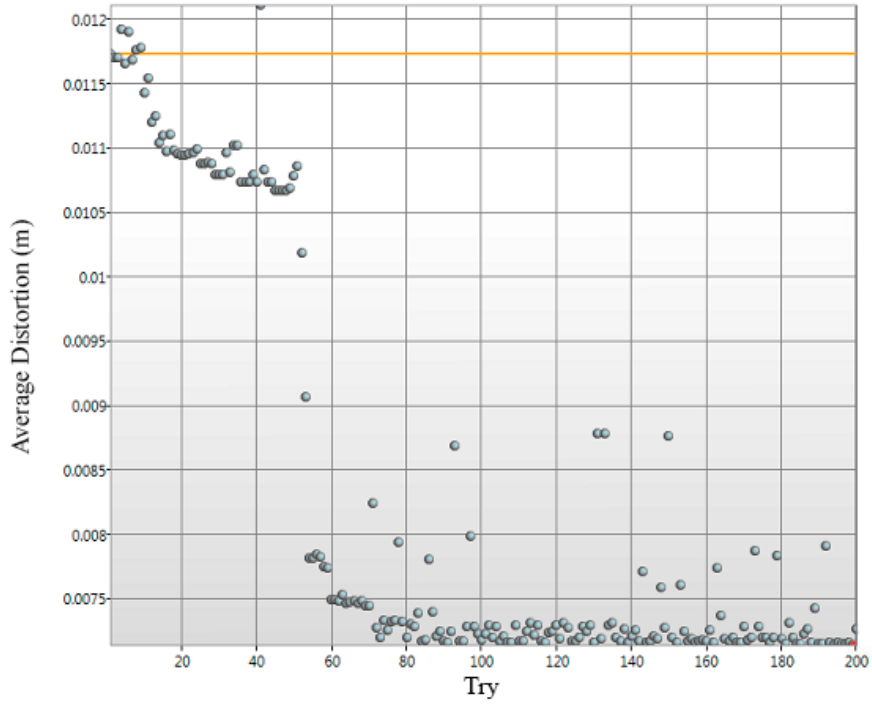

Figure 80 - Optimization of Common Sequence Model for 200 iterations

Summarizing the obtained results, it is presented in *Table 11*, which shows the distortion and relative decrease for each optimization.

	Original Sequence		Common Sequence	
	Distortion (mm)	Decrease (%)	Distortion (mm)	Decrease (%)
Initial	10.7	-	11.7	-
100 Optimization	6.4	40.2	10.3	12.0
200 Optimization	6.8	36.5	7.1	39.3

Table 11 - Summary of the obtained results for optimizations

Figure 81 shows the displacement on the vertical direction for the base plate. It is possible to note that the initial sequence has a great negative displacement on the edges. The results of optimizations transform the main part of distortion into a positive displacement. It is even possible to see that the plate with 6.4 mm distortion has more white areas, which denotes a distortion near to zero.

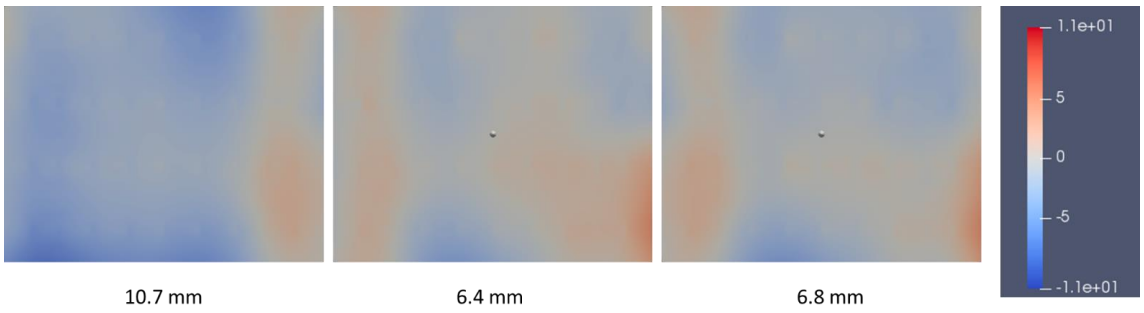

Figure 81 - Comparison between base plate distortion for initial sequence, 100 optimization and 200 optimization of Original Sequence Model

The same illustration is presented for the Common Sequence Model in Figure 82. The starting welding sequence generates a different profile when compared to the OSM, as the main displacement is now in a positive direction. Being maximum on the areas near to the girders. The optimizations show the whitening of displaced areas, diminishing the overall distortion.

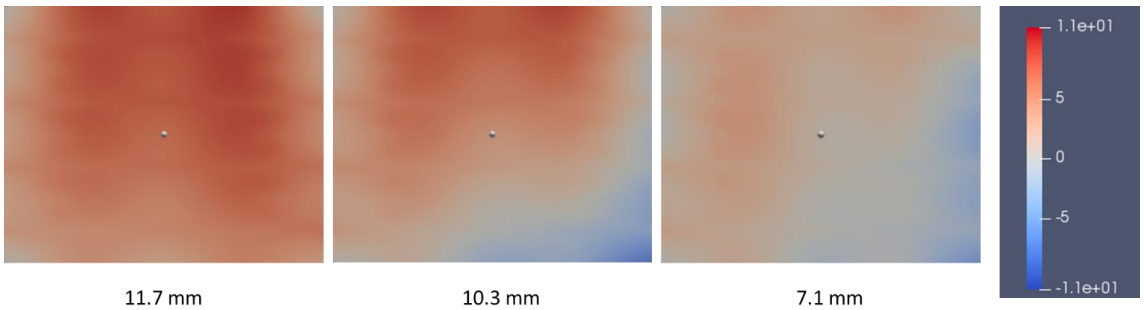

Figure 82 - Comparison between base plate distortion for the initial sequence, 100 optimizations and 200 optimizations of Common Sequence Model

The visual comparison is not an accurate method, becoming important to present the results data on another format. Figure 83 shows the normalized frequency of distortions on vertical direction over the base plate for each welding sequence: initial, 100 optimization and 200 optimization. It is also shown the mean value and the standard deviation for each welding sequence.

As the results described earlier, it is evident in data analysis that the 100 iterations optimization achieved the minimum distortion. The mean value most close to zero is given by the 100 iterations optimization, indicating that distortions are better distributed along the negative and positive displacement axis. Additionally, the 100 optimization has the lower standard deviation, indicating that frequencies are closer to the mean than the other welding sequences. The combination of near to zero mean distortion and lower standard deviation confirms that try 98 is the best result achieved during the optimization.

The same representation is made for Common Sequence Model in Figure 84. May be seen on chart and by the mean value of distortion, that try 199 from 200 optimization has the mean most close from zero. This welding sequence also presents the lower standard deviation, indicating a higher concentration of distortions around the mean value.

As discussed before, try 98 from OSM and try 199 from CSM are the better welding sequences found during the optimization process. This is concluded from the data generated by Virfac, which is the comparison between distortion magnitude, and from analysis of vertical displacement, given by visual comparison and frequencies distribution.

The last results to be presented are the comparison between the two models, depicted in Figure 85. The results given by Virfac show that optimized welding sequences have a near distortion, 6.4 for OSM on 98^{th} try and 7.1 for CSM on 199^{th} try. However, Figure 85 shows that mean frequency of distortions is much closer to zero on OSM than CSM. Although CSM presents a lower standard deviation, the difference between the OSM standard deviation is not great. OSM mean represents only 16.3% of the CSM mean, while CSM standard deviation is 93.9% of OSM's. This comparison shows that the difference on standard deviation is negligible when considered the difference between mean distortion frequency. Therefore, the results given by Virfac are reinforced, even though the vertical displacement is only one part of the results presented by Virfac.

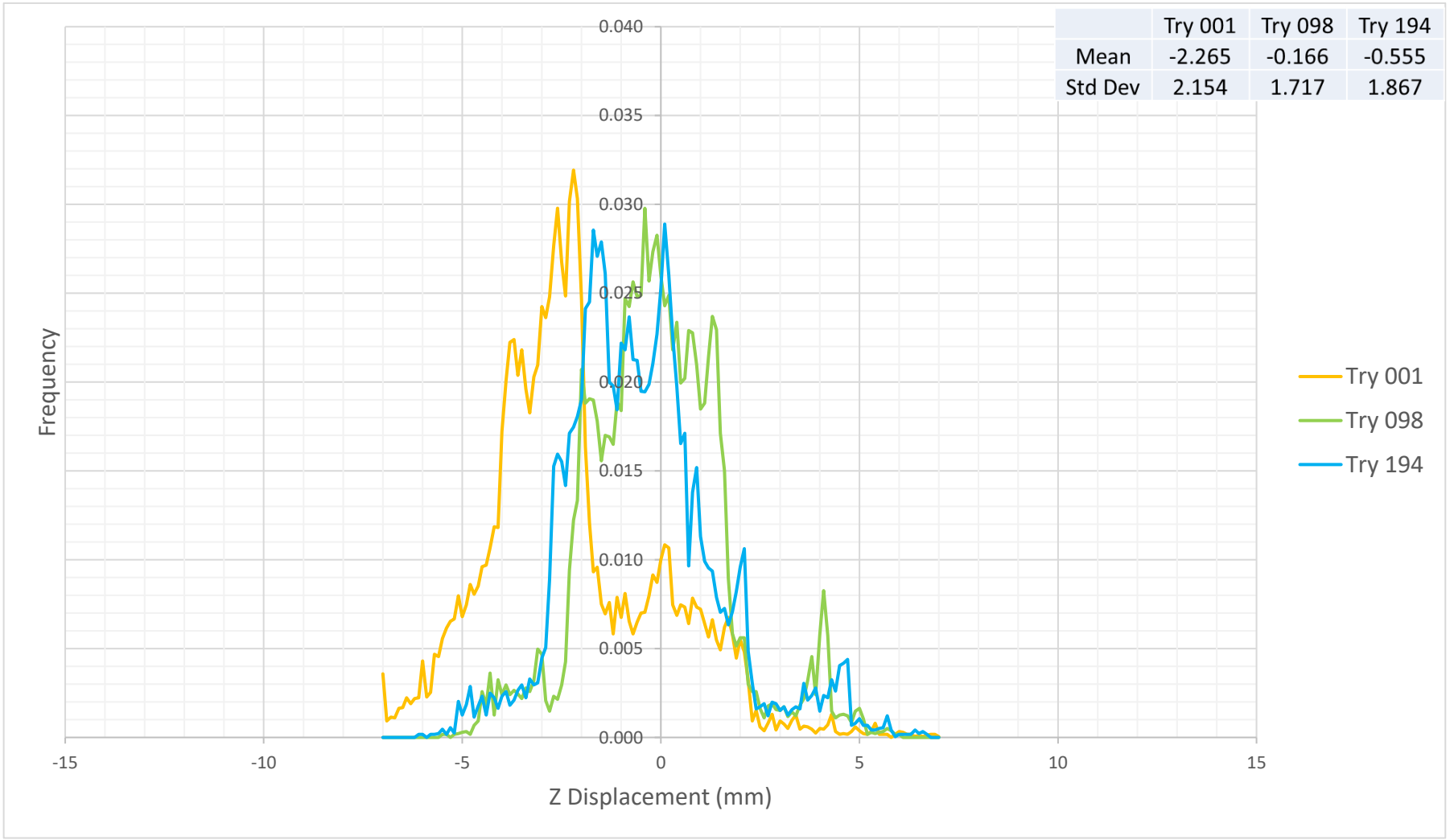

Figure 83 - Normalized frequency of distortions over the base plate for Original Sequence Model

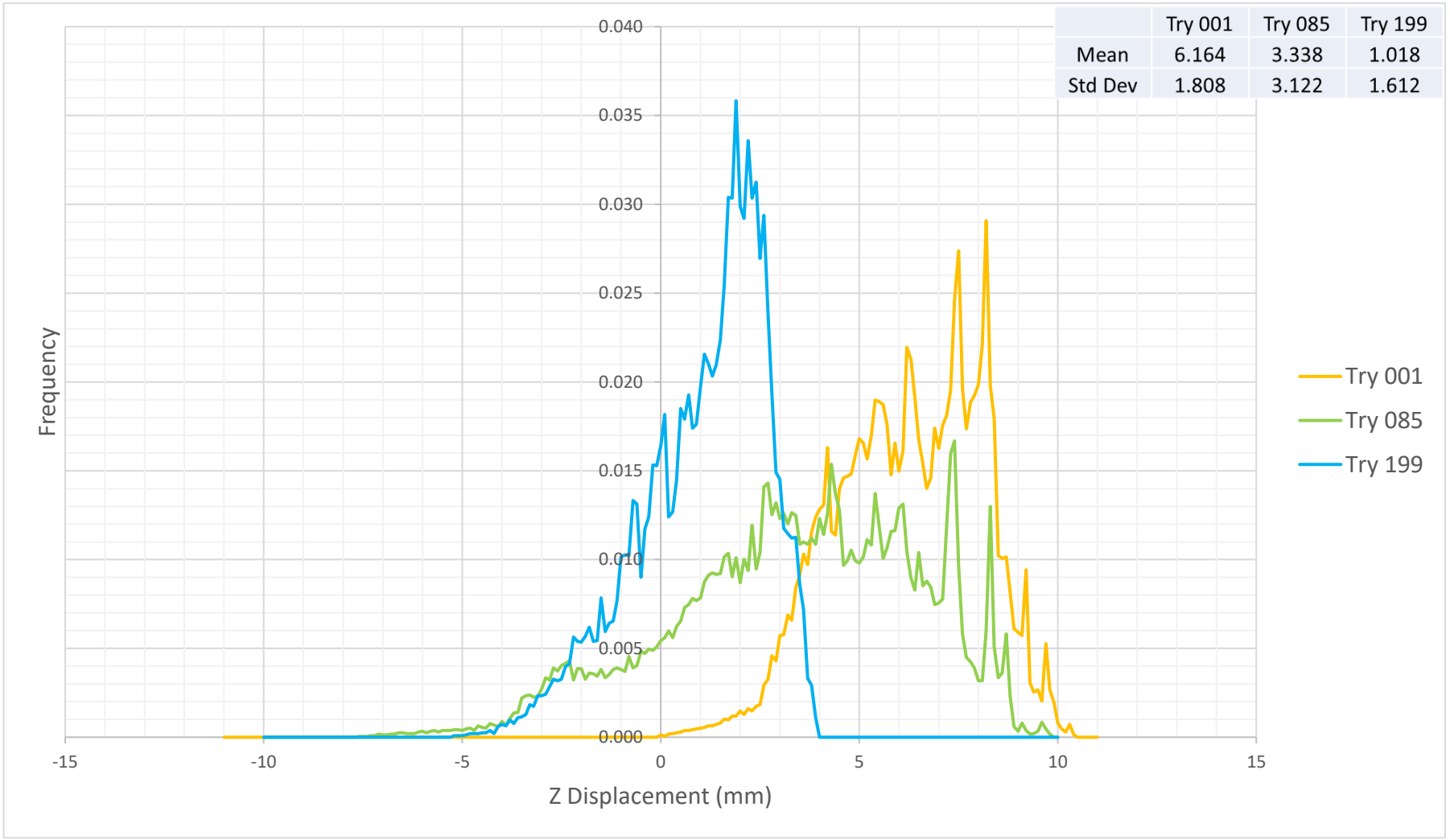

Figure 84 - Normalized frequency of distortions over the base plate for Common Sequence Model

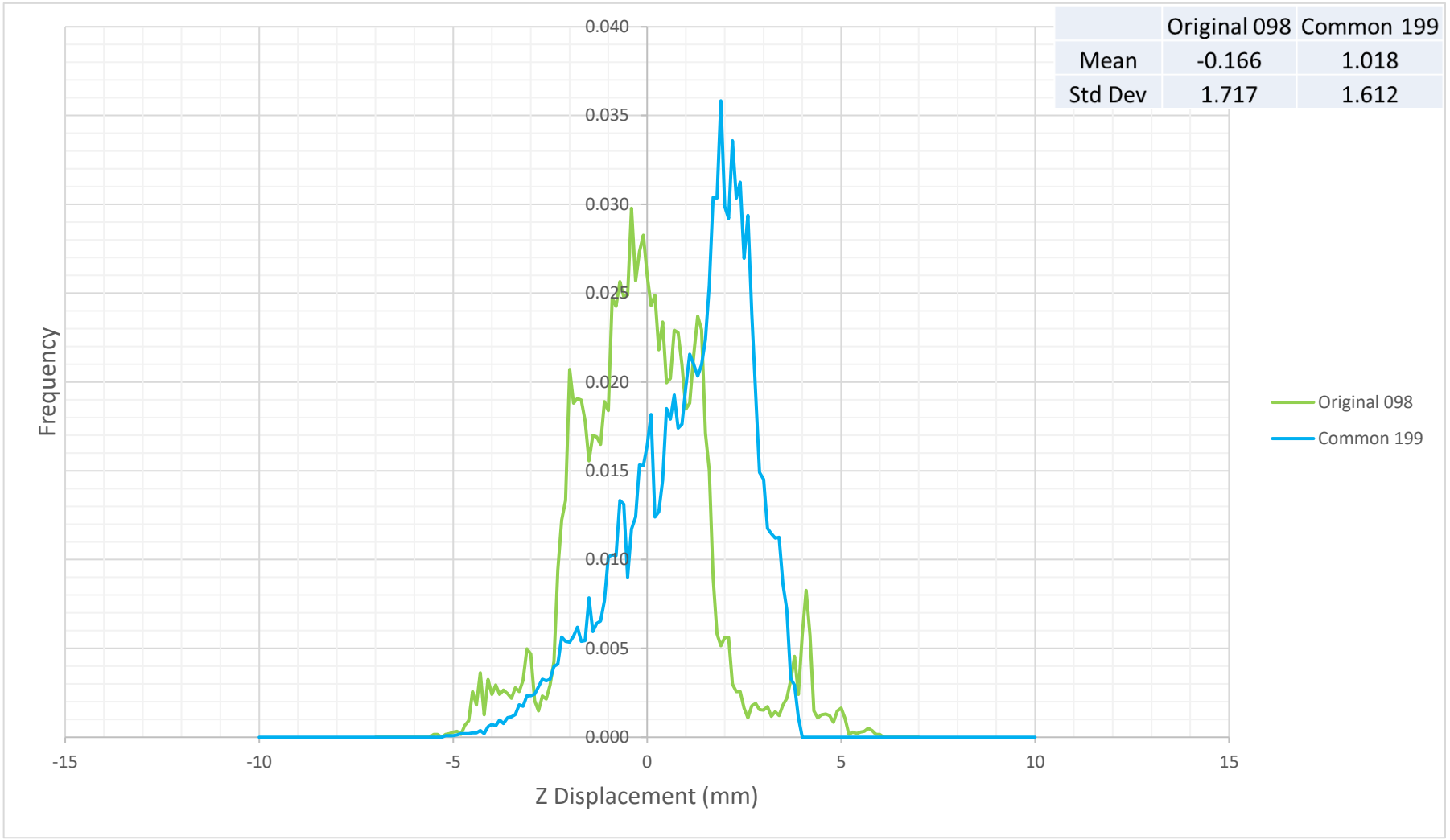

Figure 85 - Comparison between optimized welding sequences of OSM and CSM

Other parameters that may be assessed are the shrinkage on the in-plane direction, the longitudinal and the transversal shrinkage. These values are calculated as the difference in mm between the edges of the base plate. For the longitudinal shrinkage, are considered the transversal lines on $x = 0\,mm$ and $x = 1500\,mm$. The same is done for the transversal shrinkage, but with longitudinal lines on the edges, the first at $y = 0\,mm$ and the second at $x = 1200\,mm$.

The results of longitudinal and transversal shrinkage are presented in Figure 86 and Figure 87. Are presented the shrinkage for the original welding sequence for both models, Original Sequence Model (OSM) and Common Sequence Model (CSM). Also, are shown the shrinkages for the optimized sequence of each model. The positive values correspond to shrinkage and the negative to stretch.

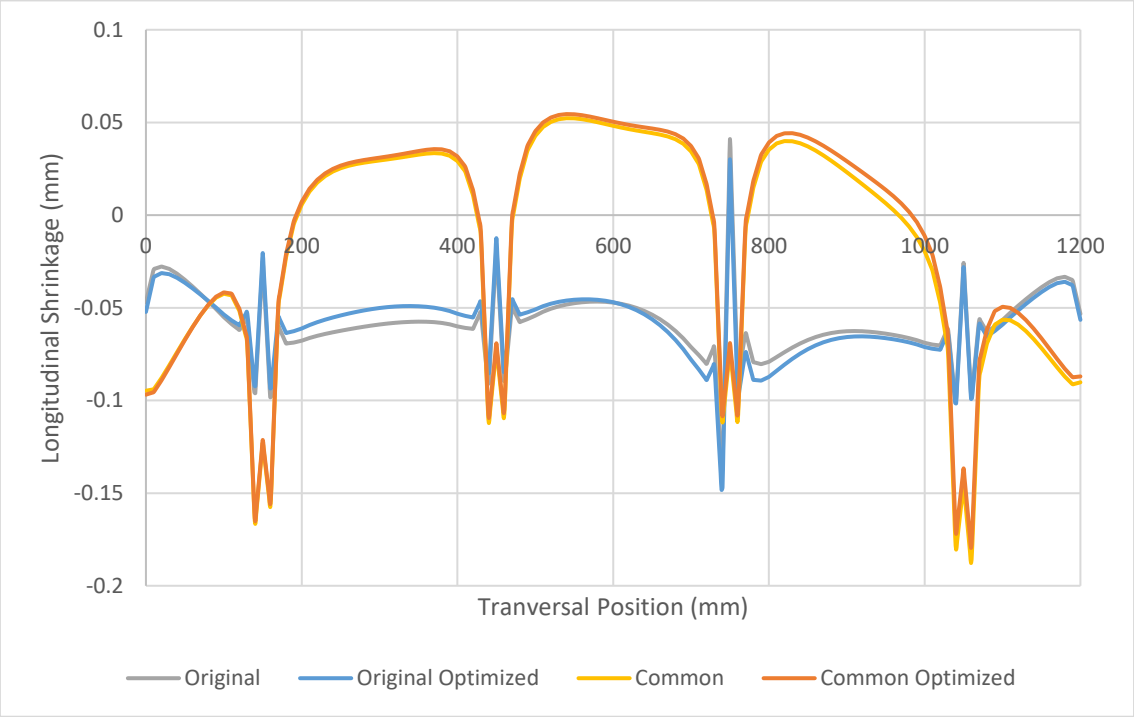

Figure 86 - Longitudinal shrinkage of the global models

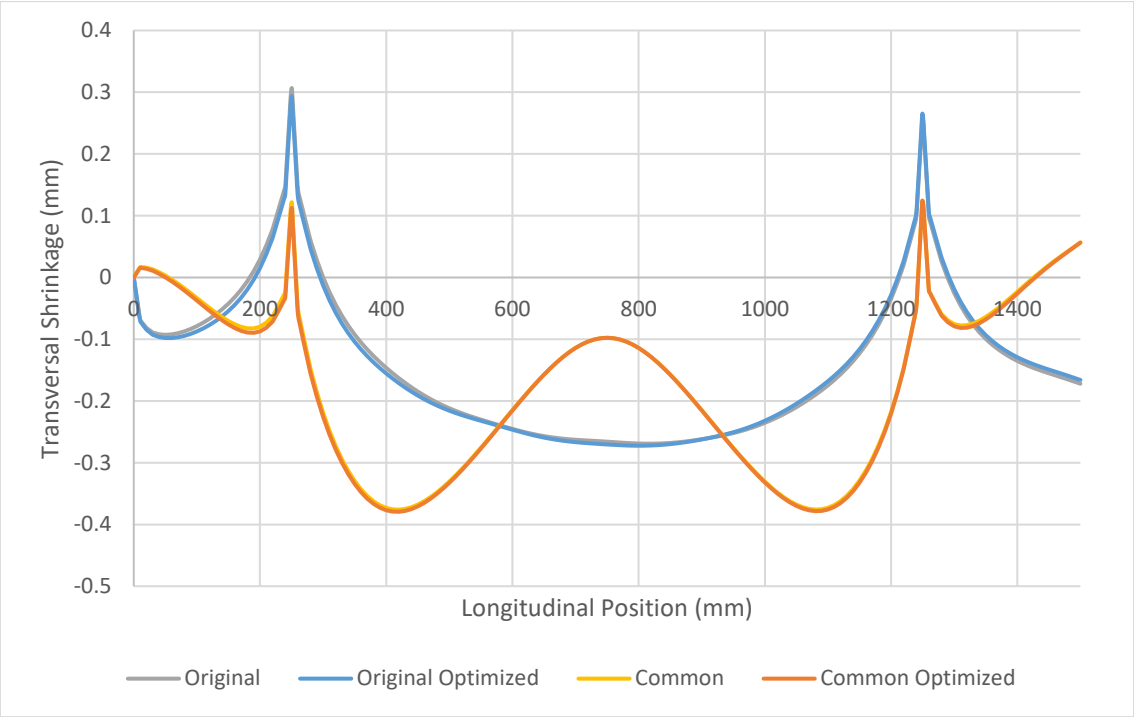

Figure 87 - Transversal shrinkage of the global models

6. CONCLUSIONS

On this project, a method was developed to minimize the distortions over a stiffened plate. The first phase was responsible to create and simulate local models, which results were used to compose and predict the distortions over the stiffened plate, called global model. Next, an optimization was implemented on the welding sequence in order to minimize the distortions over the base plate.

The method was able to minimize the distortions on the base plate, reaching a decrease of 40.2% for the model based on the original welding sequence (Original Sequence Model) and 39.3% for the simplified model (Common Sequence Model). Although the obtained welding sequence is not a usual one, it may improve the assembling of panels and blocks in shipyards. Leading to a reduction in time spent in this phase, which tends to reduce the costs.

Another important feature of the proposed method is its feasibility into an industrial environment. The time spent on the optimizations are viable to be implemented through the detailed project phase and could be extended over the construction phase if necessary. Furthermore, the computer necessary to run the optimization does not have an elevated cost. If a cluster is combined with the proposed method, which has a higher cost when compared to the user computer, a great gain in time spent is expected.

Becomes a difficult task for a welder to implement a random welding sequence, as the ones generated by the optimizations. However, robots are becoming more usual in industry, which enables the adoption of complicated welding sequences. Also a multi-objective optimization may be studied adding the travel distance of the robot as a part of the objective function.

The results also shown a side effect of the optimizations, which is local minimum. Maybe the code was led into a local minimum, as occurred on the 200 iterations optimization for the Original Sequence Model. As the results are worst when compared to the 100 iterations optimization, which is the opposite of the expectation.

The great difference observed on vertical displacements, was not present on in-plane shrinkage when comparing the original and optimized models. However, a severe change on the pattern was observed between models. The main modification was observed on the

longitudinal shrinkage, where the simplification of the model led to shrinkage instead of stretch, as presented by the original model.

Comparing the optimized results of both models, it was seen a considerable difference on distortion distribution. The Original Sequence Model (OSM) presented fewer vertical distortions when compared to the optimized Common Sequence Model (CSM). Thus, would be an interesting study to also analyse the ideal number of weld beads that is necessary to optimize the distortions. As the current study presents a great difference on the number of beads for longitudinal stiffeners. OSM presents 20 beads for each stiffener, while CSM presents only two.

Another important and crucial enhance for this work is the validation of simulations. Although the use of computational simulations is getting more reliable, the validation is one essential step. On this project was expected to compare the obtained results with the original experiment. First, we expected to receive the experimental data from GeonX after the results of the simulations. However, these data were not passed for us. Now we are in direct contact with DAMEN, trying to get the experimental results. The costs to perform an experiment were elevated, making it unpractic for the laboratory. Maybe in the future, this project may be offered to a partnership turning the experiment feasible.

REFERENCES

[1] Chen BQ, Guedes Soares C. Effects of plate configurations on the weld induced deformations and strength of fillet-welded plates. Mar Struct 2016;50:243–59. doi:10.1016/j.marstruc.2016.09.004.

[2] Farajkhah V, Liu Y. Effect of metal inert gas welding on the behaviour and strength of aluminum stiffened plates. Mar Struct 2016;50:95–110. doi:10.1016/J.MARSTRUC.2016.07.005.

[3] Gannon L, Liu Y, Pegg N, Smith MJ. Effect of welding-induced residual stress and distortion on ship hull girder ultimate strength. Mar Struct 2012;28:25–49. doi:https://doi.org/10.1016/j.marstruc.2012.03.004.

[4] Shi XH, Zhang J, Guedes Soares C. Experimental study on collapse of cracked stiffened plate with initial imperfections under compression. Thin-Walled Struct 2017;114:39–51. doi:10.1016/J.TWS.2016.12.028.

[5] Deng D. Influence of deposition sequence on welding residual stress and deformation in an austenitic stainless steel J-groove welded joint. Mater Des 2013;49:1022–33. doi:10.1016/J.MATDES.2013.02.065.

[6] Fu G, Lourenço MI, Duan M, Estefen SF. Influence of the welding sequence on residual stress and distortion of fillet welded structures. Mar Struct 2016;46:30–55. doi:10.1016/j.marstruc.2015.12.001.

[7] Gannon L, Liu Y, Pegg N, Smith M. Effect of welding sequence on residual stress and distortion in flat-bar stiffened plates. Mar Struct 2010;23:385–404. doi:10.1016/J.MARSTRUC.2010.05.002.

[8] Doyen O, Rizzo N, Forest L, Tosi J, Thomas N, Zmitko M. Assessment of HCLL-TBM optimum welding sequence scenario to minimize welding distortions. Fusion Eng Des 2017;121:80–6. doi:10.1016/j.fusengdes.2017.06.015.

[9] Chen Z, Chen Z, Shenoi RA. Influence of welding sequence on welding deformation and residual stress of a stiffened plate structure. Ocean Eng 2015;106:271–80. doi:10.1016/j.oceaneng.2015.07.013.

[10] Ozcatalbas Y, Vural HI. Determination of optimum welding sequence and distortion forces in steel lattice beams. J Mater Process Technol 2009;209:599–

604. doi:10.1016/J.JMATPROTEC.2008.02.051.

[11] Michaleris P, DeBiccari A. Prediction of welding distortion. Weld J 1997;76:172–80.

[12] Souloumiac B, Boitout F, Bergheau J-M. A new local global approach for the modelling of welded steel component distortions. Math Model Weld Phenom 2002;6:573–90.

[13] Derakhshan ED, Yazdian N, Craft B, Smith S, Kovacevic R. Numerical simulation and experimental validation of residual stress and welding distortion induced by laser-based welding processes of thin structural steel plates in butt joint configuration. Opt Laser Technol 2018;104:170–82. doi:10.1016/j.optlastec.2018.02.026.

[14] Pasternak H, Launert B, Kannengießer T, Rhode M. Advanced Residual Stress Assessment of Plate Girders Through Welding Simulation. Procedia Eng 2017;172:23–30. doi:10.1016/j.proeng.2017.02.013.

[15] Xia J, Jin H. Analysis of residual stresses and variation mechanism in dissimilar girth welded joints between tubular structures and steel castings. Int J Press Vessel Pip 2018;165:104–13. doi:10.1016/j.ijpvp.2018.06.003.

[16] Gadallah R, Osawa N, Tanaka S, Tsutsumi S. A novel approach to evaluate mixed-mode SIFs for a through-thickness crack in a welding residual stress field using an effective welding simulation method. Eng Fract Mech 2018;197:48–65. doi:10.1016/j.engfracmech.2018.04.040.

[17] Ihara R, Katsuyama J, Onizawa K, Hashimoto T, Mikami Y, Mochizuki M. Prediction of residual stress distributions due to surface machining and welding and crack growth simulation under residual stress distribution. Nucl Eng Des 2011;241:1335–44. doi:10.1016/j.nucengdes.2011.01.018.

[18] Cho WI, Schultz V, Woizeschke P. Numerical study of the effect of the oscillation frequency in buttonhole welding. J Mater Process Technol 2018;261:202–12. doi:10.1016/j.jmatprotec.2018.05.024.

[19] Ai Y, Jiang P, Wang C, Mi G, Geng S. Experimental and numerical analysis of molten pool and keyhole profile during high-power deep-penetration laser

welding. Int J Heat Mass Transf 2018;126:779–89. doi:10.1016/j.ijheatmasstransfer.2018.05.031.

[20] Yang Z, Zhao X, Tao W, Jin C. Effects of keyhole status on melt flow and flow-induced porosity formation during double-sided laser welding of AA6056/AA6156 aluminium alloy T-joint. Opt Laser Technol 2019;109:39–48. doi:10.1016/j.optlastec.2018.07.065.

[21] Baptista R, Santos T, Marques J, Guedes M, Infante V. Fatigue behavior and microstructural characterization of a high strength steel for welded railway rails. Int J Fatigue 2018;117:1–8. doi:10.1016/j.ijfatigue.2018.07.032.

[22] Zhu C, Cheon J, Tang X, Na SJ, Cui H. Molten pool behaviors and their influences on welding defects in narrow gap GMAW of 5083 Al-alloy. Int J Heat Mass Transf 2018;126:1206–21. doi:10.1016/j.ijheatmasstransfer.2018.05.132.

[23] Fu G, Lourenco MI, Duan M, Estefen SF. Effect of boundary conditions on residual stress and distortion in T-joint welds. J Constr Steel Res 2014;102:121–35. doi:10.1016/j.jcsr.2014.07.008.

[24] Caprace JD, Fu G, Carrara JF, Remes H, Shin SB. A benchmark study of uncertainness in welding simulation. Mar Struct 2017;56:69–84. doi:10.1016/j.marstruc.2017.07.005.

[25] Goldak JA, Akhlaghi M. Computational Welding Mechanics. New York: Springer US; 2005.

[26] Rosenthal D. The theory of moving sources of heat and its application to metal treatments. Trans ASME 1946;68:849–65.

[27] Rykalin R. Energy sources for welding. Weld World 1974;12:227–48.

[28] Pavelic V, Tanbakuchi R, Uyehara OA, Myers PS. Experimental and computed temperature histories in gas tungsten arc welding of thin plates. Weld J Res Suppl 1969;48:295s–305s.

[29] Goldak JA, Chakravarti A, Bibby M. A new finite element model for welding heat sources. Metall Trans B 1984;15B:299–305.

[30] Xiu L, Wu J, Liu Z, Ma J, Fan X, Ji H, et al. Weld distortion prediction of the

CFETR vacuum vessel by inherent strain theory. Fusion Eng Des 2017;121:43–9. doi:10.1016/j.fusengdes.2017.03.175.

[31] Guirao J, Rodríguez E, Bayón A, Cortizo JL, Jones L. A study of the influence of electron beam welding sequences on the ITER vacuum vessel prototype VATS. Fusion Eng Des 2011;86:2805–11. doi:10.1016/j.fusengdes.2011.04.015.

[32] Shadkam S, Ranjbarnodeh E, Iranmanesh M. Effect of sequence and stiffener shape on welding distortion of stiffened panel. J Constr Steel Res 2018;149:41–52. doi:10.1016/j.jcsr.2018.07.010.

[33] Wang J, Zhao H, Zou J, Zhou H, Wu Z, Du S. Welding distortion prediction with elastic FE analysis and mitigation practice in fabrication of cantilever beam component of jack-up drilling rig. Ocean Eng 2017;130:25–39. doi:10.1016/j.oceaneng.2016.11.059.

[34] Tekgoz M, Garbatov Y, Soares CG. Ultimate strength assessment of welded stiffened plates. Eng Struct 2015;84:325–39. doi:https://doi.org/10.1016/j.engstruct.2014.12.001.

[35] Bai R, Guo Z, Tian C, Lei Z, Yan C, Tao W. Investigation on welding sequence of I-beam by hybrid inversion. Mar Struct 2018;62:23–39. doi:10.1016/j.marstruc.2018.07.002.

[36] Shao Q, Xu T, Yoshino T, Song N. Multi-objective optimization of gas metal arc welding parameters and sequences for low-carbon steel (Q345D) T-joints. J Iron Steel Res Int 2017;24:544–55. doi:10.1016/S1006-706X(17)30082-1.

[37] Bonnaud E. Mitigation of weld residual deformations by weld sequence optimization: limitations and enhancements of surrogate models. Procedia Struct Integr 2017;5:310–7. doi:10.1016/j.prostr.2017.07.176.

[38] Li Y, Wang K, Jin Y, Xu M, Lu H. Prediction of welding deformation in stiffened structure by introducing thermo-mechanical interface element. J Mater Process Technol 2015;216:440–6. doi:10.1016/j.jmatprotec.2014.10.012.

[39] Tian Y, Wang C, Zhu D, Zhou Y. Finite element modeling of electron beam welding of a large complex Al alloy structure by parallel computations. J Mater Process Technol 2008;199:41–8. doi:10.1016/j.jmatprotec.2007.07.045.

[40] Ma N, Yuan S. An Accelerated Explicit Method and GPU Parallel Computing for Thermal Stress and Welding Deformation of Automotive Parts. Int J Appl Mech 2016;08:1650023. doi:10.1142/S175882511650023X.

[41] Ikushima K, Itoh S, Shibahara M. Development of idealized explicit FEM using GPU parallelization and its application to large-scale analysis of residual stress of multi-pass welded pipe joint. Weld World 2015;59:589–95. doi:10.1007/s40194-015-0235-2.

[42] Ikushima K, Shibahara M. Prediction of residual stresses in multi-pass welded joint using Idealized Explicit FEM accelerated by a GPU. Comput Mater Sci 2014;93:62–7. doi:10.1016/j.commatsci.2014.06.024.

[43] Maekawa A, Kawahara A, Serizawa H, Murakawa H. Fast three-dimensional multipass welding simulation using an iterative substructure method. J Mater Process Technol 2015;215:30–41. doi:10.1016/j.jmatprotec.2014.08.004.

[44] Bhatti AA, Barsoum Z, Khurshid M. Development of a finite element simulation framework for the prediction of residual stresses in large welded structures. Comput Struct 2013;133:1–11. doi:10.1016/j.compstruc.2013.11.011.

[45] Huang H, Tsutsumi S, Wang J, Li L, Murakawa H. High performance computation of residual stress and distortion in laser welded 301L stainless sheets. Finite Elem Anal Des 2017;135:1–10. doi:10.1016/j.finel.2017.07.004.

[46] Rong Y, Zhang G, Huang Y. Study on deformation and residual stress of laser welding 316L T-joint using 3D/shell finite element analysis and experiment verification. Int J Adv Manuf Technol 2017;89:2077–85. doi:10.1007/s00170-016-9246-4.

[47] Wang J, Yuan H, Ma N, Murakawa H. Recent research on welding distortion prediction in thin plate fabrication by means of elastic FE computation. Mar Struct 2016;47:42–59. doi:10.1016/j.marstruc.2016.02.004.

[48] Deng D, Murakawa H, Shibahara M. Investigations on welding distortion in an asymmetrical curved block by means of numerical simulation technology and experimental method. Comput Mater Sci 2010;48:187–94. doi:10.1016/j.commatsci.2009.12.027.

[49] Deng D, Murakawa H. FEM prediction of buckling distortion induced by welding in thin plate panel structures. Comput Mater Sci 2008;43:591–607. doi:10.1016/j.commatsci.2008.01.003.

[50] Murakawa H, Deng D, Ma N, Wang J. Applications of inherent strain and interface element to simulation of welding deformation in thin plate structures. Comput Mater Sci 2012;51:43–52. doi:10.1016/j.commatsci.2011.06.040.

[51] Liang W, Deng D. Influences of heat input, welding sequence and external restraint on twisting distortion in an asymmetrical curved stiffened panel. Adv Eng Softw 2018;115:439–51. doi:10.1016/j.advengsoft.2017.11.002.

[52] Ueda Y, Fukuda K, Nakacho K, Endo S. A New Measuring Method of Residual Stresses with the Aid of Finite Element Method and Reliability of Estimated Values. J Soc Nav Archit Japan 1975;1975:499–507.

[53] Yalamanchili VK, Galindo DA, Mach JC. Robust Virtual Welding Process Optimization. Procedia Comput Sci 2018;140:342–50. doi:10.1016/j.procs.2018.10.305.

[54] Choudhary A, Kumar M, Unune DR. Experimental investigation and optimization of weld bead characteristics during submerged arc welding of AISI 1023 steel. Def Technol 2018. doi:10.1016/j.dt.2018.08.004.

[55] Edwin RDJ, Jenkins HDS. A review on optimization of welding process. Procedia Eng 2012;38:544–54. doi:10.1016/j.proeng.2012.06.068.

[56] Kramer O. Genetic Algorithm Essentials. Cham: Springer International Publishing; 2017. doi:10.1007/978-3-319-52156-5.

[57] Fitschy L, Thirifay F, Wyart E, Pierret S, Geuzaine P. Structural optimization of a small aircraft wing from aeroelastic responses. Fluid Struct. Interact. Mov. Bound. Probl. IV, vol. I, Southampton, UK: WIT Press; 2007, p. 173–81. doi:10.2495/FSI070161.

[58] Kato H, Pierret S, Coelho RF. CAD-Centric Framework for Aero-mechanical Optimization - Counter-Rotating Fan Design. In: Deconinck H, Dick E, editors. Comput. Fluid Dyn. 2006, Berlin, Heidelberg: Springer Berlin Heidelberg; 2009, p. 861–6.

[59] Optimal Computing. Xtreme Technology n.d. https://www.optimalcomputing.be/software/xtreme-technology.php (accessed November 27, 2018).

[60] Fu G, Gu J, Lourenco MI, Duan M, Estefen SF. Parameter determination of double-ellipsoidal heat source model and its application in the multi-pass welding process. Ships Offshore Struct n.d.:37–41. doi:10.1080/17445302.2014.937059.

[61] Virfac -溶接シミュレーションソフトウェア- ｜ CAEソリューション：株式会社JSOL n.d. https://www.jsol-cae.com/product/seisan/virfac/ (accessed December 23, 2018).

APPENDIX A

W1 WELD BEADS

	Weld Length [mm]	Weld throat thickness [mm]			Direction	Duration [s]
W1F1	145	3	3	3	-	8
W1A1	140	4	4	4	-	10
W1F2	140	5	4	3	-	12
W1A2	150	4.5	3	3	-	12
W1F3	150	4	5	5	-	8
W1A3	145	5	4	3	+	12
W1F4	145	5.5	3	3	-	11
W1A4	160	4	4	3	-	11
W1F5	150	3.5	3	3	+	10
W1A5	135	4	3	4	+	10
W1F6	130	4	3	3	-	10
W1A6	150	4	4	4	+	11
W1F7	150	4	3	3	+	11
W1A7	150	5	4	3	-	13
W1F8	140	3.5	3.5	4	+	9
W1A8	145	5	3	4	+	9

W2 WELD BEADS

	Weld Length [mm]	Weld throat thickness [mm]			Direction	Duration [s]
W2F1	145	4	3.5	4	-	17
W2A1	145	5	4	4	-	11
W2F2	140	5	4	4	-	14
W2A2	145	4	4	4	-	12
W2F3	140	4	4	5	-	11
W2A3	150	4	3.5	3.5	-	10
W2F4	145	4.5	4	3	-	12
W2A4	120	4.5	4	3	-	13
W2F5	140	4.5	3.5	3.5	+	12
W2A5	160	5	4	3	+	14
W2F6	150	4	4	4.5	+	14
W2A6	150	4	4	3	-	12
W2F7	140	5	4	4	+	13
W2A7	125	4	4	4	+	13
W2F8	140	4.5	4	5	+	12
W2A8	140	4	4	4	+	10

W3 WELD BEADS

	Direction	Weld Length [mm]	Weld throat thickness [mm]			Duration [s]
W3F1	-	135	4	3	3	10
W3A1	-	125	5	4	4	10
W3F2	-	110	4.5	4	4	10
W3A2	-	120	5	4	4	9
W3F3	-	160	4	3	3	14
W3A3	-	140	4	3	4	14

W3F4	-	170	4	3	3	16
W3A4	-	165	4	3	3	16
W3F5	-	170	4	3	3	13
W3A5	-	165	5	4	3	17
W3F6	+	160	5	4	3	17
W3A6	+	175	4	3.5	3	15
W3F7	+	160	4	4	4	14
W3A7	+	170	5	3	4	17
W3F8	+	160	4	3	3.5	14
W3A8	+	165	4	3.5	3	15
W3F9	+	125	4	4	4	11
W3A9	+	115	5	4	4	9
W3F10	+	120	5	4	4	9
W3A10	+	130	4	4	3	10

W4 WELD BEADS

	Direction	Weld Length [mm]	Weld throat thickness [mm]			Duration [s]
W4F1	-	140	4.5	4	3	11
W4A1	-	135	4.5	4	3	11
W4F2	-	100	5	4	3.5	14
W4A2	-	110	5	4	3	10
W4F3	-	150	5	4	4	16
W4A3	-	155	5	4	3.5	14
W4F4	-	165	4.5	4	3.5	15
W4A4	-	160	5	4.5	4.5	16
W4F5	-	170	5	4	4	11
W4A5	-	175	4.5	4	4	16
W4F6	-	180	5	4	3	18
W4A6	+	180	4.5	3.5	4	14
W4F7	+	165	4	4	4	17
W4A7	+	170	4.5	4	3.5	14
W4F8	+	155	5	4	4	16
W4A8	+	150	5	4	3.5	16
W4F9	+	110	4.5	3.5	3	12
W4A9	+	110	4.5	4	3.5	9
W4F10	+	135	5	4	4	11
W4A10	+	130	4	3	3.5	9

W5 WELD BEADS

	Direction	Weld Length [mm]	Weld throat thickness [mm]			Duration [s]
W5F1	-	130	4	3.5	4	10
W5A1	-	125	5	4	3	11
W5F2	-	110	4	3.5	4	10
W5A2	-	120	5	4	3	12
W5F3	-	160	5	4	4	16
W5A3	-	160	5	4	4	14
W5F4	-	175	4	3	4	16
W5A4	-	170	4	4	4	13
W5F5	-	170	3.5	3	4.5	15

W5A5	-	165	5	4	3.5	15
W5F6	-	160	4	3	3	12
W5A6	+	170	5	4	5	14
W5F7	+	165	5	4	4	15
W5A7	+	165	5	4	4	17
W5F8	+	165	5	4	4	17
W5A8	-	160	4.5	4	4	15
W5F9	+	115	5	4	4	12
W5A9	+	120	4	3.5	4.5	10
W5F10	+	135	6	5	3.5	11
W5A10	+	120	5	4	4	12

W6 WELD BEADS

	Direction	Weld Length [mm]	Weld throat thickness [mm]			Duration [s]
W6F1	-	110	5	3	4	10
W6A1	-	105	4	3	4	10
W6F2	-	115	4.5	3.5	3	14
W6A2	-	115	5	4	4	9
W6F3	-	155	5	4	3	16
W6A3	-	150	4.5	4	3.5	12
W6F4	-	165	5	3	3.5	16
W6A4	-	175	4	3	3	12
W6F5	-	160	3.5	3	3.5	14
W6A5	-	160	5	4	3	14
W6F6	+	160	4	3	3	15
W6A6	+	160	4.5	3	4	13
W6F7	+	180	4	4	3.5	17
W6A7	+	170	4.5	3	4	12
W6F8	+	155	5	3.5	3	12
W6A8	+	155	5	3	5	15
W6F9	+	120	5	4	4	11
W6A9	+	120	4	3	4	9
W6F10	+	115	4.5	4	3	9
W6A10	+	115	4	3	3.5	10

W7 WELD BEADS

	Direction	Weld Length [mm]	Weld throat thickness [mm]			Duration [s]
W7F1	-	235	4	3	3	16
W7A1	-	240	4	3	3	19
W7F2	-	235	4	3	4	16
W7A2	-	240	4	3	3	16
W7F3	-	235	4	4	3	13
W7A3	+	250	5	4	4	17
W7F4	+	240	4	4	5	20
W7A4	+	245	4	3	3	15
W7F5	+	240	4	4	4	10
W7A5	+	225	3	3	3	13

W8 WELD BEADS

	Direction	Weld Length [mm]	Weld throat thickness [mm]			Duration [s]
W8F1	-	220	5	4	4	11
W8A1	-	220	5	4	4	12
W8F2	-	200	5	4	4	12
W8A2	-	200	4	5	5	12
W8F3	-	205	4.5	4	4	16
W8A3	+	190	5	4	4	15
W8F4	-	80	5	4	4	11
W8A4	+	105	4	4	4	16
W8F5	+	240	5	4	5	16
W8A5	+	205	4.5	5	5	15
W8F6	+	270	5	4	4	16
W8A6	+	280	5	5	5	16

J1 WELD BEADS

	Direction	Weld Length [mm]	Weld throat thickness [mm]	Duration [s]
J1FF	+	80	4.5	7
J1AF	+	80	5	10
J1FA	+	80	5	11
J1AA	+	80	4	9

J2 WELD BEADS

	Direction	Weld Length [mm]	Weld throat thickness [mm]	Duration [s]
J2FF	+	80	5	9
J2AF	+	80	5.5	10
J2FA	+	80	4	11
J2AA	+	80	3	8

J3 WELD BEADS

	Direction	Weld Length [mm]	Weld throat thickness [mm]	Duration [s]
J3FF	+	80	5	6
J3AF	+	80	5	9
J3FA	+	80	5	6
J3AA	+	80	4.5	9

J4 WELD BEADS

	Direction	Weld Length [mm]	Weld throat thickness [mm]	Duration [s]
J4FF	+	80	5	10
J4AF	+	80	5	8
J4FA	+	80	5	11
J4AA	+	80	5	10

J5 WELD BEADS

	Direction	Weld Length [mm]	Weld throat thickness [mm]	Duration [s]
J1FF	+	80	7	8
J1AF	+	80	4.5	9
J1FA	+	80	5	7
J1AA	+	80	4.5	7

J6 WELD BEADS

	Direction	Weld Length [mm]	Weld throat thickness [mm]	Duration [s]
J1FF	+	80	4.5	10
J1AF	+	80	4	8
J1FA	+	80	5	12
J1AA	+	80	4.5	9

J7 WELD BEADS

	Direction	Weld Length [mm]	Weld throat thickness [mm]	Duration [s]
J1FF	+	80	6	7
J1AF	+	80	4	8
J1FA	+	80	6	9
J1AA	+	80	4.5	10

J8 WELD BEADS

	Direction	Weld Length [mm]	Weld throat thickness [mm]	Duration [s]
J1FF	+	80	4	12
J1AF	+	80	4	7
J1FA	+	80	6	12
J1AA	+	80	4.5	10

APPENDIX B

ORIGINAL SEQUENCE MODEL - REPRESENTATION

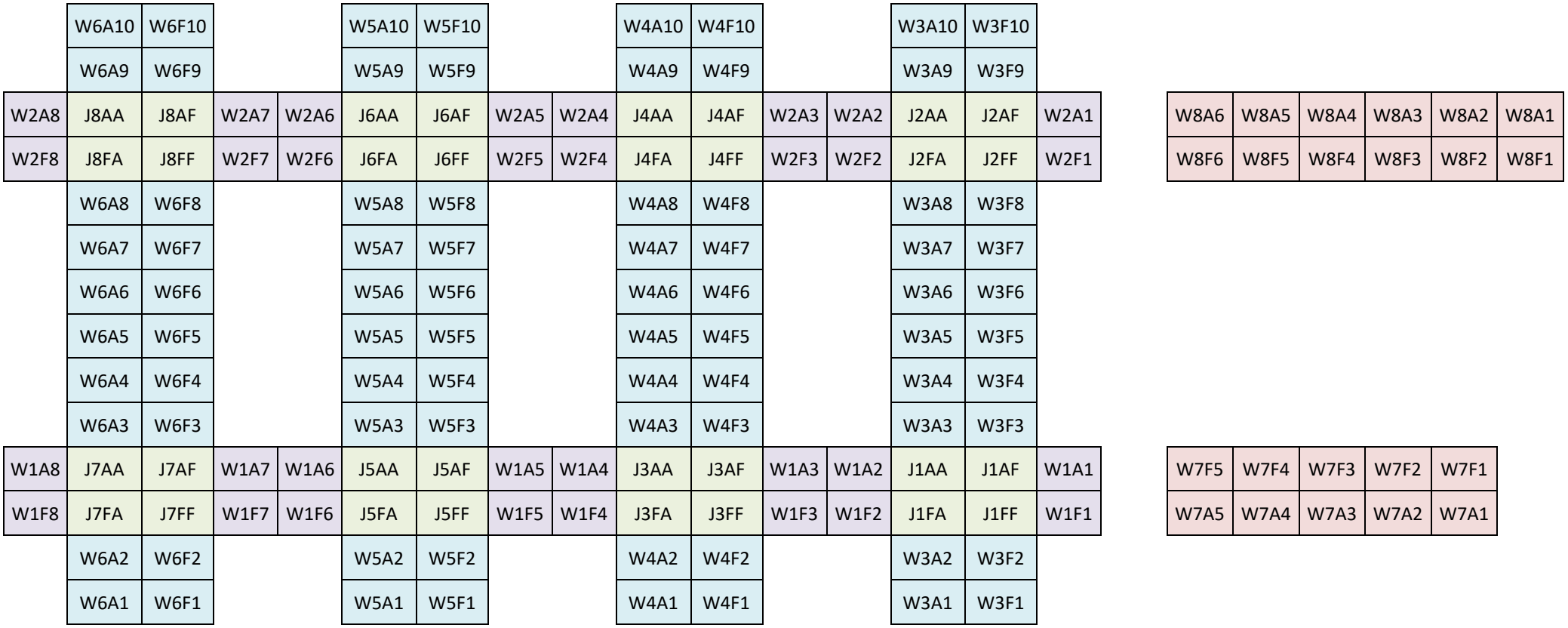

ORIGINAL SEQUENCE MODEL – ORIGINAL SEQUENCE

	161	162			88	89			69	70			140	141	
	163	160			90	87			71	68			142	139	
44	118	114	52	41	117	113	47	39	116	112	49	45	115	111	53
54	126	122	43	50	125	121	40	48	124	120	42	51	123	119	46
	154	151			81	79			61	59			133	131	
	150	152			78	91			58	63			130	143	
	166	147			94	75			74	55			146	127	
	148	164			76	92			56	72			128	144	
	165	149			93	77			73	57			145	129	
	155	153			82	80			62	60			134	132	
29	110	106	38	25	109	105	32	23	108	104	34	28	107	103	36
35	102	98	27	33	101	97	24	31	100	96	26	37	99	95	30
	159	156			86	83			67	64			138	135	
	157	158			84	85			65	66			136	137	

5	10	1	11	7	3
6	9	2	12	8	4

16	22	21	18	14
15	20	19	17	13

ORIGINAL SEQUENCE MODEL – 100 ITERATIONS (TRY 98)

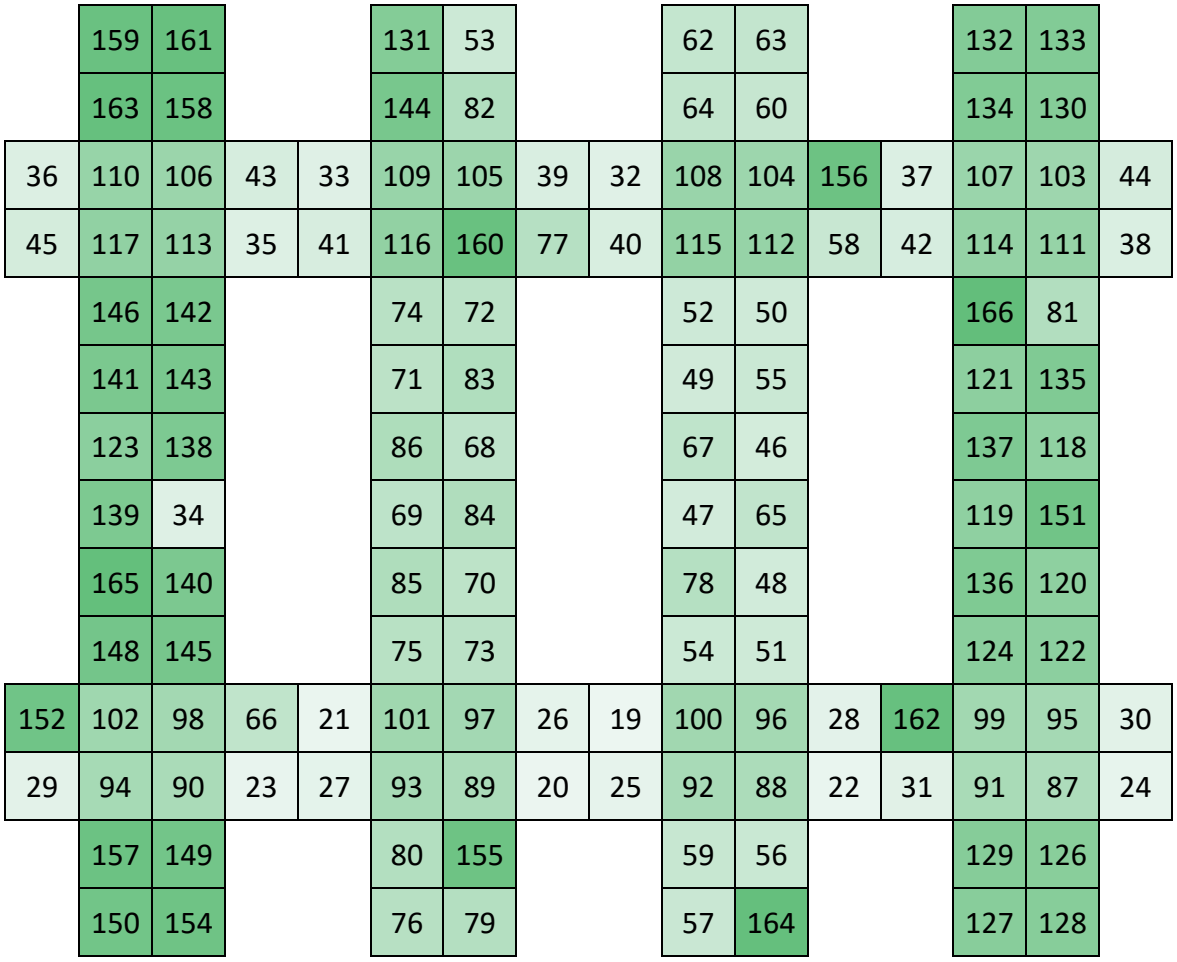

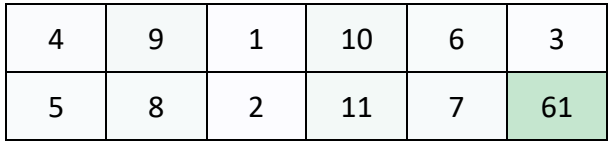

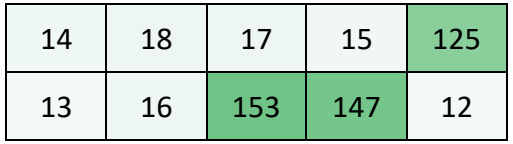

ORIGINAL SEQUENCE MODEL – 200 ITERATIONS (TRY 164)

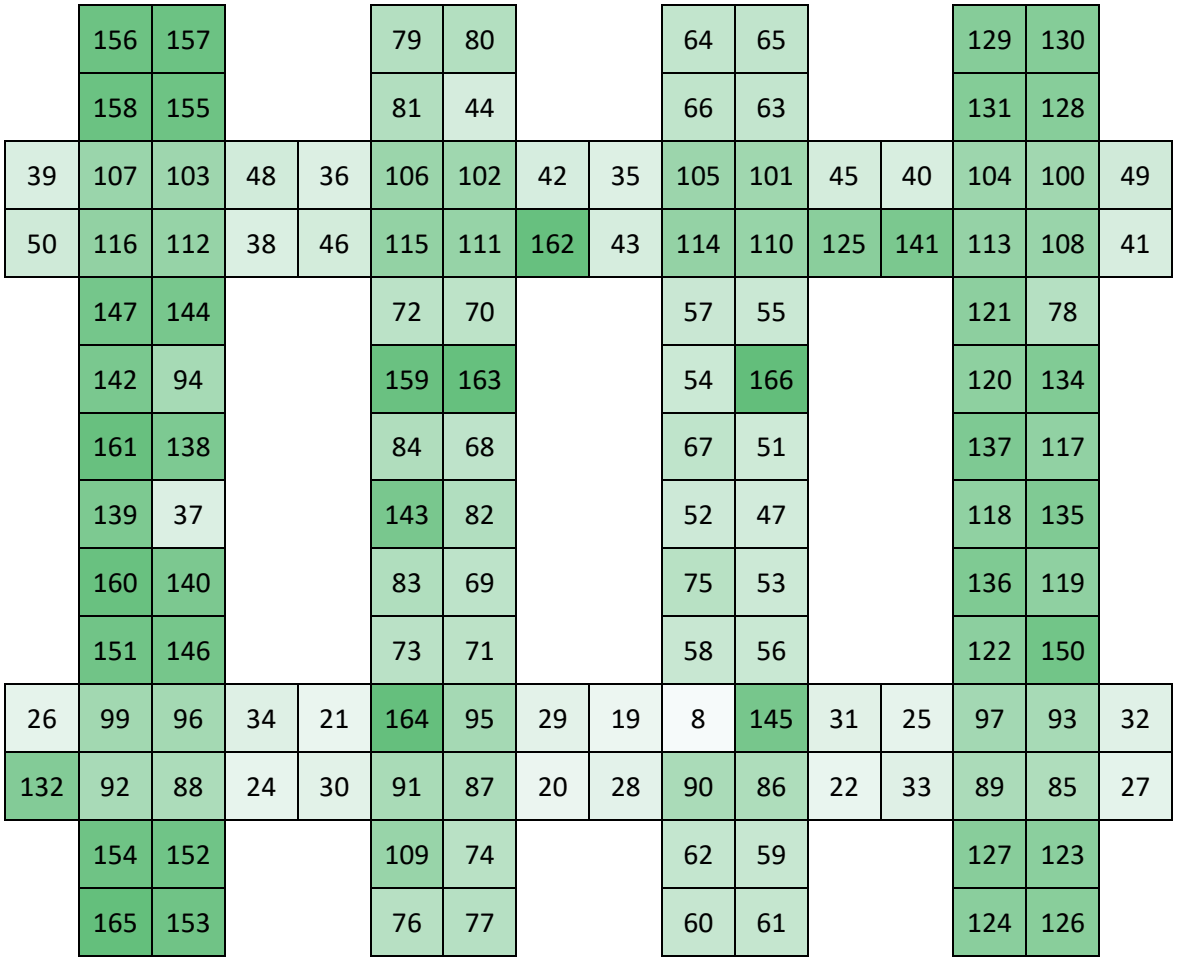

	156	157			79	80			64	65			129	130	
	158	155			81	44			66	63			131	128	
39	107	103	48	36	106	102	42	35	105	101	45	40	104	100	49
50	116	112	38	46	115	111	162	43	114	110	125	141	113	108	41
	147	144			72	70			57	55			121	78	
	142	94			159	163			54	166			120	134	
	161	138			84	68			67	51			137	117	
	139	37			143	82			52	47			118	135	
	160	140			83	69			75	53			136	119	
	151	146			73	71			58	56			122	150	
26	99	96	34	21	164	95	29	19	8	145	31	25	97	93	32
132	92	88	24	30	91	87	20	28	90	86	22	33	89	85	27
	154	152			109	74			62	59			127	123	
	165	153			76	77			60	61			124	126	

5	98	1	9	7	3
6	23	2	148	133	4

13	18	17	14	11
12	16	15	149	10

COMMON SEQUENCE MODEL – REPRESENTATION

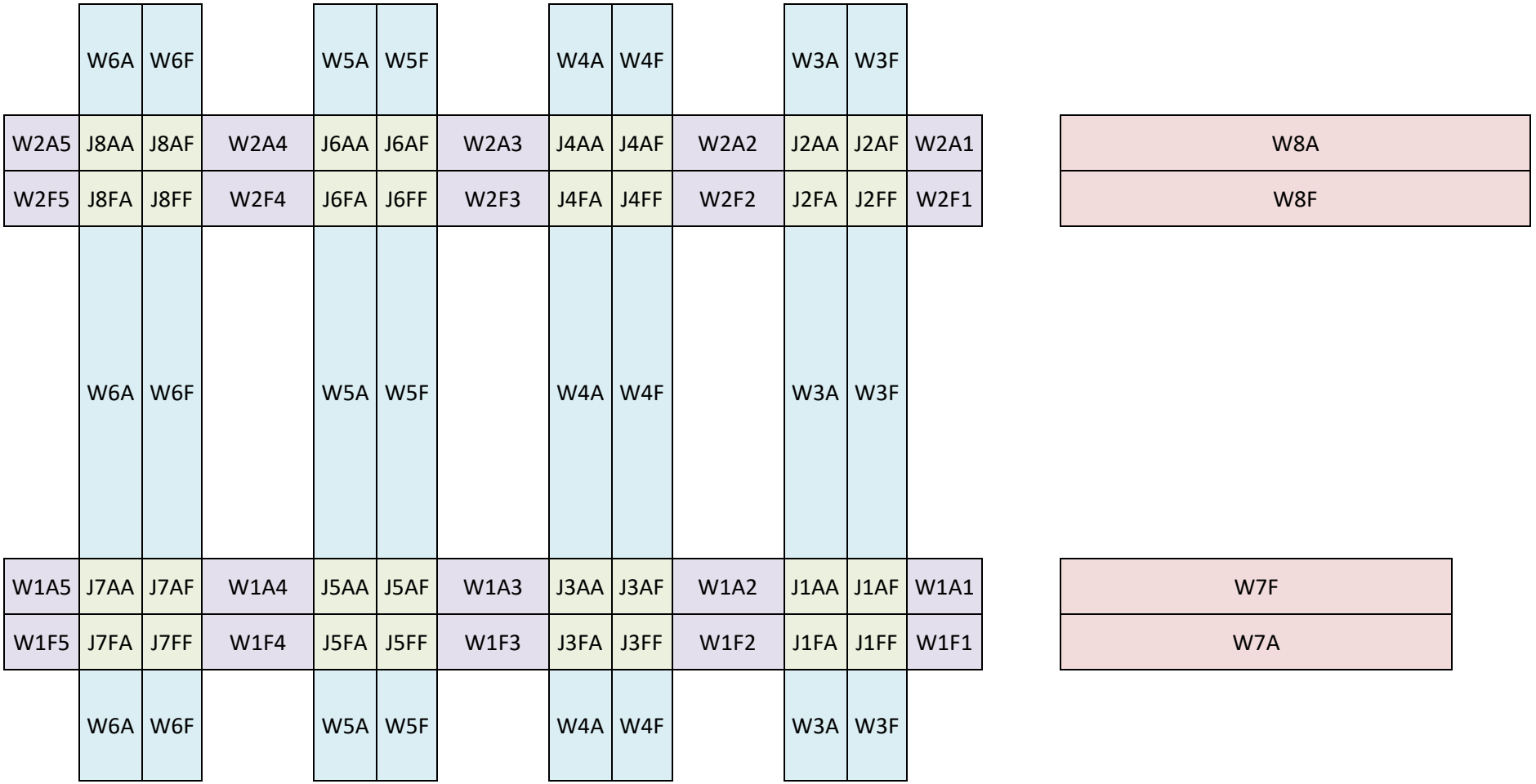

COMMON SEQUENCE MODEL – ORIGINAL SEQUENCE

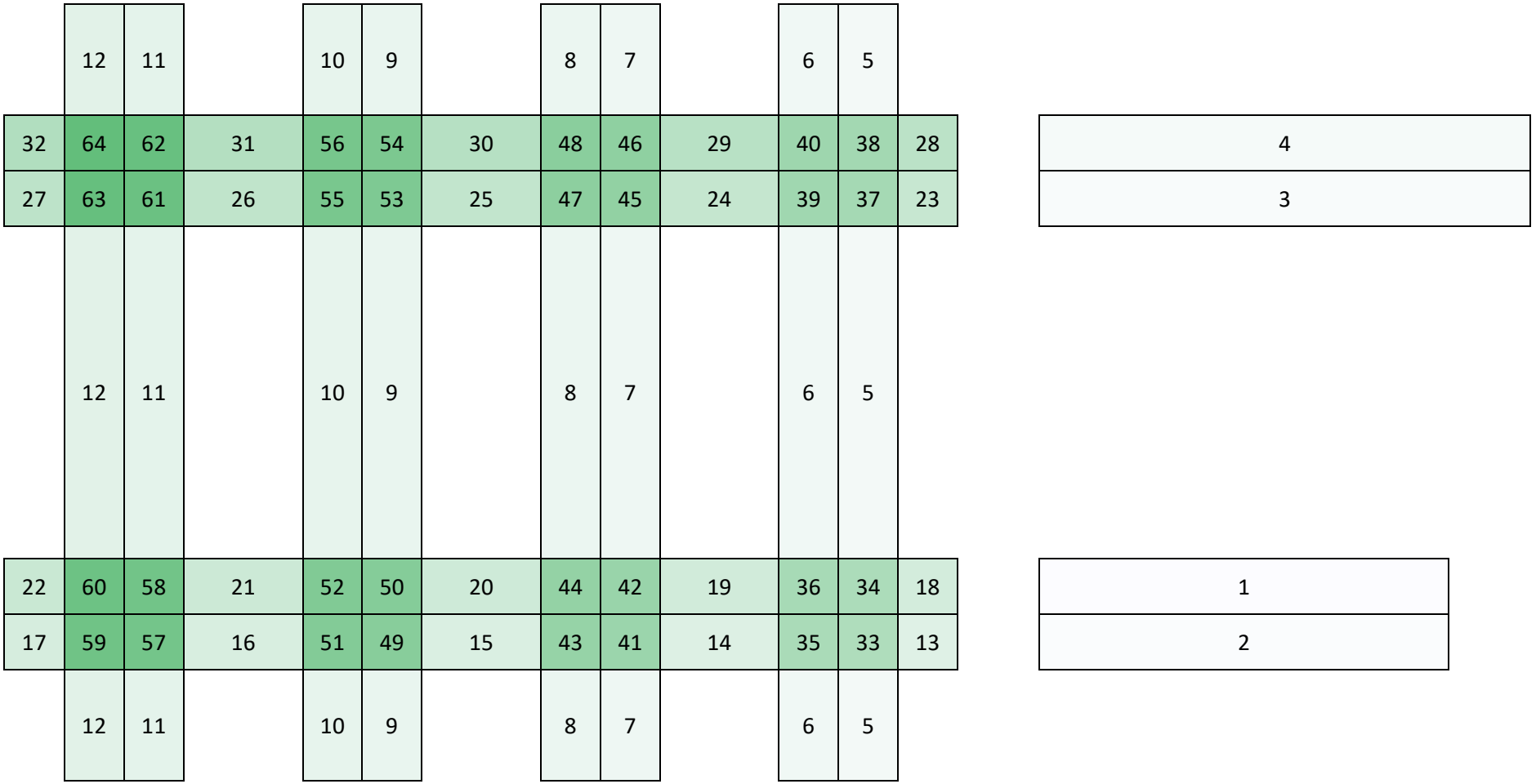

COMMON SEQUENCE MODEL – 100 ITERATIONS (TRY 85)

	12	11		10	9		8	7		6	5	
15	54	34	32	63	49	31	57	44	30	41	37	29
18	58	60	28	50	48	27	45	59	26	40	38	25
	12	11		10	9		8	7		6	5	
24	56	36	23	47	39	22	43	42	21	35	33	20
19	64	53	17	46	52	16	55	62	14	61	51	13
	12	11		10	9		8	7		6	5	

4
3
1
2

COMMON SEQUENCE MODEL – 200 ITERATIONS (TRY 199)

	12	6		11	10		9	7		8	5	
15	35	60	31	50	57	30	37	59	29	40	39	28
22	42	58	27	49	55	25	46	48	24	36	38	23
	12	6		11	10		9	7		8	5	
18	43	34	21	64	56	26	45	41	32	44	33	20
19	61	53	17	47	52	16	54	63	14	62	51	13
	12	6		11	10		9	7		8	5	

4
2
1
3